UNIVERSITÀ
DEGLI STUDI
FIRENZE

INTERNATIONAL DOCTORATE IN
ATOMIC AND MOLECULAR PHOTONICS

CICLO XXIX

COORDINATORE: PROF. ROBERTO RIGHINI

Control of quantum dynamics on an atom chip

Settore Scientifico Disciplinare: FIS/03

Dottorando:
Cosimo LOVECCHIO

Supervisore:
Prof. Francesco Saverio
CATALIOTTI

Coordinatore:
Prof. Roberto RIGHINI

Anni 2013/2016

Alla mia famiglia

Abstract

In this thesis, I report on experiments concerned with the control of single atom internal dynamics. These experiments are performed on a Bose-Einstein condensate (BEC) of ^{87}Rb atoms prepared on an atom chip. In particular, we developed a practical tomography protocol, we investigated the possibility to prepare an arbitrary internal state in a given Hilbert space, and demonstrated, for the first time, Quantum Zeno Dynamics, which consists in the confinement of coherent dynamics in tailored sub-spaces.

Cold atomic systems and degenerate quantum gases are unique tools for quantum simulations, but their applications outside laboratory depend critically on the simplification and downsizing of bulky experimental setups. From this point of view, atom chips provide compact and robust platforms, which allows high integration, and open the path to the combination of atoms with solid state structures.

In the experiments we manipulate, by means of radio-frequency fields, a BEC of ^{87}Rb atoms produced in a magnetic micro-trap. The trapping, as well as the radio-frequency fields, are provided by wires embedded on the chip surface. By means of forced Rabi oscillations and Ramsey spectroscopy, we are able to carefully set all the experimental parameters describing the dynamics of the atoms. Exploiting this ability we implemented a tomography protocol relying on time-resolved measurements of the population distribution among atomic internal states during an accurately controlled coherent evolution. This protocol allows to reconstruct with high fidelities any unknown density matrix, even with small set of data. Equipped with this novel state reconstruction techniques, and making use of the tools developed in the field of optimal control, we demonstrate our ability to manipulate the internal state wave function in order to prepare arbitrary superpositions. We investigated the connection between the time length of the manipulation, and the accuracy in the target state preparation. Finally, we have proven how a coherent evolution is modified when perturbed by measurements and strong couplings, which dynamically disconnect different groups of quantum states and constrain the atoms to evolve inside a reduced level sub-space. We have measured long living coherences in the protected space, and we demonstrated the equivalence between different measurement protocols.

All these results fit into the broad context of quantum control, and confirm the versatility of the atom chip as benchmark to investigate quantum dynamics.

Contents

Introduction

There is little doubt that we are approaching the era of *quantum technologies*, where increasingly complex devices grow closer to the ultimate limit imposed by quantum mechanics, thinning the boundary between fundamental research and technological development. As a consequence, quantum control [1] - i.e., the ability to prepare and control the quantum states of physical systems minimizing the resources spent - promises cross advancements in many areas, from biology to medicine, from quantum simulation and computation to engineering and informatics [2–5].

For example the disruptive breakthrough of the realization of a quantum computer appears not to be so far behind the horizon. The fundamental ideas of quantum computing date back to '70s, and the famous lecture given by R. Feynman [6] is widely accepted has launched the field. Along the years, with the advancement of experimental abilities, the discussion turned to be more concrete from being merely theoretical, until the mandatory conditions to implement a quantum computer [7] were defined. Nowadays we are in a situation in which a commercial quantum simulator already exists[1] and a big company has made available a quantum processor composed of five superconducting qubits on its cloud[2].

Atom chips based experiments [8], among all, have proven to be very promising platforms for the future quantum information processors, joining most of the necessary properties that a realistic architecture should have, like scalability [9–11], precise control of the coherent evolution [12], and the capability of integrating cold atoms with nanostructures [13–15]. Indeed, they have already enabled the demonstration of some of the key components of a quantum architecture [16–18].

This thesis concerned with a Bose-Einstein condensate of ^{87}Rb atoms prepared on an atom chip, to exploit and explore the possibilities offered by quantum control, in particular facing three problems related to the realization of a reliable quantum information processor: The initialization of the system state to a fiducial one. The creation of protected areas of the Hilbert space where quantum informations can be stored and manipulated. The ability to read the results of a general manipulation.

[1] http://www.dwavesys.com/

[2] http://www.research.ibm.com/quantum/

Thesis outline

I will present the main results of my PhD work in the following order

- In **Chapter 1** I review the magnetic properties of ^{87}Rb, used to manipulate and trap atomic cloud by suitably engineered magnetic fields. I will then describe the experimental apparatus and the magnetic trap implemented on our atom chip. Finally the manipulation and detection tools employed all along the thesis will be presented.

- In **Chapter 2** I present a tomography protocol which allows an easy reconstruction of the results of a manipulation accomplished on the internal states of a condensate. Relying only on the time-resolved measurements of the atomic population distribution among such states, it represents a practical, experimentally undemanding tool which does not require the access to the condensate state by means of fields created externally to the chip. I will show how it is possible to achieve good reconstructions fidelities even with a modest number of measurements, without the necessity to spend much computational efforts.

- In **Chapter 3** I address the problem of the arbitrary preparation of the system state by applying results of optimal control theory. Starting from a given initial state which is fixed by the BEC evaporation procedure, by means of appropriately shaped radio-frequency manipulation pulses I will show how to prepare different arbitrary coherent superposition of states. I will report on the investigation of the limits of our scheme by characterizing the dependence of the final state preparation error as a function of the manipulation time.

- In **Chapter 4** I report on the experimental realization, by means of engineered strong couplings and controlled measurements, of the Quantum Zeno Dynamics, which lead to the creation of dynamically disconnected regions of the Hilbert space, where a qubit can be confined and protected out from the remaining sub-levels. The measurements show how it is possible to achieve the protection enabled by the Zeno Dynamics using different perturbation protocols on the system. The final part of this chapter is dedicated to the investigation of confinement strength and of coherence in the protected sub-space.

Publications

The results presented in this thesis are reported in the following references:

- F. Schäfer, I. Herrera, S. Cherukattil, **C. Lovecchio**, F.S. Cataliotti, F. Caruso and A. Smerzi, *"Experimental realization of quantum zeno dynamics"*, Nat. Comm. **5** 4194 (2014).
- **C. Lovecchio**, S. Cherukattil, B. Cilenti, I. Herrera, F.S. Cataliotti, S. Montangero, T. Calarco, F. Caruso, *"Quantum state reconstruction on atom-chips"*, New. J. Phys. **17**, 093024 (2015).
- **C. Lovecchio**, F. Schäfer, S. Cherukattil, M. Alì Khan, I. Herrera, F. S. Cataliotti, T. Calarco, S. Montangero, and F. Caruso, *"Optimal preparation of quantum states on an atom-chip device"*, Phys. Rev. A **93**, 010304(R) (2016).

Other publications of related results:

- P. Lombardi, F. Schäfer, I. Herrera, S. Cherukattil, J. Petrovic, **C. Lovecchio**, F. Marin, F.S. Cataliotti, *"Reading the phase of a Raman excitation with a multi-state atomic interferometer"*, Optics Express Vol. **22**, 19141 (2014).
- S. Gherardini, **C. Lovecchio**, M. M. Müller, P. Lombardi, F. Caruso, F. S. Cataliotti, *"Ergodicity in randomly perturbed quantum systems"*, arXiv preprint arXiv: 1604.08518.

Chapter 1

Bose-Einstein condensation on atom chips

1.1 Magnetic trapping on atom chips

In this first chapter I will give an overview of the basic concepts underlying this thesis. In the first Section I will briefly introduce the physics of the atomic element we use in our experiment, the ^{87}Rb, especially its magnetic properties, crucial to trap the atoms by engineered potentials. The second section will contain a brief description of the experimental apparatus used to perform the experiments described in following chapters. Then in the third section the typical experimental sequence to reach the BEC is summarized. Finally I will briefly present the main manipulation and probing tools extensively used all along this work. What I will not discuss in this chapter are the Bose-Einstein condensation, which can be found in almost every book of modern physics, and the common laser cooling techniques, also addressed by many exhaustive books [19].

Further details on the experimental system used in this thesis work can be found in [20].

1.1.1 ^{87}Rb hyperfine structure

Discovered in 1861, in Heidelberg, by Robert Bunsen and Gustav Kirchhoff, Rb, but in particular its isotope ^{87}Rb, is the evergreen of the atomic physics. Came to fame in 1995 when the first ever Bose-Einstein condensate was achieved, today is widely used from technological applications, to fundamental research.

The characteristic ruby absorption line of rubidium has two components coming from a fine-structure doublet, the D_1 ($5^2S_{1/2} \rightarrow 5^2P_{1/2}$) and D_2 ($5^2S_{1/2} \rightarrow 5^2P_{3/2}$) transitions. Each transition has an underlying hyperfine-structure produced by the coupling between the nuclear angular momentum $\mathbf{I}$ and the total electron angular momentum $\mathbf{J} = \mathbf{L} + \mathbf{S}$. The Hamiltonian describing the ground level hyperfine structure is $H_{\rm hfs} = A_{\rm hfs}\, \mathbf{J} \cdot \mathbf{I}$, where $A_{\rm hfs}$ is the magnetic dipole constant (see appendix B), and it can be diagonalized by the eigenkets of the total angular momentum operator $\mathbf{F^2}$ and its projections F_z, indicated as $|F, m_F\rangle$. The total momentum $\mathbf{F}$ is given by $\mathbf{F} = \mathbf{I} + \mathbf{J}$, and in the

Rb ground state it takes the values $F = 2$, and $F = 1$ ($L = 0$). Each F sublevel is $(2F + 1)$-fold, and degenerate in absence of any applied fields. This degeneracy is broken when an atom is immersed in an external magnetic field $\mathbf{B}$, and the Hamiltonian $H_{\rm hfs}$ is corrected by the interaction term $H_B = -\boldsymbol{\mu} \cdot \mathbf{B}$, where $\boldsymbol{\mu} = -\mu_B(g_s\mathbf{S}+g_I\mathbf{I})/\hbar$, μ_B is the Bohr magneton, g_s and g_I the spin and nuclear Landé g-factors. In presence of a $\mathbf{B}$ directed along the z direction, the total Hamiltonian then reads

$$H = A_{\rm hfs}\mathbf{J} \cdot \mathbf{I} + \mu_B B(g_s S_z + g_I I_z)/\hbar \tag{1.1}$$

For a weak field H_B can be treated as a perturbation of $H_{\rm hfs}$, so F and F_z are still good quantum numbers. The shifts of the energy levels of H induced by $\mathbf{B}$ are well approximated by the formula

$$\Delta E_{F,m_F}(B) = \mu_B g_F m_F B\,, \tag{1.2}$$

where g_F is the total angular momentum Landé g-factor. Otherwise, when the weak field approximation fails, and one has to diagonalize H on eigenstates of I and S. For the ground state of Rb, in the case of intermediate fields, the following analytical result, known as Breit-Rabi formula [21], holds

$$E_{F,m_F}(B) = -\frac{\Delta E_{\rm hfs}}{2(2I+1)} + g_I\mu_B m_F B \pm \frac{\Delta E_{\rm hfs}}{2}\left(1 + \frac{4m_F x}{2I+1} + x^2\right)^{1/2}, \tag{1.3}$$

where $\Delta E_{\rm hfs} = A_{\rm hfs}(I + 1/2)$ is the hyperfine splitting, sign $+$ $(-)$ is related to the $F = 1$ ($F = 2$) level, and

$$x = \frac{\mu_B(g_J - g_I)B}{\Delta_{\rm hfs}}\,. \tag{1.4}$$

We point out that, while the new eigenvectors of H are still commonly indicated as $|F, m_F\rangle$, they are different from the eigenvectors of $H_{\rm hfs}$, as they depend by the strength of the magnetic field B. Note that for weak fields Eq. 1.3 recover the linear behaviour of Eq. 1.2.

To describe the internal state dynamics of the atoms in an homogeneous magnetic field, all our numerical routines will always make use of the Breit-Rabi formula, and, wherever not explicitly stated, we refer to $|F, m_F\rangle$ as the eigenkets of H.

We conclude this section noting that, given the dependency of the atomic energy levels by the external magnetic field, while moving in an spatially inhomogeneous $\mathbf{B}(\boldsymbol{r})$ the atoms will be affected by a force. If we are then able to create a field configuration for which a minimum of $E_{F,m_F}(B(r))$ exists, then we will also able to trap atoms. In the next two sections I will describe the most widely used trap geometries, the quadrupole trap and the Ioffe-Pritchard trap, and how to realize the latter by using a current distribution easily achievable

on a chip, the Z-trap.

1.1.2 Quadrupole and Ioffe-Pritchard traps

Realized by means of two coils in anti-Helmholtz configuration, the quadrupole trap consists in a field $\mathbf{B}(\boldsymbol{r})$ which is vanishing in some position, say $\boldsymbol{r} = 0$. Around this vanishing point, $\mathbf{B}(\boldsymbol{r})$ increases approximately linearly, i.e.

$$\mathbf{B}(\boldsymbol{r}) = B'_x x\, \boldsymbol{e_x} + B'_y y\, \boldsymbol{e_y} + B'_z z\, \boldsymbol{e_z}\,, \tag{1.5}$$

still fulfilling the divergenceless condition $\nabla\cdot$B(r)$= 0$. If we assume that a moving particle keeps a constant projection of the total magnetic moment on the field line direction, then Eq. 1.2 (or Eq. 1.3, in the case of intermediate field) will hold everywhere. The magnetic potential in a nearby of $\boldsymbol{r} = 0$ will be given by

$$\Delta E_{F,m_F}(B(r)) = \mu_B g_F m_F \sqrt{(B'_x x)^2 + (B'_y y)^2 + (B'_z z)^2}\,, \tag{1.6}$$

and it will produce a magnetic force $F_B \propto \hat{r}$ directed towards the center of the trap, or outwards, depending on the sign of the product $g_F\, m_F$. The m_F substates such that $g_F m_F > 0$, i.e. $|F = 2, m_F = +1/+2\rangle$, and $|F = 1, m_F = -1\rangle$, are confined and thus called "low field seeking states", unlike those for which $g_F m_F < 0$ which are repelled and then called "high field seeking states". The difficulty in using this trap for ultra-cold atoms, is represented by the zero field point. Indeed, moving across this position (and its very nearby) an atom feels a magnetic field which change direction abruptly, thus it cannot keep a constant projection of the magnetic moment on the field orientation, undergoing a spin flip process after which the output state can be an high field seeking state, which is expelled from the trap. This loss mechanism is known as Majorana spin flips [22].

To overcome the spin flip problem, to the quadrupole field it can be superimposed an homogeneous field B_{IP}. The effect is to avoid the zero in $\boldsymbol{r} = 0$, still leaving this position as a minimum for the total $\mathbf{B}(\boldsymbol{r})$. The combination homogeneous-quadrupole field is the so-called Ioffe-Pritchard (IP) trap [23], which provides a quadratic magnetic confinement. For example, in the case of axial symmetry the trapping field close to the trap center is given by

$$\boldsymbol{B}(\boldsymbol{r}) = B_{IP} \begin{pmatrix} 1 \\ 0 \\ 0 \end{pmatrix} + B' \begin{pmatrix} 0 \\ -x \\ z \end{pmatrix} + \frac{B''}{2} \begin{pmatrix} x^2 + (y^2 + z^2)/2 \\ -xy \\ -xz \end{pmatrix}\,, \tag{1.7}$$

and its modulus, expanded to the second order in r, produces an harmonic trap having trap frequencies

$$\begin{aligned} \omega_{\text{axial}} &= \sqrt{\frac{\mu}{m} B''} \\ \omega_{\text{radial}} &= \sqrt{\frac{\mu}{m}\left(\frac{B'^2}{B_{IP}} - \frac{B''}{2}\right)}, \end{aligned} \tag{1.8}$$

where $\mu = \mu_B m_F g_F$, and m is the mass of the trapped particle.

The evolutions of the IP trap, as the *cloverleaf trap* [24] and the *QUIC trap* [25, 26], are the most used magnetic traps in cold atoms experiments. In the next section we will show how to implement a Ioffe-Pritchard trap by means of a planar distribution of current.

1.1.3 Z-trap

A Z-trap is a special case of wire trap, which consists in current conducting wires arranged so as to create a trapping magnetic potential. To illustrate the working principle of this kind of traps, let us start from the most simple example: an infinitely thin straight wire carrying a current I. This creates a magnetic field given by $\mathbf{B}_{\boldsymbol{w}}(\boldsymbol{r}) = \mu_0\, \mathbf{I} \times \boldsymbol{r}/2\pi\, r^2$. At distance r_0 from the wire the field modulus will be $B_0 = \mu_0\, I/2\pi\, r_0$, so, by superimposing to $\mathbf{B}_{\boldsymbol{w}}$ an homogeneous magnetic field B_0 perpendicular to the wire direction, a line of 0 field will be created parallel to the wire. In the region around this zeros line, the total magnetic field is well approximated by a quadrupole field, as shown in Fig. 1.1.

Given that the confinement is only radial, this geometry is suitable to transport atoms along the wire direction, but it does not provide an axial confinement, necessary to form a three dimensional trap. To confine the atoms in all direction we can to provide a straight wire with *endcaps*. In other words, by bending a finite length wire to form a Z, it is possible to create closely enough to the central wire a line of zeros, to which the field produced by the Z arms adds up creating the axial confinement. In the particular case of the Z-trap, the field produced by the arms has a finite value at the trap center, as shown in Fig. 1.2, so the total field results in a three-dimensional Ioffe-Pritchard trap.

The Z-wire trap is harmonic near its minimum, yet it has a strong confinement by a nearly linear gradient further away from the wire, allowing efficient evaporative cooling. It is actually the wire geometry we use in our experimental setup to trap the BEC, as we are going to show in the next section.

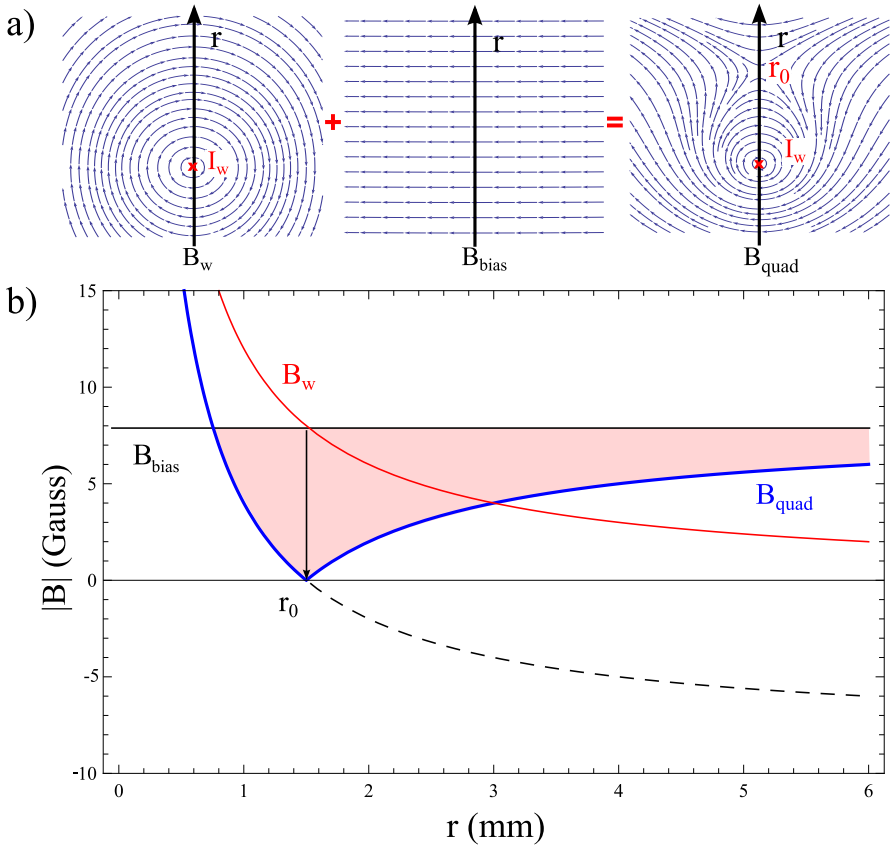

FIGURE 1.1: (a) The combination of the field produced by a straight wire, varying as $B_w \sim 1/r$, with a homogeneous bias field B_{bias}, produces a two-dimensional quadrupole field in the plane perpendicular to the wire. (b) Magnetic field strength dependence as a function of the distance from the wire. Red line correspond to B_w and black line to the bias field B_{bias}. In the plane where these fields have opposite direction, they will sum up to zero in r_0, which will be the center of the quadrupole trap

1.2 Experimental setup

1.2.1 Chip layout

The chip installed in our apparatus consists of a $2\,\mu\mathrm{m}$ thick gold layer evaporated on top of an extremely flat silicon surface, and it was produced by the Quantum Optics group of the University of Vienna. The wires on the surface were obtained by opportunely removing gold portions in such a way to shape the appropriate structures. In particular, before the evaporation of gold, the silicon surface it is allowed to oxide, creating a very thin layer (less than $100\,\mathrm{nm}$) of isolating SiO_2, then is covered with photoresist which is patterned by photolithography, after that an adhesion layer of Ti, $30\,\mathrm{nm}$ thick, is deposited everywhere. Finally, after covering everything with gold, the remaining photoresist

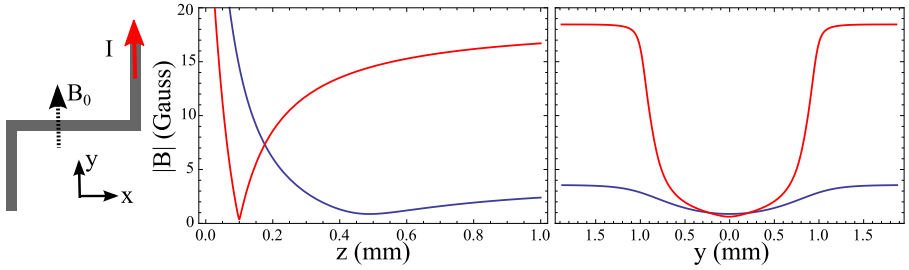

FIGURE 1.2: Layout of z-shaped IP, and calculated magnetic fields generated for $I = 1A$. The bias field along y was set to have the trap at positions $r_0 = 0.5\,\mathrm{mm}$ (red line) and $0.1\,\mathrm{mm}$ (blue line). The fields shown in the figure take into account a wire width of $125\,\mu\mathrm{m}$

was removed. The resulting wires has several widths (50, 125, $300\,\mu\mathrm{m}$), and are defined by $10\,\mu\mathrm{m}$-wide gaps. The whole surface is remarkably smooth, with grain size $< 50\mathrm{nm}$.

The chip layout is shown in Fig. 1.3. The asymmetric dimensions compensate the beam diameter during the mirror MOT phase (described in the next section), since the beams hit the chip at $45°$. In the picture we highlight in pink colour the z-shaped wire which generates the potentials for the IP trap where the condensate is produced. The z has a central body length d of $d = 2\,\mathrm{mm}$ and $6\,\mathrm{mm}$ long arms. The width w of this wire was set to $w = 125\mu\mathrm{m}$. The resulting resistance is $1.63\,\Omega$. The values of w and d were chosen in order to have a compromise between a low ohmic heating of the wire (large w, small d) and large attainable trap frequencies trapping volume(small w, large d and I).

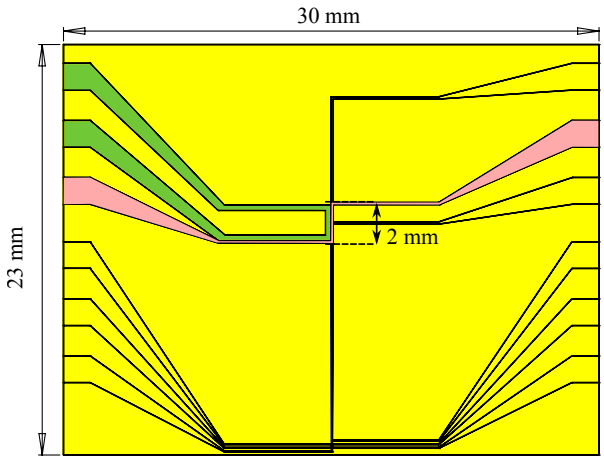

FIGURE 1.3: Layout of the chip wires. The z-shaped on-chip wire used to create the IP trap is highlighted in pink. In green we also highlight the u-wire used to create a radio-frequency magnetic field for the internal state manipulation.

The measured trap frequencies in the center of the Ioffe-Pritchard trap created by an external bias field of $15\,\mathrm{Gauss}$ directed along the $-x$ direction are

$$\begin{aligned} \omega_{\mathrm{axial}} &= 2\pi \times 76\,\mathrm{Hz} \\ \omega_{\mathrm{radial}} &= 2\pi \times 975\,\mathrm{Hz}\,. \end{aligned} \tag{1.9}$$

In Fig. 1.3 we highlight in green a u-shaped wire originally included to create an intermediate confining potential between the z-trap and the previous trapping stages. The purpose of this wire was to facilitate the loading in the z-trap by creating a shallower and wider potential which was better fitting the characteristics of the external trapping fields. However, because of its close proximity to the atoms, it is currently exploited to create a radio-frequency field for the atomic internal state manipulation. Given the width this wire ($w = 300\,\mu\mathrm{m}$) its resistance is lower than that of the z-wire ($R = 0.8 \div 0.9\,\Omega$), and its reactive component is almost negligible up to frequencies of tenth of MHz. Thus, by directly applying to the wire heads a voltage signal $V(t) = A\cos(\omega_{RF}t)$, it will carry a proportional current $I(t) = R\,V(t)$. In correspondence of the central body of the u-wire, at the distance of $d = 190\,\mu\mathrm{m}$ from the chip surface, i.e. where our condensate is created, provided that ω_{RF} does not goes over few tenth of MHz, the electromagnetic field created by $I(t)$ is a near-field, and it can be approximately considered as created by an infinitely long wire. The atoms will be then interested by a time varying magnetic field given by

$$\begin{aligned} B(t) &= (\mu_0 R/2\pi\, d)V(t) \\ &= A(\mu_0 R/2\pi\, d)\cos(\omega_{RF}t) \end{aligned} \tag{1.10}$$

As we will show in the following, this magnetic field is able to drive transitions between the internal m_F states of the hyperfine structure, and thus it will provide a suitable tool for the state manipulation.

1.2.2 Coils and lasers

Like many atom chip experiments, our apparatus consists of a single steel vacuum chamber at which, in the bottom part, is attached a rectangular glass parallelepiped (science cell) made in Vycor. The chip emerges from the steel chamber in the science cell, with the surface oriented upside down. The vacuum in the science cell is sustained by a $125\,\mathrm{l/s}$ ion pump, and the background gas pressure measured by the pump controller is constantly about $10^{-10}\,\mathrm{mbar}$ during normal experimental activity. A Ti-sublimation pump is also attached to the main steel chamber. Close around to the science cell (see Fig. 1.4), 6 pairs of Helmholtz coils, 2 for each direction, generate the homogeneous magnetic bias fields $\{B_x, B_y, B_z\}$ used to set the position of the traps center, nullify the environmental magnetic field, and to set the sub-levels energies for the internal state

manipulation (e.g. by Eq. 1.3), while a $45°$ tilted external pair in anti-Helmholtz configuration creates the quadrupole magnetic field for the preliminary cooling in the mirror MOT phase.

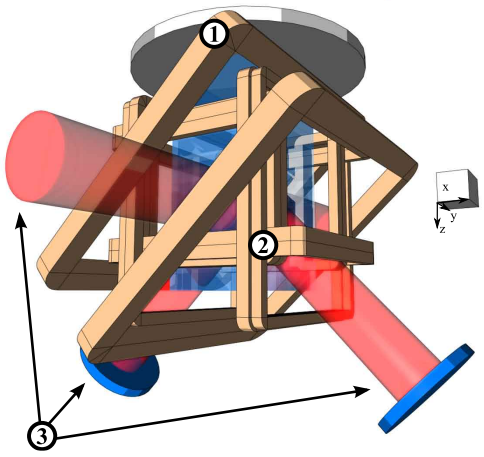

FIGURE 1.4: Coil suit and MOT laser beam propagation. (1) The MOT coils are $45°$ degrees tilted, to create the mirror MOT configuration, (2) 6 pairs of coils in Helmholtz configuration generates opposite bias fields in each direction, (3) MOT beams.

Behind the chip surface (see Fig. 1.5) an addition z-shaped kapton wire (big-Z) provides an intermediate large volume Ioffe trap to enable a better transfer from the molasses into the magnetic trap of the chip. The big cross-section of this wire ($0.61\,\mathrm{mm}$, $0.87\,\mathrm{mm}$ with jacket, KAP2) allows to push high currents and thus to form the minimum of the trap away from the chip surface. Keeping the external field constant and decreasing the big-Z current, the trap position moves closer to the chip surface, until the trapping potential of the z-trap on the chip can be turned on. An additional benefit of such small-scale circuits is that their low inductance enables rapid changing and switching of the potentials. In Fig. 1.5 it can also be noted, under the kapton z-wire , an additional couple of u-shaped conductors, one of which is actually used to generate on the cloud the radio-frequency field for the forced evaporation.

To cool down the atoms to temperatures of the order of $10\,\mu\mathrm{K}$, several different laser light frequencies are required. These are illustrated in Fig. 1.6 along with the hyperfine structure of the ground $5^2\mathrm{S}_{1/2}$ and excited $5^2\mathrm{P}_{3/2}$ states of the D2 transition in ^{87}Rb. In our setup this frequencies are generated by two DFB lasers, whose beams are split and modulated by acousto-optic modulators. This two lasers with the optical elements and devices for the frequencies manipulation, are placed in a black closed box, and connected to the optical table where the science cell is by polarization maintaining fibers (with the exception of the optical pumping beam).

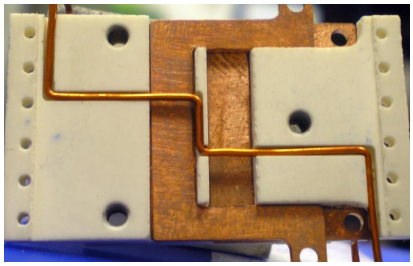

FIGURE 1.5: Photograph of the Z kapton wire. Embedded in the white sustaining structure, two u-shaped conductor which closest one to the chip surface is used to carry the radio-frequency signal for the evaporation.

The DFB master laser provides lights for the MOT cooling, optical pumping and absorption imaging. Its output is frequency stabilized on the crossover $F = 2 \rightarrow F' = \mathrm{CO}(2,3)$ by a frequency-modulation (FM) locking system which acts on the supply current. After passing through an optical isolator and an anamorphic prism, the light is divided in two beams which are sent to a double pass AOM, and to an optical amplifier. The beam going to the AOM (AOM1) is shifted almost in resonance with the transition cooling $F = 2 \rightarrow F' = 3$, and then is further divided in two part, one is sent to the FM spectroscopy setup for the frequency stabilization, the other to another double pass AOM scheme (AOM2) to get the optical pumping light. The light injecting the optical amplifier is amplified up to $850\,\mathrm{mW}$. This amplification is necessary to capture a large number of atoms in the preliminary cooling stage accomplished by the MOT. After being amplified it is red-shifted respect to the cooling transition by a single pass AOM (AOM3), aligned to get the maximum efficiency on the negative diffracted order. The negative first diffracted order is finally sent to a PBS cube to clean the polarization and coupled to an optical fiber to be used as cooling light. Due to the great power from the optical amplifier the first positive order diffracted by the AOM3 has enough power to be used, $\sim 15\,\mathrm{mW}$. This light, after a double-pass trough an AOM (AOM4), it is frequency shifted down in order to be resonant with the $F = 2 \rightarrow F' = 3$ transition. Finally an optical fiber cleans the spacial profile of this beam to get the imaging beam.

The second DFB laser provides the light for the repumping $F = 1 \rightarrow F' = 2$. It is stabilized using the polarization spectroscopy and locked to $F = 1 \rightarrow F' = \mathrm{CO}(1,2)$ crossover resonance. A small part of the light produced by the laser is sent to the spectroscopy setup, and the other through a single pass AOM, shifting the frequency in order to be resonant with the required transition.

1.3 Reaching BEC

In every cold atoms experiment, the path from a gaseous atomic species to a BEC is made of several subsequent cooling and trapping steps. Even the most

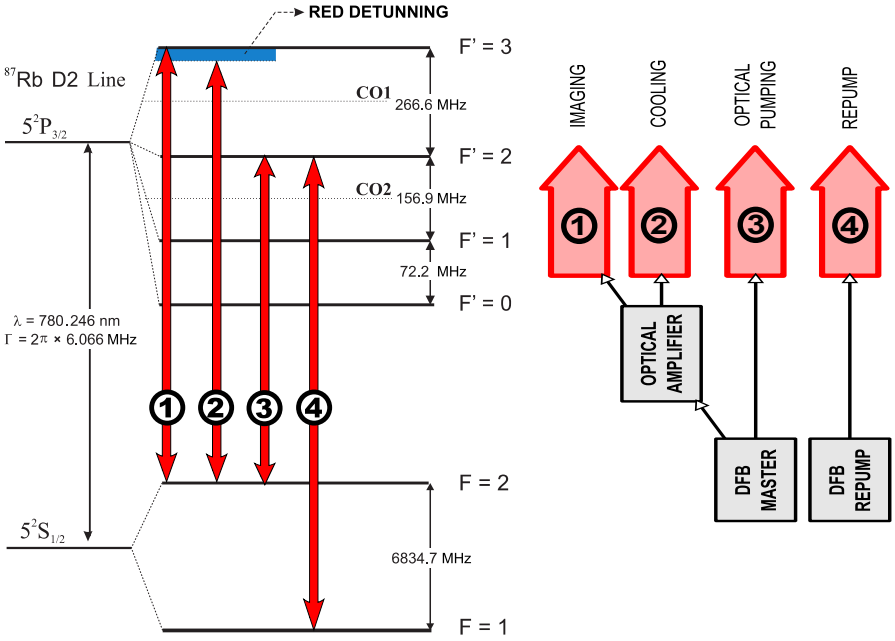

FIGURE 1.6: Left side: The hyperfine structure of the $5^2S_{1/2}$ and $5^2P_{3/2}$ states of ^{87}Rb D2 line, from [21], showing the laser frequencies required for the experiment, and the intervals (in MHz) between the hyperfine levels. 1) MOT/molasses cooling, 2) optical pump, 3) imaging, 4) repumper. Right side: Small map of the laser sources and the final lights beams.

prepared research team would spend several months designing the experimental system and tuning all the parameters involved, but once every single variable is under control, an usual condensation cycle is accomplished in few tens of seconds. Atom chips based systems are remarkable from the point of view of the condensation velocity, being usually able to produce a BEC in few seconds. The sketch I will provide of our procedure for the production of the BEC does not do justice to the work previously done to make it possible, but a detailed exposition can be found in [20].

Our experimental cycle lasts $23\,\mathrm{s}$: during the first $8\,\mathrm{s}$ we produce, manipulate, and probe the BEC, while in the remaining time the chip cools down for the successive cycle. As Rb source we use two dispensers placed behind the chip (SAES dispensers). They are activated at the beginning of the cycle by a $2\,\mathrm{s}$ long pulse of current at $7\,\mathrm{Amps}$, which causes the evaporation of atoms at a temperature of about $\sim 970\,\mathrm{K}$. The confining potential generated by the on-chip z-wire has a maximum depth of $\sim 150\mu\mathrm{K}$ at $190\,\mu\mathrm{m}$ from the surface, and thus, to efficiently load it, we need to cool down the atoms at a lower temperature. This cooling can be broken down in 6 main steps, during which the temperature of the trapped atomic cloud is lowered and simultaneously its phase space

density is increased. These steps are listed below.

Mirror-MOT

The first cooling step is carried out by a mirror-MOT, in which the mirror role is played by the gold chip surface. In particular the cooling light is divided in 4 beams (see. Fig 1.4). Two are counter propagating and aligned along the y direction, parallel to chip surface, touching it. The other two impinge on the chip at 45° from opposite directions and lay in the xz plane. In this phase the cooling light is $-3\,\Gamma$ detuned from the cyclic transition $F = 2 \rightarrow F' = 3$ ($\Gamma \sim 2\pi\,6\,\mathrm{MHz}$ is the natural line width of the D_2 transition), and the beams power density is the maximum available, i.e. $\sim 10\,\mathrm{mW/cm^2}$. The repump light, with the total power of $7\,\mathrm{mW}$ after the fiber, is mixed with the cooling light by a polarizing beam splitter. The 45° tilted anti-Helmholtz coils create a quadrupole field which minimum is set, with the aid of the homogeneous bias field generated by the Helmholtz coils, $7\,\mathrm{mm}$ away from the chip surface, in an overlapping region of the beams.

The mirror-MOT phase starts simultaneously to the activation of the dispensers, and lasts for $4.5\,\mathrm{s}$, when approximately $N = 70 \times 10^7$ atoms are cooled at a temperature of about $T = 120\,\mu\mathrm{K}$. At this point the trapped cloud phase space density is $\Phi = 8.5 \times 10^{-8}$.

CMOT and optical molasses

After loading the mirror-MOT, the atomic cloud is moved at a distance of $2\,\mathrm{mm}$ from the chip surface, in the place where the magnetic trap generated by the kapton z-wire will be switched on. This transport is achieved by linearly ramping up the bias fields along z and x directions in $450\,\mathrm{ms}$. Once the atoms have reached their final position, they undergo a compression in a CMOT.

The CMOT step consists of a normal MOT with increased red detuning of the trapping laser, decreased power of the cooling light and greatly reduced repump laser power. It has the effect of reducing radiation pressure in the trap and thus creating a denser cloud of atoms. Specifically, the repump power is reduced to $50\,\mu\mathrm{W}$, and simultaneously we jump the detuning of the cooling light to $-14\,\Gamma$, while its power is reduced by 80%. The entire CMOT stage lasts about $14\mathrm{ms}$, during which the temperature of the atoms is reduced to $T = 25\,\mu\mathrm{K}$, and their phase space density increased to $\Phi = 8.5 \times 10^{-7}$.

At the end of the CMOT stage a short molasses step is performed. During $4\,\mathrm{ms}$ the quadrupole field is switched off and the bias field is adjusted in order to compensates the environment magnetic fields. The benefits of the molasses are greatest in terms of temperature: at the end of the stage the cloud has a temperature of $T = 10\,\mu\mathrm{K}$ and a phase space density of $\Phi = 4.5 \times 10^{-6}$.

Optical pumping

The optical pumping cycle starts immediately after we switch off the molasses light, and lasts 300μs. First a magnetic field of $1\,\mathrm{Gauss}$ is set along the y direction in $100\,\mu$s, then we turn on the repump light and the optical pumping light. The latter is also oriented along the y direction and is σ^+ polarized, in order to transfer the whole atomic population in the strong field seeking state $F = 2, m_F = +2$ by successive absorption and spontaneous emission cycles. We illuminates the atoms with the pumping light for $150\,\mu$s, and for further $50\,\mu$s with the repump light. At the end of the process the cloud temperature slightly increase to $T = 12\,\mu$K, however the improvements of the magnetic trap loading is dramatic.

Magnetic trapping in the big Z trap

This is formed by rapidly increasing the current I_Z through the Z-shaped kapton wire, and simultaneously setting the bias field along x (B_x) in order to obtain the position of the minimum of the resulting confining potential $2\,\mathrm{mm}$ away from the surface, and the bias field along y (B_y) to set a non vanishing value of the field in the minimum so as to prevent the Majorana flipping. In particular, we set $B_x = 10.5\,\mathrm{Gauss}$, and $B_y = 3\,\mathrm{Gauss}$. Actually I_Z is ramped up from 0 to the maximum value of $25\,\mathrm{Amps}$ given by our supply, by a double-MOSFET circuit to speed-up the switching which is accomplished in a total time of $300\,\mu$s. Simultaneously the $-x$ and $-y$ bias coils currents are set to about $2\,\mathrm{Amps}$.

Magnetic transfer and trapping in the z on-chip trap

After having loaded the Z-shape kapton wire (big Z) trap, we adiabatically transfers the atoms to the magnetic trap potential made by the on-chip z-wire (small z). By linearly turning off the current in the big Z, and keeping constant the bias field along x, the position of the minimum of the trap is moved toward the chip surface. Simultaneously the current through the small-z is turned on, from 0 to $1.7\,\mathrm{Amps}$, and the bias field in the y-direction is decreased to maintain the residual field at the trap center. This transfer is accomplished in $250\,\mathrm{ms}$, which follows a second compression in the small-z trap by rising up the x bias field from $B_x = 10.5\,\mathrm{Gauss}$ to $B_x = 15.5\,\mathrm{Gauss}$ in $250\,\mathrm{ms}$. At the end of this compression, the trap minimum is located $190\,\mu\mathrm{m}$ above the chip surface, the number of atoms held is decreased to $N = 1.5 \times 10^7$, their temperature goes up to $T = 90\,\mu$K, and the phase space density to $\Phi = 1.8 \times 10^{-5}$.

Radio frequency forced evaporation

The last step along the path to BEC is to apply forced radio frequency evaporative cooling to the compressed atom cloud. After compression we apply to

the U-shaped conductor behind the chip (see Fig. 1.5) a radio frequency signal whose frequency is exponentially swept from $22\,\mathrm{MHz}$ to a final value of $0.7\,\mathrm{MHz}$ in $3\,\mathrm{s}$. The phase space density overcome the critical value $\Phi = 2.614$ at the expense of the atom number, indeed the condensation is reached with $N = 90 \times 10^3$ atoms in the pure state $|2, +2\rangle$, at a the temperature of $T = 480\,\mathrm{nK}$. The dimensions (Thomas-Fermi radii) of the condensed cloud in the anisotropic magnetic trap are $d_{\mathrm{axial}} = 15.5\,\mu\mathrm{m}$ along the axial direction, and $d_{\mathrm{rad}} = 1.26\,\mu\mathrm{m}$ in the radial direction.

1.4 Manipulating and probing BEC

The experiments presented in the following chapters of this thesis will have has common ingredient the quantum dynamics in the hyperfine ground manifold of Rb atoms, i.e. the coherent evolution of m_F sub-states superpositions in presence of a driving field. A versatile tool to realize such driving is provided by the radio-frequency near-field produced by the u-wire structure integrated on the chip surface (see section 1.2.1 and Fig. 1.3). Hereafter, given the intended use of this particular wire, we will refer to it as chip "antenna".

After a generic manipulation of an m_F superposition we need to extract some information about the output state, and here again we exploit the magnetic properties of the Rb, applying the Stern-Gerlach method, combined with an absorption imaging technique, to determine the occupation probabilities of each m_F sub-level.

In the following two sections I will enter into the details of the state manipulation and the Stern-Gerlach discrimination.

1.4.1 Radio-frequency manipulation

As seen in section 1.1.1, an homogeneous magnetic field perturbs the Hamiltonian describing the Rb hyperfine structure, and this perturbation is semiclassically introduced in H by an interaction term between the vector of magnetic moment operators $\boldsymbol{\mu}$ and the classical field $\mathbf{B_0}$, i.e. by the term $H_B = -\boldsymbol{\mu} \cdot \mathbf{B_0}$. Of course this description holds also in the case af a time varying magnetic field $\mathbf{B}(t)$ having polarization $\widehat{\boldsymbol{\xi}}$, thus in general we will have

$$\begin{aligned} H &= H_{\mathrm{hfs}} + H_B(t) \\ &= A_{\mathrm{hfs}} \mathbf{J} \cdot \mathbf{I} + \mu_B \left(\mathbf{B_0} + B(t)\, \widehat{\boldsymbol{\xi}} \right) \cdot (g_s \mathbf{S} + g_I \mathbf{I})/\hbar \,. \end{aligned} \tag{1.11}$$

By exploiting the non-diagonality of the terms $\boldsymbol{\xi} \cdot \mathbf{S}$ and $\boldsymbol{\xi} \cdot \mathbf{I}$, we can connect different sub-states, making possible transitions between them.

The first approximation introduced in Eq. 1.11 is to neglect the interaction with the nuclear magnetic moment, since $|g_I/g_s| \approx 0.5 \times 10^{-3}$. A second one is

to considered the coupling between $\mathbf{B}(t)$ and $\mathbf{S}$ as a perturbation, if $B(t) \ll B_0$. In this case we can represent the related term in the basis of the eigenstates of the Hamiltonian as given by Eq. 1.1. These field dependent eigenstates are still labelled as $|F, m_F\rangle$, and indeed, for the magnetic fields of few Gauss considered here, they are well approximated by the true eigenstates of the operators $\mathbf{F^2}$ and F_z. Finally, when we consider an oscillating field $B(t) = B_{RF}\cos(\omega_{RF}t)$, we can make a RWA approximation. Changing reference to the frame rotating at frequency ω_{RF}, in the case of $|\omega_{RF} - \Delta\omega_F| \ll \Delta\omega_F$, where $\Delta\omega_F$ is the mean energy distance between neighbouring m_F sub-levels, the Hamiltonian 1.11 reads

$$\begin{aligned} H = \sum_{F,m_F} (E_{F,m_F}(B) - \hbar\, m_F\, \omega_{RF})\, |F, m_F\rangle \langle F, m_F| + \\ + \frac{\hbar}{2} \sum_{F,m_F,m_{F'}} \Omega_{F,m_F,m_{F'}}\, |F, m_F\rangle \langle F, m_{F'}| \ , \end{aligned} \tag{1.12}$$

where we have introduced the coefficients

$$\Omega_{F,m_F,m_{F'}} = \frac{\mu_B\, g_s\, B_{RF}}{\hbar}\ \langle F, m_F|\, \widehat{\boldsymbol{\xi}} \cdot \mathbf{S}\, |F, m_{F'}\rangle \ . \tag{1.13}$$

Depending on the field polarization $\widehat{\boldsymbol{\xi}}$ and the quantization axis direction, these coefficients can lead either to a coupling between different m_F sub-levels, or to a correction on the diagonal elements of H. We consider here a linear polarized field along the x direction (as it is the case in our experiment), orthogonal to the quantization axis imposed by $\mathbf{B_0}$. In this case only the terms $\Omega_{F,m_F,m_{F'}}$ with $m_F \neq m_{F'}$ will be different from 0.

The RWA approximation lead to ignore in H the couplings between substates belonging to different hyperfine levels, too far out of resonance to produce any effect on the dynamics. Thus the total Hamiltonian can be written as $H = H_{F=2} \oplus H_{F=1}$, allowing to treat the dynamics in the two manifold independently. We can then individually shift the sub-levels energies by a quantity $E_{F,0}(B)$[1], and redefine the diagonal elements as $E_{F,m_F}(B) - E_{F,0}(B) - \hbar\, m_F\, \omega_{RF} \equiv \delta_{F,m_F}(B, \omega_{RF})/\hbar$. We also define, from Eq. 1.13, the Rabi frequency $\Omega = \mu_B\, g_s\, B_{RF}/\hbar$. Ultimately, for our purposes, a matrix representation of Eq. 1.12 results more convenient, as well as more intuitive. The Hamiltonians acting on the two hyperfine sub-spaces then read

[1]This correspond to a unitary transformation $U(t) = \sum_F \exp\{-i\, E_{F,0}(B)\, \mathbb{1}_F\, t\}$.

$$H_{F=2} = \hbar \begin{pmatrix} \delta_{2,+2}(B,\omega_{RF}) & \Omega & 0 & 0 & 0 \\ \Omega & \delta_{2,+1}(B,\omega_{RF}) & \sqrt{\frac{3}{2}}\,\Omega & 0 & 0 \\ 0 & \sqrt{\frac{3}{2}}\,\Omega & \delta_{2,0}(B,\omega_{RF}) & \sqrt{\frac{3}{2}}\,\Omega & 0 \\ 0 & 0 & \sqrt{\frac{3}{2}}\,\Omega & \delta_{2,-1}(B,\omega_{RF}) & \Omega \\ 0 & 0 & 0 & \Omega & \delta_{2,-2}(B,\omega_{RF}) \end{pmatrix}, \tag{1.14}$$

$$H_{F=1} = \hbar \begin{pmatrix} \delta_{1,+1}(B,\omega_{RF}) & \sqrt{\frac{1}{2}}\,\Omega & 0 \\ \sqrt{\frac{1}{2}}\,\Omega & \delta_{1,0}(B,\omega_{RF}) & \sqrt{\frac{1}{2}}\,\Omega \\ 0 & \sqrt{\frac{1}{2}}\,\Omega & \delta_{1,-1}(B,\omega_{RF}) \end{pmatrix}. \tag{1.15}$$

All along this thesis we will represent the internal state of the atoms by using the density matrix formalism. The state dynamics will be then described by the von Neumann equation, in which we include the Lindblad super-operator term $\mathcal{L}$, acting on a density matrix ρ as $\mathcal{L}[\rho] = \sum_j \gamma_j[-\{|j\rangle\langle j|,\rho\}+2|j\rangle\langle j|\rho|j\rangle\langle j|]$, where j runs over all the $\{F, m_F\}$ sub-states, and γ_j are dephasing rates uniformly set, for simplicity, to $\gamma_j \equiv \gamma\ \forall j$. Then the dynamical equation reads

$$\frac{d}{dt}\rho(t) = -\frac{i}{\hbar}[H(t,B,\Omega,\omega_{RF}),\rho(t)] + \mathcal{L}[\rho(t)]\ . \tag{1.16}$$

As seen in section 1.2.1, we can employ the chip u-wire (the antenna), to generate on the BEC a time varying magnetic field, whose strength depends on the amplitude A of the voltage signal applied at the antenna ends, as Eq. 1.10 shows. Given that the Rabi frequency Ω defined above is linear in B_{RF}, and this is linear in the A, it turns out that $\Omega \propto A$.

We now make some considerations on the space homogeneity of Ω. To perform our experiments, we turn off the chip z-wire trap which holds the atoms, and after $800\,\mu$s of free falling, we apply to the antenna a voltage signal to manipulate the BEC. Typically a manipulation is accomplished in about $100\,\mu$s or less. During the manipulation time the radial radii of the BEC increases from approximately $6.1\,\mu$m to $7\,\mu$m, while the axial radii is almost constant at $16\,\mu$m. On the other hand, after the $800\,\mu$s of free fall the condensate moves $3\,\mu$m down from the trap position, and during the subsequent manipulation it further fall for $0.8\,\mu$m. Summing the contributions of both the cloud expansion and the fall, we can estimate a maximum variation of the Rabi frequency of $\Delta\Omega = (\Delta d/d)\Omega \sim 5.2 \times 10^{-3}\,\Omega$. We can then safely approximate Ω as constant on the whole BEC during the entire manipulation time.

1.4.2 Stern-Gerlach and absorption imaging

An unique tool extensively used thorough this thesis is the Stern-Gerlach discrimination. As discussed in section 1.1.1 and 1.1.2, an inhomogeneous magnetic field $\mathbf{B(r)}$ exerts on an atom a force arising from the interaction Hamiltonian $H_B = -\boldsymbol{\mu} \cdot \mathbf{B(r)}$. In particular, an atom in a pure m_F state will experience the force

$$\langle F, m_F | \nabla(-\boldsymbol{\mu} \cdot \mathbf{B(r)}) | F, m_F \rangle = -\mu_B g_F m_F \nabla B(r) \,. \tag{1.17}$$

It follows that atoms belonging to different m_F sub-states, while moving across the inhomogeneous field region (deflection area), will be physically deflected in different directions. Let us suppose that for each of these directions, and thus for each m_F sub-state, it is available a detector Π_{m_F} which clicks for every atom on that path. If we now let pass through the deflection area a single atom prepared in a particular coherent superposition $\widetilde{\psi} = \sum_{m_F} c_{m_F} |F, m_F\rangle$, this will be measured by one of the detectors according to the probabilities of occupying the single sub-states $|c_{m_F}|^2$. Repeating the passage and detection procedure N times, having care to start from the same identical state $\widetilde{\psi}$, each detector Π_{m_F} will click a number of times n_{m_F}. If N is statistically relevant then the set of measurements will be a good approximation of the theoretical expectations, i.e. $n_{m_F} \sim N |c_{m_F}|^2$, allowing us to extract information about the state of the atoms. This is actually the case of a non interacting BEC, made of N identical atoms, all crossing together the deflection area.

In our set-up the inhomogeneous magnetic field $\mathbf{B(r)}$ is generated by a pairs of anti-Helmholtz coils placed in proximity of the science cell (see Fig. 1.4), with the axis aligned along the y direction. After the manipulation, while the atoms are falling under the effect of the gravitational field, the quantization axis is set along y by a bias field of $B_y = 1\,\mathrm{Gauss}$, and a current pulse of $16\,\mathrm{Amps}$, $10\,\mathrm{ms}$ long, is sent through the coils. After further $13\,\mathrm{ms}$ of free falling we turn on our detectors, i.e. we perform an absorption imaging procedure, taking a picture of separated atomic clouds.

In the absorption imaging the shadow cast in a probe beam due to the absorption by the atoms is imaged on a CCD camera. In order to ensure a strong absorption process, and thus a large signal-to-noise ratio, the probe beam is resonant with the transition $|F = 2\rangle \rightarrow |F' = 3\rangle$ (see section 1.2.2), and σ^+ polarized.

When a beam propagating along x direction, with an intensity profile $I_0(y, z)$, crosses an atomic cloud with spatial density $n(\boldsymbol{r})$, the transmitted beam intensity is given by

$$I_t(y, z) = I_0(y, z) e^{-\sigma \int n(\boldsymbol{r}) dx} \tag{1.18}$$

where $\sigma = 3\lambda^2/2\pi$ is the resonant absorption cross section. Using the above equation, and taking images of the probe beam profile with and without the atoms, one can extract the column atom density $\widetilde{n}(y, z) = \int n(\boldsymbol{r}) dx$. Actually,

in order to avoid offset errors due to spurious light sources, it is also useful to take a "dark" image I_d, which consists in an image with no atoms, nor imaging beam. The final column density, corrected by the CCD camera pixel area, and the magnification of the optical system, is given by

$$\widetilde{n}(y,z) = -\frac{A}{\sigma M^2}\ln\left(\frac{I_t - I_d}{I_0 - I_d}\right) \tag{1.19}$$

The integral of this quantity over all pixels gives the total number of atoms. However, to determine a cloud population we prefer to measure relative-quantities, excluding the influence of the sensor features.

In the actual imaging procedure we illuminates the cloud for $25\,\mu$s with a pulse of only imaging light propagating along x, parallel to a bias magnetic field of $B_x = 1\,$Gauss. The shadow projected on the CCD camera comes from the atoms in the $F = 2$ manifold, which at this point, have accumulated enough recoil to be blown away from BEC. A successive equally long pulse of imaging light it's used to record the beam profile with no shadows.

A third image is taken by simultaneously illuminating the atoms with the imaging and repumping light, again for $25\,\mu$s. In this case the shadow is produced by the atoms in the $F = 1$ manifold. Successively, an equal imaging and repumping light pulse gives the beam profile with no shadows. Finally we take the dark image. In Fig. 1.7 we show a typical image recorded by our procedure after a free-falling time of $24\,$ms during which we also performed the Stern-Gerlach discrimination.

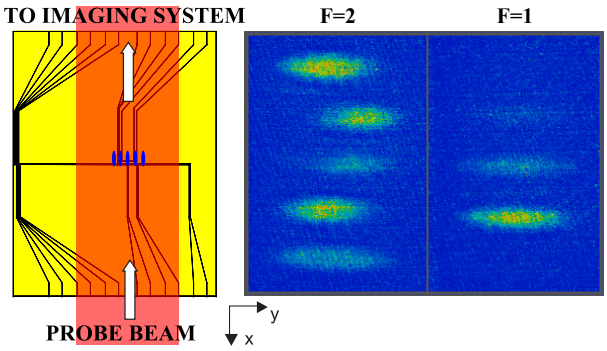

FIGURE 1.7: Left side: Layout of the probe beams to image of the atom cloud. The beam is horizontal to chip surface and perpendicular to the axial shape of the cloud. Right side: example of false colour absorption images of Stern-Gerlach separated cloud, in the two hyperfine manifolds.

1.4.3 Experimental parameter setup

In a typical experimental situation, we need to accomplish some desired manipulation on the internal state of the atoms, which evolution is described by

Eq. 1.16. As a consequence, we have to precisely tune the values of the set of parameters $\Gamma = \{\Omega, \omega_{RF}, \mathrm{B}\}$ appearing in this equation, and uniquely identifying the atomic Hamiltonian. While setting ω_{RF} is a straightforward task, the procedure to set the Rabi frequency Ω and the magnetic field B is slightly more involved. The *sensor* we use to adjust both the parameters is the same BEC we manipulate, in particular, Ω can be adjusted by observing some number of Rabi oscillations, and B by means of Ramsey spectroscopy. In the following we will detail this two procedure, restricting our attention to the dynamics in the only $F = 2$ sub-manifold, i.e. where we produce our BEC.

Rabi oscillations

Applying to the chip antenna for a time τ a radio-frequency signal $s(t) = A\cos(\omega_{RF}\, t)$ with constant amplitude A, and frequency ω_{RF} resonant with the levels energy distance, the atoms in the BEC coherently oscillates between the $|m_f = +2\rangle$ and $|m_f = -2\rangle$ sub-states, passing through all the intermediate levels. For example, left side of Fig. 1.8 shows the oscillations of the five relative populations $p_{m_F}(\tau) = N_{m_F}(\tau)/N_T(\tau)$, N_{m_F} is the number of atoms recorded in each m_f sub-level, and $N_T(\tau) = \sum_i N_i(\tau)$ is the total number of atoms, as measured in the experiment.

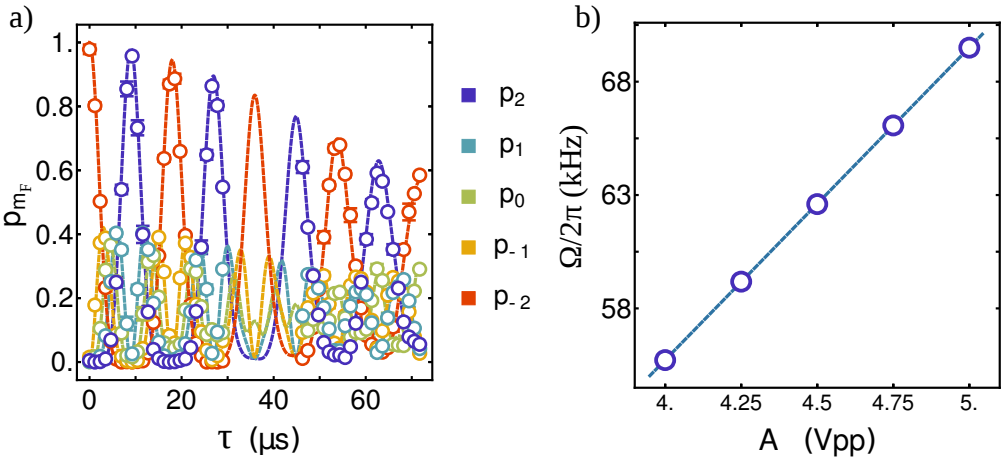

FIGURE 1.8: a) Rabi oscillations in the $F = 2$ manifold as a function of the radio-frequency pulse length $\tau_n = 2\pi\, n/\omega_{RF}$, n being an integer number. Each point with error bars represents the mean values and standard deviation calculated from five experimental realizations under the same conditions. Using Ω as free parameter, we fit the theoretical evolution to the collected data, obtaining the result represented with dashed line. b) Rabi frequencies Ω resulting from fitting the evolutions produced by different radio-frequency signal amplitude A, and linear fit of the data, which yields $\Omega/2\pi \simeq 13.78\, A\,\mathrm{kHz/V}$.

The oscillations are described by Eqs. 1.16 . In particular if we integrate this set of differential equations leaving Ω as free parameter, we can fit the theoretical evolution to the experimental data, obtaining a correspondence between the amplitude A and the strength of Ω.

Then, if we measure the oscillations induced by radio-frequency signals at different amplitudes and fixed $\omega_{RF} = 2\pi\, 4.323\,\mathrm{MHz}$, by fitting the data we obtain the dependence of Ω by A, as shown in the right side of Fig. 1.8. A linear of the data yields $\Omega/2\pi \simeq 13.78\, A\,\mathrm{kHz/V}$ for this configuration, in which the external bias magnetic field is directed along the $\hat{y}$ direction, and the local magnetic field induced by the radio-frequency signal along $\hat{x}$.

As we said at the beginning of this section, the value of ω_{RF} chosen it's resonant with the sub-level energy splitting induced by the magnetic field $B = 6.1794\,\mathrm{Gauss}$, therefore to measure on-resonance Rabi oscillations we need to adjust B at this value. In order to perform a preliminary tuning of B we check that, changing the current sent to the bias coils involved, the radio-frequency pulse with the chosen A and time length shorter than half a Rabi oscillation, transfers the maximum number of atoms towards the $|m_f = -2\rangle$ sub-level. Using this method we have an accuracy in determining B of about $\Delta B \sim 10\,\mathrm{mGauss}$ at best, which is sufficient to measure several resonant oscillations for an accurate determination of Ω.

Ramsey spectroscopy

We perform time domain Ramsey spectroscopy to tune the value of the magnetic field at some desired value. The spectroscopy sequence consists in three phases: a first (preparation) radio-frequency pulse that creates a symmetrical superposition around the $m_f = 0$ sub-state, a free evolution time T_B in which each sub-state accumulates a phase under the effect of only the magnetic field, and a second (recombination) pulse [27]. The final state superposition, and thus the relative populations p_{m_F}, will depend by the different phases acquired during T_B by each m_f sub-state, as shown in left side of 1.9.

The two pulses used in the sequence are equal and defined by the parameters $\Omega = 2\pi\ 60\ \mathrm{kHz}$, $\omega_{RF} = 2\pi\, 4.323\,\mathrm{MHz}$, and a time-length of $\mathrm{T}_P = 2\pi\, 18/\omega_{RF}$ ($\mathrm{T}_P \simeq 4.16\,\mu\mathrm{s}$). The magnetic field is constant through the whole sequence, and dependent on the current I_B applied to the external Helmholtz coils. Using $\mathrm{T}_B \gg \mathrm{T}_P$ the final population distribution is more sensitive to the phases acquired during the free evolution, than to the preparation and recombination phases, where imperfections in the experimental settings can introduce uncertainty in the determination of B.

As in the case of the Rabi oscillations, to describe the dynamics during the three phases we numerically integrate Eqs. 1.16, this time leaving B as free parameter. Then fitting the theoretical evolution to the experimental data we are able to link I_B and B. In the right side of Fig. 1.9 are shown the magnetic

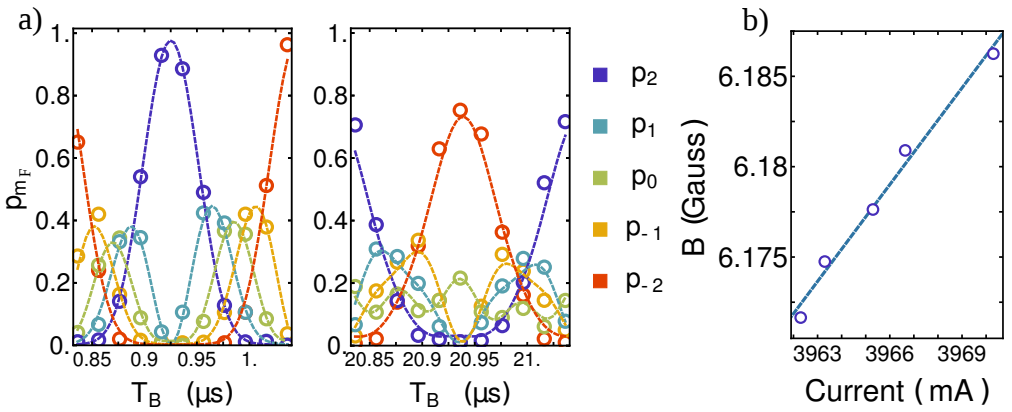

FIGURE 1.9: a) Ramsey fringes of the $F = 2$ hyperfine levels in two time windows. Each point with error bars represents the mean values and standard deviation calculated from five experimental realizations under the same conditions. B is the free parameter to fit the collected data with the theoretical evolution. The fit result is represented with dashed line. b) Magnetic field B resulting from fitting the fringes produced by different currents I_B, and linear fit of the data, which slope is $B \simeq 1.727\, I_B\,\mathrm{Gauss/A}$.

fields measured in correspondence of different values of I_B. A linear fit of the data gives a slope $B \simeq 1.7269\, I_B\,\mathrm{Gauss/A}$.

To determine B, we typically set a current value, measure the interferometer output behaviour, and then we pass to the next value of current. In this way from one set of measurements to the next we are influenced by the slow drifts of the environmental magnetic field, which appear as noise in Fig. 1.9. We have to notice that B is known with a precision of few mGauss if we fit a single set of data related to one value of current I_B, while, as a consequence of the slow drifts, the uncertainty goes above $10\,\mathrm{mGauss}$ in the case of linear fit of the results which belongs to different interferometers.

Chapter 2

Quantum state reconstruction

In this chapter I will present our protocol for the reconstruction of the internal quantum state af an ^{87}Rb atom. Beyond the significant role that this kind of tools plays in the context of quantum information processing, I will directly make use of it in the following chapters, to corroborate our experimental results. Unlike most of the common quantum tomography schemes, our procedure does not require stringent constraints on the family of measurement to perform on the unknown state to estimate, but relies on time-resolved measurements of the atomic population distribution while it dynamically evolves under the influence of a known driving field. After a general theoretical introduction to the quantum estimation problem, I will introduce our approach and its connections to a standard tomography procedure. Then, in the last section, I will present the experimental results of two particular reconstructions, and how the estimation accuracy is influenced by the amount of data collected.

The result reported in this chapter were published in [28].

2.1 Quantum state tomography

The goal of quantum state tomography (QST) is to obtain an estimation of an unknown quantum state, a problem that can be traced back to the dawn of quantum mechanics, and has become popular in the fields of quantum computation and quantum information science [7, 29]. Most of the efforts in this two fields are pointing toward possible implementations of a quantum computer, and many proposals based on different quantum systems were already developed. As a consequence of this growing number of "quantum architectures", it doesn't exist a general QST algorithm or method that can be used in all the cases, but rather many system-specific procedure: optical homodyne tomography of electromagnetic fields [30], recently extended to ultracold atoms [31], "spin tomography" protocol derived in the optical homodyne framework [32], atomic density matrix characterization [33], Josephson qubit tomography [34], to name few examples. However, for synthesis duty, hereafter we will restrict our attention to the atomic case only.

All the estimation schemes developed can be broken down into the following two phases:

(i) Measure of some set of observables a sufficient number of times in order to determine the statistical properties (mean and standard deviation) of the related outcomes.

(ii) Search of the state which better reproduce the collected data.

Both this steps can be carried out with a certain degree of freedom. Regarding the first, for example, we may choose between a weak-continuous measurement protocol on a single ensemble of atoms [35], or a series of independent destructive perturbations to perform on many identically prepared copies of the unknown state. Once one of the two schemes is chosen, we can almost freely decide the set of (eventually continuous) measurements to use, having care to fulfil the prescription of informationally completeness of the operator basis in order to have a good estimation of the initial state. This method was stated for the first time by Fano in the 1950s [36], who introduced the concept of quorum.

From the experimental side, every measurement operator correspond to a precise subset of physical parameters, like orientation of magnetic fields, laser light intensity, phase between radio-frequency fields, and so on, thus a considerable amount of work has to be dedicated to reproduce accurately the whole family of operators.

In the second step, the system state has to be deduced from the set of collected data, which in general is always affected by the noise coming from the external environment, and by the uncertainties on the experimental parameters. In particular, we have to choose an estimator that, from the statistics of the input data, gives us an estimation of the unknown state. Many options have been developed, like simple linear inversion [37], least square minimization [38], maximum-likelihood estimation [33], Bayesian mean tomography [39, 40], minimax mean estimation [41], and so on, and so forth. According to the set of measurements used and the number of data available, one choice is more suitable than another, but no general formula exist.

Before introducing our proposal for a QST protocol, I will briefly introduce the simpler tomographic scheme, the linear inversion, and the most widely used method in the atomic field, i.e. the maximum likelihood estimation.

2.1.1 Linear inversion

Consider the case of a d-dimensional Hilbert space where quantum states, when described by density matrix operators, are uniquely specified by $d^2 - 1$ parameters. One approach which can be adopted to assess these parameters is to observe the states through quantum measurement operators.

The most common description of an observable in quantum mechanics is by means of projection operators, which can be thought as ideal, perfect measurements of a quantum system. Suppose we have, in the experimental setup, M measurement channels Π_j , each one associated to a projector

$$\Pi_j = |y_j\rangle \langle y_j| , \quad j = 1 \dots M. \tag{2.1}$$

Let us denote with the physical quantities o_j the possible measurement outcomes of the (projective) channels. We can then define the observable O composed by the set $\{\Pi_j\}$ together with the outcomes o_j

$$O = \sum_{j=1}^{M} o_j \Pi_j. \tag{2.2}$$

As an example, these observables can correspond to the magnetic moment projections along the z direction of a spin-F system, and are detectable by using a Stern-Gerlach setup identical to our measurement system (see section 1.4.2).

The quantum object we observe is a dilute BEC containing N non-interacting atoms, formally equivalent to an ensemble of N identical copies of the same quantum state ρ. The action of O on this ensemble, using the definition 2.2, gives as result the quantity

$$\left\langle \sum_{i=1}^{N} O \right\rangle = \mathrm{Tr}\left[\sum_{i=1}^{N} O\rho \right] = N \sum_{j=1}^{M} o_j p_j , \tag{2.3}$$

where $p_j = \mathrm{Tr}\left[\Pi_j \, \rho\right]$ is the probability of a single atom to be detected in the measurement channel j, and it depends only on the elements of the density matrix ρ once the measurements Π_j are normalized. When the number of atoms N is statistically relevant, we can approximate the probability p_j with the relative number of atoms $f_j = n_j/N$ experimentally detected by the j-th channel, and from the realistic set of equation

$$f_j = \mathrm{Tr}\left[\Pi_j \rho\right] = \langle y_j \, |\rho| \, y_j \rangle , \quad j = 1 \dots M, \tag{2.4}$$

we might be tempted to extract the unknown matrix elements of ρ. Of course, a first constraint is given by the number of equations and unknown parameters involved, which imposes to have a number of measurement channels equal to the unknown parameters in ρ , i.e. $M = d^2 - 1$. However, without any other constraint, these equations have generally no physical solutions, i.e. they do not lead to semi-positive definite hermitian operators describing physical states.

The non-hermitianity of the unknown ρ can be prevented imposing the linear parametrization

$$\rho = I/d + \sum_{k=1}^{d^2-1} s_k S_k, \quad s_k \in \mathbb{R} \tag{2.5}$$

where S_k are members of an orthonormal Hermitian basis of traceless operators, and s_k the unknown parameters to identify. Furthermore, to be confident of being able to reconstruct the entire ρ from the measurements, we can use a more complex set of $M = d^2 - 1$ non-commuting operators $\{\Pi_j\}$ such that $\Pi_j \geq 0$ (positive operator) and $\sum_j \Pi_j = I$ (informationally complete, or IC, set). An example of such set for a spin-$1/2$ system are the Pauli matrices with the identity $\mathcal{S} = \{\sigma_1, \sigma_2, \sigma_3, I\}$. The σ_is correspond to projection of three mutually orthogonal spin components ($\sigma_x, \sigma_y, \sigma_z$), which are physically detectable by Stern-Gerlach apparatus oriented along the principal directions.

If we adopt the parametrization in Eq. 2.5, Eq. 2.4 then reads

$$f_j = \mathrm{Tr}\left[\Pi_j\right]/d + \sum_{k=1}^{d^2-1} s_k \,\mathrm{Tr}\left[S_k \Pi_j\right] . \tag{2.6}$$

By defining the vector of coefficients $\widetilde{f}_j = f_j - \mathrm{Tr}\left[\Pi_j\right]/d$, and the matrix of entries $\widetilde{\Pi}_{jk} = \mathrm{Tr}\left[S_k \Pi_j\right]$, we can write Eq. 2.6 in vector notation

$$\widetilde{\boldsymbol{f}} = \widetilde{\boldsymbol{\Pi}} \cdot \boldsymbol{s} \,. \tag{2.7}$$

Finally, it can be shown that whenever the set $\{\Pi_j\}$ fulfil the IC requirement stated above, then the matrix $\widetilde{\boldsymbol{\Pi}}$ is invertible [42], which leads to substitute in Eq. 2.5 the coefficients s_j obtained inverting Eq. 2.7. We then obtain the density matrix estimation

$$\rho = I/d + \sum_{k=1}^{d^2-1} (\widetilde{\boldsymbol{\Pi}}^{-\mathbf{1}} \cdot \widetilde{\boldsymbol{f}})_k S_k \tag{2.8}$$

which is by construction Hermitian and normalized, and in the absence of noise, semi-positive definite. However, in practice, there is always noise in real measurements, thus the estimation will often leads to not semi-positive definite density matrices.

2.1.2 Maximum likelihood estimation

Maximum likelihood (ML) is the most commonly used tomography reconstruction method which avoid estimating non-physical states [33].

Suppose we experimentally implemented a set of $M = d^2 - 1$ measurement apparata corresponding to the IC set of positive operators $\{\Pi_j\}$ ($\sum_{j=1}^{M} \Pi_j = \mathbb{1}$, $\Pi_j \geq 0$), and let use the members of this set to compose the observable O as in Eq. 2.2. In correspondence of the measurement of O on a single atom described

by the unknown density matrix ρ, one among the M physical apparata clicks. Repeating the measurement of O on N identically prepared copies of the atomic states ρ, we obtain an history of detections in which each output channel j clicks n_j times. Obviously $\sum_j n_j = N$. The probability of the outcome j depends by the density matrix via the usual relation $p_i = \mathrm{Tr}\left[\Pi_j \rho\right]$, so the overall probability of a recorded clicks sequence is given by the likelihood functional

$$\mathcal{L}\left(\rho\right) = \frac{N!}{\prod_i n_i!} \prod_j \mathrm{Tr}\left[\Pi_j \rho\right]^{n_j} \ . \tag{2.9}$$

Once the occurrences n_j are extracted from the history record and substituted in Eq. 2.9, we have a functional which quantifies the degree of belief in the hypothesis that the initial state of the system was ρ. The aim of ML estimation it is to selects that particular ρ for which the likelihood attains its maximum value according to the recorded data.

As a classical example, we can imagine to toss a coin N times, recording 50 times a head, and 50 times a tail. The likelihood functional in this case is $\mathcal{L} \propto \left(p_h p_t\right)^{50} = p_h^{50}\left(1 - p_h\right)^{50}$, which of course is maximum when the probabilities of tail and head are equal, $p_h = p_t = 0.5$ (see Fig. 2.1).

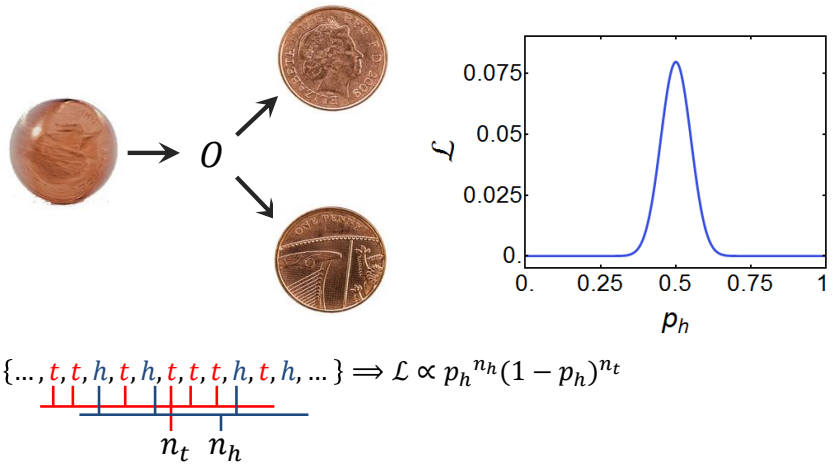

FIGURE 2.1: Pictorial representation of the maximum likelihood estimation for the fair coin flip process. The coin "observed" by O gives as result head (h) or tail (t). Repeating N time the toss, we record a sequence of outcomes in which h appears $n_h \simeq 0.5N$ times, and the same for t ($n_t \simeq 0.5N$). Accordingly, a plot of the likelihood function respect to p_h shows a maximum in correspondence of $p_h = 0.5$.

In the case of a density matrix, the maximization of $\mathcal{L}$ is not straightforward as for a coin, but many algorithms are available and well documented. Most of them recasts the maximization in a fixed points problem, and solve the semi-definite positivity issue by decomposing ρ as $\rho = A^\dagger A$, where A is a lower triangular matrix.

2.2 Our proposal

The theoretical frame of the schemes above mentioned are well developed, and they leave no room for doubt with respect to the capability of reconstructing unknown states, giving in some cases also an estimation of the reconstruction error. Despite this reliability, the necessary condition for the set $\{\Pi_j\}$ to be informationally complete often prevents a straightforward experimental realization of the procedure. In fact each projector correspond to a physical measurement apparatus which has to be appropriately designed, and all together the apparatus must be carefully tuned to fulfill the completeness condition. A further complication is given by the fact that, in the general case of an N $d-$level system, the density matrix ρ is described by a linear combination of direct products $\prod_{i=1}^{N} s_k^{(i)} S_k^{(i)}$, thus the number of measurement apparatus needed to determine the s_k^i parameters exponentially increases as d^{2N}.

Conversely, the tomographic procedure we propose is straightforward, since all the essential tools used are commonly employed in almost every cold-atoms experiment. For example in our case it does not require any further improvement of the pre-existing experimental set-up. The idea is simple:

(i) The only observable we measure is the projection of the atomic spin along the quantization axis, $O = F_z$. The measure of O is performed after a controlled evolution of the unknown state to be reconstructed. We repeat this step changing in an appropriate range the controlled evolution time τ preceding the measurement of O.

(ii) The dynamics of the same observable is numerically simulated starting from a randomly chosen initial state. We run an optimization protocol that minimizes the difference between the simulated and measured data in such a way that the optimal solution provides the tomographic reconstruction of the initial state – see also the reconstruction protocols in Refs. [35] and [38].

Both the **data collection** step (i), and the **data analysis** step (ii) are simpler to perform respect to other solutions of the estimation problem, resulting in a quick, robust, and experimentally accessible methodology, in which there are no many theoretical subtleties to take into account.

We now analyse in details the two steps.

Data collection

Hereafter we restrict our attention to states in the 5-fold hyperfine level $F = 2$. As mentioned above, we want to estimate the unknown density matrix of a single atom by measuring the projections of the atomic spin along the quantization axis. The related observable is the traceless operator $O = F_z =$

$\sum_{m_F=-2}^{+2} m_F \Pi_{m_F}$, where $\Pi_{m_F} = |m_F\rangle \langle m_F|$, which is physically measured via a Stern-Gerlach discrimination followed by an absorption imaging sequence. We recall from section 1.4.2 that, given the destructive nature of the absorption imaging, in each experimental cycle we can perform only one measurement of O, and that ideally this couples uniformly to the BEC, which contains up to $N = 10^5$ non-interacting atoms in the same state ρ . It follows that one observation on one BEC gives as result 5 atomic populations n_{m_F} , but it can be thought as N observations on N identical copies of ρ , i.e. $\langle \Pi_{m_F} \rangle_{BEC} = NTr\left[\Pi_{m_F}\rho\right]$. In other words, for a non-interacting BEC, measuring the number of atoms in each sub-level is equivalent to measuring the probability for each atom to occupy any of the sub-levels.

Let we suppose that, after an unspecified manipulation, the BEC (not necessarily pure) state is described by the unknown density operator $\rho_0 \equiv \rho(t=0)$, which we aim to reconstruct. Instead of measuring F_z directly on ρ_0 , we use this state as initial condition for an accurately controlled coherent evolution, then, after evolving for a time τ, we measure the 5 atomic populations $n_{m_F}(\tau)$ and calculate the relative frequencies with which the atoms are observed in the m_F channels, i.e. by the relative populations

$$f_{m_F}(\tau) = \frac{n_{m_F}(\tau)}{N}. \tag{2.10}$$

For "accurately controlled" we mean that we are able to perfectly determine the full Hamiltonian H of the atoms by experimentally controlling all the parameters in it. If we also assume that for each experimental cycle we are able to start exactly from the same ρ_0 we want to reconstruct, then we can repeat many times the process of controlled evolution and measurement, calculating the mean values $\overline{f_{m_F}(\tau)}$ and the standard deviations $\sigma_{m_F}(\tau)$ of the outcomes. Furthermore, changing τ from one realization to another we gather the set of data $\left\{ \overline{f_{m_F}(\tau_i)} \right\}$, representing the relative frequencies behaviour as a function of the evolution time, sampled in correspondence of the times τ_i. An example of data set recorded is shown in Fig. 2.3. The time window T in which the τ_i are chosen, has to be enough wide in order to observe a non trivial dynamics, so it can be the natural evolution time scale of the system, and the number of data collected can be just sufficient to resolve such dynamics.

Data analysis

From the theoretical point of view, in the case of unitary evolution, one has $\rho(t) = U(\tau)\rho_0 U(\tau)^\dagger$ with $U(t) = e^{-iHt}$, and H, again, is perfectly known. If the system is, instead, subjected to a noisy evolution, as it is in most experimental situation, one has $\rho(t) = \Phi_t\left(\rho_0\right)$, with $\Phi_t(\rho)$ being the so-called quantum map, or quantum channel [43].

The probability to register an outcome in the channel m_F, after the evolution time τ , and starting from an arbitrary state ρ, is given by the formula

$$p_{m_F}(\tau, \rho) = \mathrm{Tr}\left[\Pi_{m_F} \Phi_\tau\left(\rho\right)\right] \tag{2.11}$$

Given the numbers of our BEC, we can postulate that the probabilities $p_{m_F}(\tau, \rho_0)$ associated to the initial unknown ρ_0 are well approximated by the relative frequencies with which the atoms are experimentally observed in the m_F channels, i.e. $p_{m_F}(\tau_i, \rho_0) \approx \overline{f_{m_F}(\tau_i)}$. For any other ρ this condition will not hold. We can then define an overall error between measurements and theoretical prediction

$$\epsilon(\rho) = \sum_{m_F, i} \left\| p_{m_F}(\tau_i, \rho) - \overline{f_{m_F}(\tau_i)} \right\| \tag{2.12}$$

with $\|\cdot\|$ being any mathematical norm.

Our estimation procedures consists in a least square minimization of Eq. 2.12 in order to find the positive matrix which better reproduce the experimental data. The minimization algorithm we have implemented is based on the Subplex variant of the Nelder-Mead method [44]. In particular, to take into account also the experimental uncertainties, we minimize, with respect to ρ, the following weighted mean squared error function

$$\epsilon(\rho) = \frac{1}{5} \sum_{m_F} \sqrt{\left(\sum_i \omega_{m_F,i} |\overline{f_{m_F,i}} - p_{m_F,i}\left(\rho\right)|^2 \right) / \sum_j \omega_{m_F,i}} \,, \tag{2.13}$$

where $p_{m_F,i}\left(\rho\right) \equiv p_{m_F}\left(\tau_i, \rho\right)$ and analogously is for $\overline{f_{m_F,i}}$, while $\omega_{m_F,i} \equiv 1/\sigma^2_{m_f}(\tau_i)$. The density matrix $\boldsymbol{\rho_E}$ in correspondence of which $\epsilon(\rho_E)$ is minimal is our estimation of ρ_0. The constraints of Hermitianicity and positiveness of the output density matrix are inserted in the minimization algorithm as a penalty function which automatically excludes the non-physical results.

2.2.1 Link with standard estimation methods

We want to show how our strategy can be reconnected to a standard reconstruction procedure. To simplify the description, we assume that the controlled dynamics is unitary, thus the evolution of ρ_0 reads $\rho(t) = U(\tau)\rho_0 U(\tau)^\dagger$. Replacing this relation in Eq. 2.11, and making use of the cyclic invariance of the trace, we can write

$$p_{m_F}(\tau, \rho) = \mathrm{Tr}[\Pi_{m_F}(\tau)\rho], \tag{2.14}$$

where $\Pi_{m_F}(\tau) = U(\tau)^\dagger \Pi_{m_F} U(\tau)$ is a projection operator rotated in time.

Again, approximating $p_{m_F}(\tau, \rho_0) \approx f_{m_F}(\tau)$, and gathering data in correspondence of the evolution times $\{\tau_i\}$, we get the set of equations

$$f_{m_F}(\tau_i) = Tr\left[\Pi_{m_F}(\tau_i)\rho_0\right], \tag{2.15}$$

which is formally equivalent to Eq. 2.4. With proper choice of the Hamiltonian generating the time evolution, and the set of sampling times $\{\tau_i\}$, it is possible to derived a complete set of observable $\{\Pi_{m_F}(\tau_i)\}$ which can be used, for example, for a maximum-likelihood estimation of ρ_0. Due to this equivalence, also our method suffers the problem of exponential growth of the complexity with the system size, however the efforts could be scaled back by the fact that the attention is now focused on the engineering of a dynamical evolution, instead of many measurement apparatus.

2.3 Experimental Results

To test the scheme proposed here, we have prepared, by applying known Hamiltonian evolutions, a set of states to be estimated. Since the preparation can be affected by experimental errors, the real states can be different from the expected.

The central and indispensable assumption of the reconstruction procedure, is the capability to accurately control the coherent dynamics of the atomic system. For this purpose it is necessary to tune all the experimentally accessible parameters in the Hamiltonian H describing the atoms, which is given, in presence of an uniform magnetic field and a radio-frequency driving, by Eq. 1.14. Let us recall that the parameters we are able to control in H are: the strength of Ω by changing the amplitude A of the radio-frequency signal $s(t) = A\cos(\omega_{RF}t)$ applied to a chip wire, the radio-frequency ω_{RF}, and the magnetic field B by means of the current I_B flowing in a couple of external Helmholtz coils. The radio-frequency ω_{RF} is directly selectable on the function generator we use to produce $s(t)$, while Ω and B has to be tuned following the procedure detailed in section 1.4.3. Once that Ω, ω_{RF}, and B are specified, then H is uniquely identified. For consistency, in all the reconstruction performed we decided to use the same values for these parameters, i.e. $\boldsymbol{\Omega = 2\pi\,60\,\mathrm{kHz}}$, $\boldsymbol{\omega_{RF} = 2\pi\,4.323\,\mathrm{MHz}}$, and $\mathbf{B = 6.1794\,Gauss}$. Note that the values of B and ω_{RF} chosen involves resonant oscillation, but until it is possible to observe a nontrivial dynamics, also a non vanishing detuning does not affect the reconstruction procedure. In the following we will refer to the radio-frequency pulse determined by the chosen parameters as "reconstruction pulse".

The evolution of the atomic density matrix is described by the dynamical equations 1.16, which includes the presence of pure dephasing on the non-diagonal terms of H. In particular, integrating this set of differential equations

over time with the initial condition $\rho(t=0)=\rho$, using the above fixed set of parameter $\{\omega_{RF},\Omega,\mathrm{B}\}$ and an effective dephasing rate $\gamma = 2\pi\,200\,\mathrm{Hz}$, we obtain the quantum map $\rho(t)=\Phi_t(\rho)$ which can be substituted in Eq. 2.11 to simulate the probabilities behaviour.

The tests was performed as follows. In each experimental cycle, by using a carefully designed control evolution, we prepare the BEC in a desired target state described by the density operator ρ_0 (the next chapter will be devoted to the arbitrary states preparation). This preparation is carried out by driving the system dynamics with a properly engineered radio-frequency pulse, under the same constraints of B and Ω used for the reconstruction pulse. The preparation evolution is immediately followed by the reconstruction pulse, which drives the system dynamics for a time τ_i typically in the range $0\,\mu\mathrm{s}\leq\tau_i\leq T$, where $T\sim 11\,\mu\mathrm{s}$ is comparable with the system natural evolution timescale ($T\sim\pi/\Omega$)[1]. In some cases, for a more detailed analysis of the states reconstruction performance, we used evolution time until $T=100\,\mu\mathrm{s}$. We repeated this experimental sequence by changing τ_i from one realization to the next. The set of data collected was then analysed with the least square minimization algorithm implemented, obtaining the estimation ρ_E and the residual error $\epsilon(\rho_E)$ between the measurements and reconstructed dynamics. Finally we use our knowledge on the fiducial density matrix ρ_0 to compute the Uhlmann fidelity $\mathcal{F}(\rho_0,\rho_E)$ [45], in order to a posteriori verify the goodness of the reconstruction. Let us stress that no a priori knowledge of the initial state has been used for the tomographic reconstruction. However, this information has been exploited to calculate the Uhlmann fidelity.

We reconstructed several states, some of them obtained after a long preparation and thus markedly non-pure, some other having random density matrix elements, always obtaining reconstruction fidelities $\mathcal{F}\geq 0.95$. In the following sections we will show the results of two particular cases, and then we will analyse the reconstruction performance as a function of the amount of collected data.

Reconstruction of the pure state $|F,m_F\rangle = |2,+2\rangle$

The first example we show is the reconstruction of the BEC state right after the condensation, i.e. the pure state $|F,m_F\rangle = |2,+2\rangle$. In the right part of Fig. 2.2 we represent by a bar plot the density matrix ρ_0 of this state. The mean values (standard deviations) of the population distribution measured as a function of τ_j are represented by points (error bars) in fig 2.3. We sampled the dynamics in a time window approximately $11.5\,\mu\mathrm{s}$ long, every five oscillations of the radio-frequency field, i.e. $\tau_j = j\,5/4.323\,\mathrm{MHz}\sim 1.15\,\mu\mathrm{s}$. The estimated

[1]Note that, representing a state on a multi-dimensional Bloch sphere, given the experimental parameters used here, the controlled evolution of the dynamics is almost equivalent to a rotation about the "x" axis by an angle $\Omega\,T = 1.38\,\pi$.

density matrix ρ_E is represented in the left part of Fig. 2.2, and its fidelity with ρ_0 is $\mathcal{F}(\rho_0, \rho_E) = 0.98$, while the residual error between experimental data and reconstructed dynamics is $\epsilon(\rho_E) = 8.5 \times 10^{-3}$. In Fig. 2.3 we also shown the simulated dynamics with initial condition ρ_E on the left part, ρ_0 on the right, both well reproducing the experimental data.

We note that in principle this state it can be reconstructed by only one measurement at $\tau = 0$, with fidelity $\mathcal{F} = 1$. Thus it's here clear that, since the algorithm try to find a compromise reproducing the behaviour of the whole data set, which is affected by the unavoidable experimental noise, then also the initial point will suffer of this approximation.

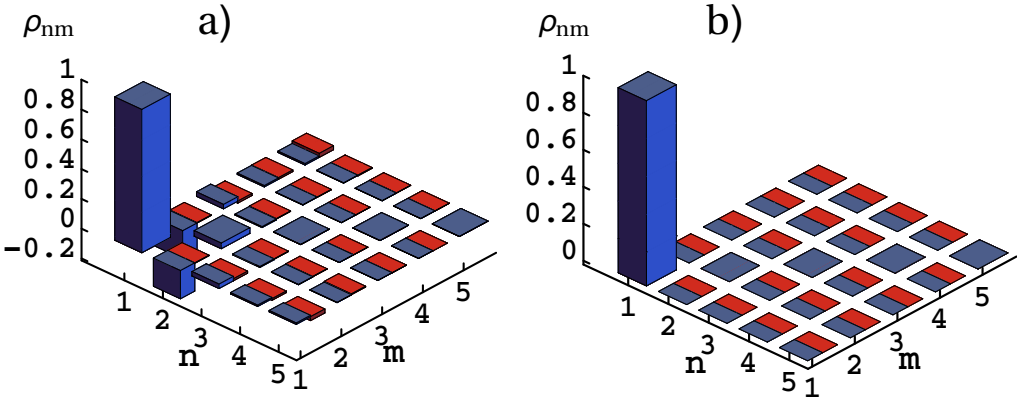

FIGURE 2.2: Pure state $m_F = +2$: Pictorial representation of the reconstructed density matrix ρ_E (a) and the theoretically expected one ρ_0 (b), with the real (blue) and the imaginary (red) components. The Uhlmann fidelity $\mathcal{F}(\rho_0, \rho_E)$ between ρ_0 and ρ_E in is $\mathcal{F} = 0.98$.

Reconstruction of a coherent superposition

The second example we show is the reconstruction of a coherent superposition, obtained after a $\pi/2$ rotation from the pure state $|F, m_F\rangle = |2, +2\rangle$. In particular this state, whose correspondent density matrix ρ_0 is represented in Fig. 2.4, is demonstrated to maximize the fringe visibility of a multi-state interferometer [46], and it is obtained by driving the dynamics with a resonant radio-frequency signal for a time $\Omega\tau = \pi/2$.

The estimated density operator ρ_E is represented in Fig. 2.4, and its fidelity with ρ_0 is a satisfactory $\mathcal{F} = 0.97$. Figure 2.5 shows the set of experimental data used for the reconstruction, recorded with the same time rate of the previous example. In this case the residual error between reconstructed dynamics (shown in the left part of Fig. 2.5) and experimental data is $\epsilon(\rho_E) = 58.4 \times 10^{-3}$.

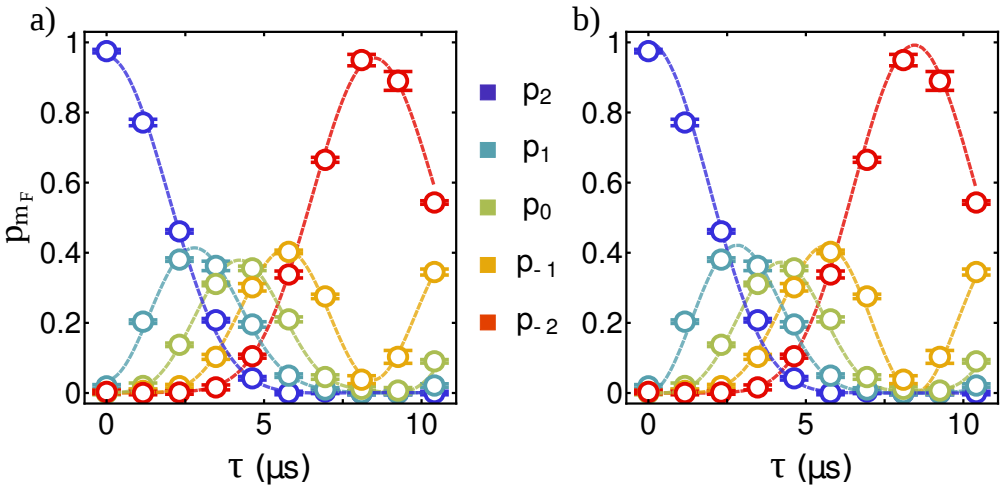

FIGURE 2.3: Time evolution of the atomic populations (points) starting from the $m_F = +2$ pure state as a function of the evolution time τ. Each point is recorded at $\tau_j = 2\pi\, j/\omega_{RF}$, and represents the mean values and standard deviation calculated from five experimental realizations under the same conditions. The superimposed line in panel (a) is the reconstructed evolution with the estimated initial condition ρ_E minimizing the deviation $\epsilon(\rho)$ between experimental and theoretical data. In this case $\epsilon(\rho_E) = 8.5 \times 10^{-3}$. In panel (b) the same data are superimposed to the theoretical evolution starting from the pure state $m_F = +2$. In both the cases the agreement is highly satisfactory.

Observing the superposition of the experimental data with the theoretical behaviour starting from ρ_0 (right part of Fig. 2.5), we note a mismatch between this ideal evolution and experimental outcomes higher than in the case of reconstructed dynamics. Indeed, calculating the error function in correspondence of ρ_0 we get $\epsilon(\rho_0) = 64 \times 10^{-3}$. In this case the algorithm is probably estimating a state which is closer to the real state of the atoms than it is ρ_0.

2.3.1 Reconstruction error convergence

In the above examples we estimated the unknown density matrices ρ_0 by feeding the reconstruction algorithm with set of data obtained from $n_s = 10$ measurements (see Fig. 2.3 and 2.5), uniformly covering a time window $T = 11.5\,\mu$s long. Each measurement record consists of 5 relative populations, so, considering the normalization constraints, we effectively have $4 \times n_s = 40$ data points available. The unknown parameters to estimate are $d^2 - 1 = 24$, so one might think that the reconstruction would still be possible using less data, however we stress that the set of measurement operators used is not informationally complete, so it is not possible to argue the minimal n_s on the bases of only the dimension of the space of parameter to estimate. We then decided to directly

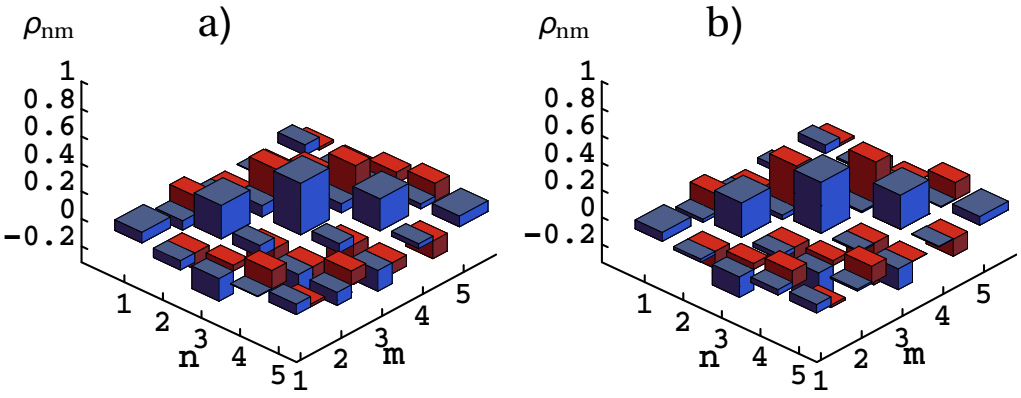

FIGURE 2.4: Coherent superposition obtained by a $\pi/2$ rotation of the pure state $m_F = +2$: a) reconstructed density matrix ρ_E. b) theoretically expected density matrix ρ_0. We represent in blue (red) the real (imaginary) components. The Uhlmann fidelity $\mathcal{F}(\rho_0, \rho_E)$ is $\mathcal{F} = 0.97$.

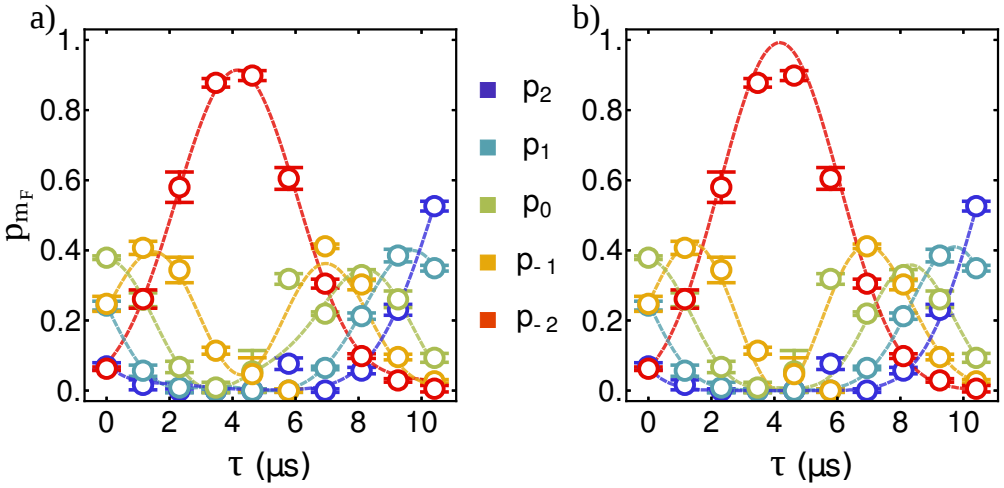

FIGURE 2.5: Time evolution of the atomic populations (points) starting from the coherent superposition obtained by a $\pi/2$ rotation of the pure state $m_F = +2$, as a function of the evolution time τ. Each point is obtained with the same prescription of the previous data set (see Fig. 2.3). We superimposed to the experimental data the reconstructed evolution with the estimated initial condition ρ_E (a), and the theoretical evolution starting from the expected state ρ_0. The reconstruction error is $\epsilon(\rho_E) = 64 \times 10^{-3}$. Also here note the good agreement in both the cases.

asses the reconstruction convergence evaluating the fidelity behaviour with respect to n_s.

For our analysis, we concentrate on the estimation of the coherent superposition in the latter example, collecting a total of 88 samples in a time windows $100\,\mu$s long, with the same sampling rate $\tau_j = j\,5/4.323\,\mathrm{MHz}$ adopted before. We then reconstructed ρ_0 by using a variable number of sequential measurements, starting from $n_S = 2$ to $n_S = 88$. In each case we evaluated the fidelity $\mathcal{F}(\rho_0, \rho_E)$, and the results are shown in Fig. 2.6.

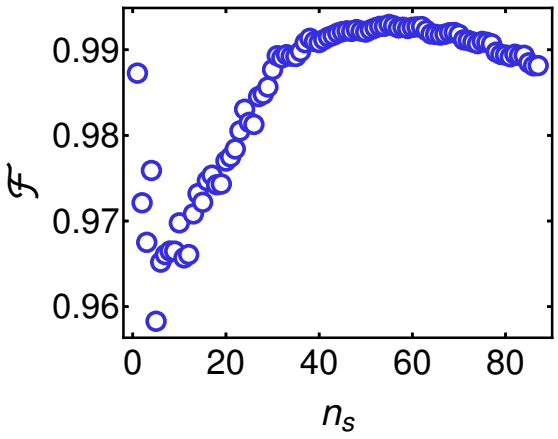

FIGURE 2.6: Fidelity $\mathcal{F}(\rho_0, \rho_E)$ between the reconstructed ρ_E and expected density matrix ρ_0 as a function of the number of samples collected n_s.

From the plot is clear that the fidelity behaviour can be broken down in three regime: For $n_S \leq 6$ the reconstruction outcomes are erratic, due to the fact that $4\,n_S \leq 24$. For $7 \leq n_s \lesssim 55$ with the increasing number of data $\mathcal{F}$ also increases, probably because the set of measurements involved is not complete, but the volume of the space outside their support becomes smaller and smaller. Finally, for $n_S \gtrsim 55$ the noise in the measurements record start to dominate, making the initial prediction more difficult.

To verify the goodness of the reconstruction we a posteriori calculate the fidelity $\mathcal{F}$ exploiting our knowledge of ρ_0. However this information is not available when the state to estimate is *really* unknown. The only output informations given by our algorithm are the estimated ρ_E, and the error $\epsilon(\rho_E)$ which express the accuracy of the reconstruction of the dynamics. To quantify our degree of believe on the estimation based on this last information, we evaluate the link between F and $\epsilon(\rho_E)$. In particular, from the same data set made of 88 records of the previous analysis, we randomly selected groups of n_s non-consecutive measurement, with n_s ranging from 2 to 30. For each n_s we repeated 100 times the random extraction, using each group of measurements obtained to perform the reconstruction. In left side of Fig. 2.7 we show the fidelity between the reconstructed ρ_E and the expected ρ_0 as a function of $\epsilon(\rho_E)$, obtained from each of the 100 sub-group of measurements, selecting some particular n_s.

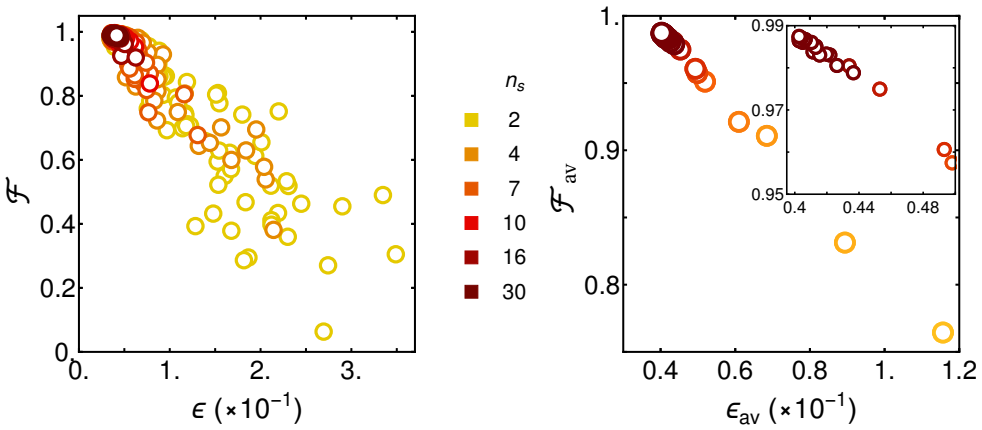

FIGURE 2.7: Left panel: Fidelity $\mathcal{F}(\rho_0, \rho_E)$ calculated by sampling the populations evolution n_S times, at random times in the time windows $0 \div 88\,\mu$s, as a function of the reconstruction error $\epsilon(\rho_E)$. For each n_S we perform 100 random extraction of the sampling time, and report the calculated fidelities in the graph. Right panel: For each group of 100 fidelities we report the mean values as a function of the of the related reconstruction errors mean values. The number of n_S collected ranges from 2 to 30.

We can observe two features: i) A nearly linear dependence of the fidelity on the error. ii) A reduction of the spread of the results in proximity of the maximum fidelity. These two factors clearly show that the uncertainty on the estimated density matrix decreases with the discrepancy between the experimental data and theoretical prediction. This behaviour is even clearer if we plot the mean fidelity $\mathcal{F}_{av}(\rho_0, \rho_E)$ with respect to the mean error $\epsilon_{av}(\rho_E)$ calculated for each n_s subset (left side of Fig. 2.7).

2.4 Conclusions and outlook

In conclusion, we have experimentally demonstrated a tomographic reconstruction procedure that relies on data collected during the evolution of an unknown quantum state. The crucial ingredient of our proposal is the ability to carefully control the system dynamics according to a precisely tuned Hamiltonian, but no constraints are given on the set of measurement to perform, unlike most of the common schemes which require to implement informationally complete set of operators. The advantages of this protocol are the use of quite conventional experimental resources (a Stern-Gerlach discrimination followed by an absorption imaging process), and the simplicity of the post-processing procedure. Furthermore, we have shown how the reconstruction quality behave as a function of the amount of collected data, and how the accuracy of the reproduction of

the population dynamics is a signature of an high fidelity between the expected and the estimated states.

Finally, this technique can be also exploited to get further information on the system evolution, e.g. estimate the amount of dephasing noise in the system dynamics resulting from its coupling to the external environment. Indeed the proposed scheme realizes quantum state tomography but could readily be modified to perform quantum process tomography by assuming complete knowledge of the input states, hence providing a very feasible and useful tool for several quantum technological applications.

Chapter 3

Optimal preparation of quantum states

In this chapter I report on experimental results in which the internal states of a ^{87}Rb BEC are coherently manipulated in order to produce arbitrary superpositions. The manipulation is provided by a suitable designed radio-frequency signal produced by an optimization algorithm called CRAB. Once the manipulation time T and all the relevant experimental constraints are fixed, we are able to prepare, with low error, states which are not encountered during standard Rabi oscillations in the same time T, under the same constraints. We analyse the time limit of our scheme, showing that the error in the states preparation it is proportional to T, until it saturates to a minimum close to 0. This makes our protocol a useful tool to arbitrary initialize an atomic system for further manipulation, before unwanted noise sources destroy the atomic coherences.

Some of the results shown in this chapter were published in [47].

3.1 Arbitrary state preparation and optimal control

The ability to create and manipulate coherent superpositions of internal substates is important in most quantum technological applications. For example, in the field of precision gravity measurement using atom interferometry. To measure the phase shifts induced on a BEC when it falls in the Earth gravitational field, the effects of the residual magnetic couplings has to be minimized. One solution is to populate the non-magnetic sub-levels $|F, m_F = 0\rangle$, perturbed only by the quadratic Zeeman effect [48]. The higher will be the transfer in this states, the greater will be the S/N ratio of the interferometer. One more example is the coherent splitting operation in a Ramsey interferometer [27]. As seen in section 1.4.3, a typical experimental sequence starts with the preparation of the atoms in a given superposition by a splitting pulse, then each m_F component accumulates a phase according to the formula $\Delta\phi \propto m_F \Delta\mathrm{T}\ \mathrm{B}$, where $\Delta\mathrm{T}$ is the accumulation time and B the magnetic field, finally the phases are mapped in a population distribution by a second recombination pulse. These pulses needs

to be properly engineered to maximize the sensitivity to the phase changes during the accumulation time, maintaining a relative robustness to the unwanted experimental parameters fluctuations. Finally, any quantum information process require a proper initialization of the input state. In the hyperfine doublet $F = 1, 2$, usually some particular Zeeman sub-levels are labelled to represent states of a qubit, which are processed by a set of quantum gates [29]. The accuracy of the gate manipulation, greatly depends by the ability to carefully prepare the gate input, i.e. the sub-levels superposition, with high fidelity.

All the previous examples require to fulfil some fidelity criteria, which often means, for quantum systems like BECs, that dephasing effects has to be minimized. In practice, the natural environment of the BEC has properties which continuously fluctuates in time, and some of these fluctuations are noise sources coupled to the quantum system. Typical sources of noise are magnetic field fluctuations, electromagnetic disturbances, stray light, or atomic density variations. The dephasing resulting from these fluctuations can be homogeneous, when the coherences are lost internally and equally for all the atoms, or it can be inhomogeneous, when the atoms dephase one with respect to each other while keeping the internal coherences [49]. Various technics were developed to avoid both this deleterious phenomena. In the case of the homogeneous dephasing the solutions ranges from passive decoupling of the BEC from the environment, to the active control of wavefuntion evolution [50] (and citation inside), while for the inhomogeneous dephasing the spin echo technic is widely used since a long time in several applications [51–53].

In all these contexts, the quantum optimal control strategies can be exploited to transform an atomic system with high fidelity from an experimentally readily prepared initial condition to a desired state which satisfy our demands and that can be further manipulated [54–56]. Moreover they may specifically take account of both single atoms initial condition and environment fluctuations, in order to have a manipulation less sensible to such variations. In the same way, by speeding up the state preparation it is possible to perform coherent tasks before inhomogeneous dephasing processes unavoidably occur [57], and often optimal control allows one to reach the ultimate bound imposed by quantum mechanics, the so-called quantum speed limit (QSL) [58–61]. Optimal control techniques have been successfully implemented in several physical systems, ranging from cold atoms [62] to molecules [63], and recently they have been developed and successfully applied to many-body quantum systems [64–69].

3.2 Optimal control mathematical framework

Let us describe the initial state of a system by the density matrix $\rho(t)|_{t=0} = \rho_0$, and its time evolution by the dynamical equation

$$i\frac{d}{dt}\rho(t) = \mathcal{H}\left[t, \rho(t), \Gamma(t)\right], \tag{3.1}$$

where $\mathcal{H}$ is a general evolution super-operator. We explicit the dependency of $\mathcal{H}$ by a vector of arbitrary dimension $\Gamma(t)$ called *control field* which contains the experimental parameter that can be tuned in time (we omit the vector notation to avoid heavy equations).

Given a particular control field $\Gamma(t)$, we let the system evolve for a time T to the state described by $\rho(\mathrm{T})$, and, according to our needs, we define a success score of Γ by means of a *cost functional* $\mathcal{J}(\rho, \Gamma)$. Generally $\mathcal{J}$ may contain many terms that reflect different aspects of the evolution (although the form of some fundamental terms depends by the optimization algorithm in use), so it can be written as

$$\mathcal{J}(\rho, \Gamma) = \sum_i f_i(\rho, \Gamma). \tag{3.2}$$

In the simplest case, we can score Γ only by the mismatch between the target density matrix ρ_{trg} and $\rho(T)$, for example by using a trace distance, i.e. $f_1(\rho(T), \rho_{trg}) = \mathrm{Tr}\left[(\rho(T), \rho_{trg})^2\right]$. If we have also experimental or evolution's constraints, we can properly include them in $\mathcal{J}$. For example, if the parameters are limited in amplitude or power, we introduce a term like $f_2 = \int_0^T \|\Gamma(t)\|^2 dt$, or if we want to avoid part of the Hilbert space during the evolution, we can add a term like $f_3 = \int_0^T \|P_{\mathcal{S}}\rho(t)P_{\mathcal{S}}\|dt$, where $P_{\mathcal{S}}$ is a projection operator in the subspace we want to avoid.

Whatever are our goals and constraints, the optimization problem lies in finding the time development of the experimental parameters $\Gamma(t)$ which minimizes the cost function $\mathcal{J}(\rho, \Gamma)$. It doesn't exist a general analytical solution for this problem, so different approaches has been developed for particular cases [70]. In most of the situation one has to opt for a numerical algorithm, which can be implemented with a complexity closely related to the particular system of interest. For our optimization we used one of this numerical approaches, called "Chopped RAndom Bases", or *CRAB* [64].

CRAB

As many optimization algorithms CRAB is an iterative optimizer. Exploiting the whole knowledge of the system that we have, we initially fix the starting behaviour of the experimental parameters forming the control field, writing it as $\Gamma_0(t)$, then the algorithm searches for the best correction of the form $\Gamma(t) = \Gamma_0(t) \cdot g(t)$ which minimizes the cost function $\mathcal{J}(\rho, \Gamma)$. It repeats this

search a variable number of times, until $\mathcal{J}$ decreases below a certain threshold. In the particular case of CRAB the correction function $g(t)$ is expanded using a finite, or "chopped", base $\{\hat{g}_l(t,\Omega_l)\}_{l=0\ldots N}$ whose elements depends by the set of parameter $\{\Omega_l\}_{l=0\ldots N}$. Note that in principle every base is equally appropriate, for example one can simply use $\hat{g}_l(t,\Omega_l) = e^{i\Omega_l t}$. The randomicity enters in basis by the parameters Ω_l, which are updated at each run of the algorithm $\Omega_l \to \Omega_l^k = \Omega_l(1 + r_l^k)$, where r_l^k are random numbers. Note that this randomly chosen basis element may not be orthogonal. Moreover, also the interval of randomicity of r_l^k, as much as the initial choice of the parameter Ω_l^k, often derives from the knowledge of the system properties.

In the end, the cost function is remapped as $\mathcal{J}(\rho, \{a_l^k\})$, and the optimization problem in the search of the set of coefficients $\{a_l^k\}$ that minimizes $\mathcal{J}$, given the random bases $\{\hat{g}_l(t,\Omega_l^k)\}$. The optimization of the coefficients can be performed by using any desired method (in particular we use the *subplex*, a variant of the Nelder–Mead direct search method), and after a given number of iteration we keep the best result has our solution.

3.3 Model Hamiltonian

In order to apply the optimal control theory to our system, we need to identify the set of parameter that can be tuned during the evolution, i.e. the entries of the control field $\Gamma(t)$.

For a direct experimental application of the optimization protocol, we restrict our attention to the ground-state hyperfine level $F = 2$, which is described, in presence of an uniform magnetic field B and a radio-frequency driving potential $V = \Omega/2\cos(\omega_{RF}t)$, by the Hamiltonian H in Eq. 1.14. This Hamiltonian determines the dynamics of the atoms by the Eq. 1.16, which is a set of differential equations unequivocally identified by the parameters $\Gamma = \{\mathrm{B}, \omega_{RF}, \Omega\}$. We can thus implement the optimization protocol by controlling this three quantities, or a subset, obviously taking into account our ability to manipulate them individually. In particular:

- The magnetic field B is produced by external coils. We can carefully control its value in the range $\mathrm{B} = 0.2 \div 15\ \mathrm{Gauss}$ along the three principal directions, but the time scale of the control is of the order of hundreds of μs if we want to avoid inductive reactions by the coils.

- The RF driving potential is the near field radiated by a U-shaped wire on the chip which we call “antenna” (see section 1.2.1). The signal applied to the antenna is produced by a function generator which has arbitrary waveform production capability at a maximum sampling rate of $250\ \mathrm{MSa/s}$ (Agilent 33522B). It follows that:

- The Rabi frequency Ω depends on the amplitude of the signal applied to the chip's antenna (see section 1.4.3), and on the alignment between the quantization axis (imposed by the external magnetic field), and the RF field polarization on the atoms. Its maximum value in the actual experimental setup is $\Omega \sim 100\,\mathrm{kHz}$. Since the impedance of the antenna on the chip has a low reactive part in the frequency range of interest, we are able to control Ω in a sub-μs time-scale.
- The radio-frequency $\nu_{RF} = \omega_{RF}/2\pi$ can be modulated arbitrarily in a range of several hundreds of kHz around the working frequency, without the radiation efficiency of the antenna is substantially affected.

Moreover, we note that B and ω_{RF} enters in H by the diagonal elements $\delta_{m_F}(\mathrm{B}, \omega_{RF}) = \omega_{m_F}(\mathrm{B}) - m_F\,\omega_{RF}$, $\hbar\omega_{m_F}(\mathrm{B})$ being the energy of the m_F ($F = 2$) magnetic sub-level (for a compact notation we omit subscript related to the hyperfine level). Thus, if we neglect the residual splitting coming from the quadratic Zeeman effect, from variations of the magnetic field $\Delta\mathrm{B}$ we can obtain the same effects of opposite sign variations of the radio-frequency $-\Delta\nu_{RF}$, i.e. $\Delta\delta_n = 0 \Leftrightarrow \mu_B g_F\,\Delta\mathrm{B}/\hbar = -2\pi\,\Delta\nu_{RF}$.
Taking account of all this factors, we choose to modulate in time only the radio-frequency $\boldsymbol{\nu_{RF} \rightarrow \nu_{RF}(t)}$, even if other results not shown here demonstrates that we are perfectly able to control simultaneously ν_{RF} and Ω but the improvements in terms of preparation accuracy are not experimentally relevant. The depth of modulation is set to $\Delta\nu_{RF} = 1.3\,\mathrm{MHz}$ around the central frequency ν_0 arbitrarily set to $\nu_0 = 4.323\,\mathrm{MHz}$. For every optimization we will use one constant value of magnetic field and Rabi frequency of the radio-frequency driving, in particular we set $\boldsymbol{\Omega = 2\pi\ 60\ \mathrm{kHz}}$, and $\boldsymbol{\mathrm{B} = 6.1794\ \mathrm{Gauss}}$. Note that the values of ν_0 and B are chosen in order to have resonant coupling between sub-level energy splitting and the radio-frequency driving (except for the residual quadratic detunings $\delta_{\pm 2} = -2\pi\,11.0\,\mathrm{kHz}$, $\delta_{\pm 1} = -2\pi\,2.7\,\mathrm{kHz}$, $\delta_0 = 0$).

3.3.1 Radio-frequency modulation and cost function

To correctly describe the system dynamics in presence of the time modulation of the angular-frequency $\omega_{RF}(t) = 2\pi\,\nu_{RF}(t)$, the Hamiltonian in Eq. 1.14 has to be modified, replacing ω_{RF} with the time derivative of the field phase $f(t) = \partial_t\,(t\,\omega_{RF}(t))$ (see Appendix A for details).
Within the CRAB picture, we decided to expand $f(t)$ in the standard Fourier basis. So we define

$$\begin{aligned} \Gamma(t) &= f(t) = f_0\,\mathrm{Re}\,[g(t)] \\ g(t) &= 1 + \alpha \sum_{l=-n}^{n} a_l\ \exp(i\,2\pi\,\nu_l\,t) \end{aligned} \quad , \tag{3.3}$$

where $\nu_l = l/\mathrm{T}$, T the time duration of the modulation, i.e. the optimal pulse length, n being the number of harmonics set to 7, $\{a_l\}_{l=-7\ldots7}$ a complex vector normalized to one, and α set the amplitude of the frequency modulation. In order to have $\Delta\omega_{RF} = 2\pi\,1.3\,\mathrm{MHz}$ we set $\alpha = 0.15$. Finally $f_0 \equiv 2\pi\,\nu_0 = 2\pi\ 4.323\ \mathrm{MHz}$.

As mentioned in the previous paragraph, the cost function can contain many terms, depending on the features of the evolution in which we are interested. In our case, for a straightforward experimental proof of the optimal pulses output, we have decided to prepare states with defined occupation probabilities. The choice is motivated by the fact that we probe the atoms using a Stern-Gerlach discrimination followed by an absorption imaging sequence, so we can directly measure the population distribution between the Zeeman sub-states of a coherent superposition. This population distribution reflect the probability of occupying the sub-states, but won't tell us anything about relative phases. In other words, when a single particle state is described by a density matrix ρ we can directly measure the diagonal elements ρ_{nn}, but not the coherences ρ_{nm} . What follows is a cost function of this form

$$\mathcal{J} = \frac{1}{2}\sum_n |\rho(\mathrm{T})_{nn} - [\rho_{trg}]_{nn}| \ , \tag{3.4}$$

where $[\rho_{trg}]_{nn}$ are the target relative populations we want to achieve, $\rho(\mathrm{T})_{nn}$ the relative populations at the end of the pulse manipulation, and the sum runs over the non-zero populated target sub–levels. We recall that the initial state of the atomic system is given by all the atoms occupying the $m_F = +2$ sub-level, i.e. $\rho_{1,1}(t=0) = 1$ (see section 1.3).

3.4 State preparation results

To test the applicability of the optimal control algorithm CRAB to our atomic system, we decided to produce and experimentally implement on our BEC several control pulses to create arbitrary internal state super-positions which are either impossible to be achieved when the evolution is driven by constant parameters Hamiltonians, or, eventually, they are encountered only after long evolution time.

3.4.1 Population distribution preparation

We initially focus on the preparation of a series of target states ρ_{trg} characterized by having a defined population distribution among the m_F sub-levels, so as to directly verify the algorithm output in the experiment, as discussed in section 3.3.1. These states are labelled as A, ... , I in Tab. 3.1, where we list them together with their target populations. They cover a wide portion of the Hilbert

TABLE 3.1: Test states prepared, labelled as A, . . . ,I. For each state, in the upper line are reported the target relative populations ρ_{nn}, in the lower line the mean values with errors of the experimentally measured populations. For all the states, the preparation pulse length is set to $100\ \mu s$. Last two columns are the theoretical (ϵ_T) and experimental (ϵ_E) error functions in the state preparation.

State	ρ_{11}	ρ_{22}	ρ_{33}	ρ_{44}	ρ_{55}	$\mathcal{J}_{Th}$	$\mathcal{J}_E$
A	1/2	0	0	0	1/2	0.04	0.07(1)
	0.54(1)	0.01(1)	0.02(1)	0.03(1)	0.40(1)		
B	1/2	0	0	1/2	0	0.06	0.02(1)
	0.47(1)	0.01(1)	0.01(1)	0.50(1)	0.01(1)		
C	0	1/2	0	1/2	0	0.02	0.04(1)
	0.01(1)	0.53(1)	0.02(1)	0.43(1)	0.01(1)		
D	1/2	1/2	0	0	0	0.01	0.02(1)
	0.50(2)	0.47(2)	0.03(1)	0(0)	0(0)		
E	0	1/3	1/3	1/3	0	0.04	0.03(1)
	0.01(1)	0.32(1)	0.34(2)	0.32(2)	0.01(1)		
F	1/5	1/5	1/5	1/5	1/5	0.03	0.03(1)
	0.19(1)	0.2(1)	0.2(1)	0.22(1)	0.19(2)		
G	0	1	0	0	0	0.03	0.04(1)
	0.03(1)	0.92(1)	0.04(1)	0.01(1)	0(0)		
H	0	0	0	1	0	0.02	0.03(1)
	0.01(1)	0.01(1)	0.03(2)	0.93(2)	0.02(1)		
I	0	0	1	0	0	0.07	0.07(1)
	0.02(1)	0.01(1)	0.86(1)	0.09(1)	0.02(1)		

space, i.e. they have varying distances from the initial ρ_0. A measure of the distance between ρ_{trg} and ρ_0 is given by the Bures (or quantum) angle [45], defined as

$$\mathcal{L}^{QF}(\rho_0, \rho_{trg}) = \arccos\left(\sqrt{\mathcal{F}(\rho_0, \rho_{trg})}\right), \tag{3.5}$$

where $\mathcal{F}(\rho_0, \rho_{trg}) = \mathrm{Tr}\sqrt{\rho_0^{1/2}\,\rho_T\,\rho_0^{1/2}}$ is the Uhlmann fidelity. The Bures angle correspond to a geodesic arch in the Hilbert space between the initial and the final states, and for the super-positions associated to the populations in Tab. 3.1 it ranges from $\mathcal{L}^{QF} = \pi/2$ (orthogonal super-position), to $\mathcal{L}^{QF} = 0.18\,\pi$.

We initially set the evolution time $\mathbf{T = 100\ \mu s}$ for all the states A,. . .,I. Generally, to choose an evolution time one as to consider a series of inherent limitations which impose some bounds on the feasible range of choice, and affect the ability to control a system dynamics. In our case, for example, a constraint is given by the fixed structure of the Hamiltonian, which restrict the number of admissible path in the Hilbert space. This problem is also connected to the Quantum Speed Limit, or QSL, arising from the fact that the physical available resources are finite (in our case the Rabi frequency strength and the range of

radio-frequency modulation, as explained in section 3.3), therefore is impossible to evolve at an arbitrary high speed in the Hilbert space. Finally, one has to face with the unavoidable decoherence sources, and with the instabilities of the experimental parameter, limiting the maximum exploitable evolution time. In practice, all these limits imply to find trade-off condition between the final experimental error in the state preparation, and the minimal evolution time to get in close proximity of the target state. Our initial choice has been taken considering the typical dephasing rates affecting our experiment (between $100\,\mathrm{Hz}$ and $250\,\mathrm{Hz}$), and the maximum Rabi frequencies attainable with our supply.

Once that all the constraints are included in the theoretical model, for every admissible population distribution, the algorithm produces an optimized radio-frequency modulation $\omega_{RF}(t)$ by minimizing the cost function $\mathcal{J}$ given by Eq. 3.4. We define the value of $\mathcal{J}$ resulting from the optimization *theoretical state preparation error*, and we write it as $\mathcal{J}_{Th}$. In Tab. 3.1 we report the values of $\mathcal{J}_{Th}$ resulting from the optimization when we include in the model an effective dephasing rate $\gamma = 2\pi\,200\,\mathrm{Hz}$.

Each theoretical pulse is finally translated in the frequency modulated voltage signal to apply at the chip antenna for the manipulation of the atoms. By means of the procedure detailed in section 1.4.3, the signal amplitude was set to produce the prefixed Rabi coupling $\Omega = 2\pi\ 60\ \mathrm{kHz}$.

The experimental tests were performed as in the following. We start with the BEC in the initial pure state $|m_F = +2\rangle$, magnetically trapped by the chip. By turning off the trap we let the atoms free-fall and expand in the homogeneous field created with the external Helmholtz coils, set, in the limit of the experimental uncertainty, to the chosen value $B = 6.1794\,\mathrm{Gauss}$ (see section 1.4.3). After $700\,\mu\mathrm{s}$ of free expansion we apply the manipulation signal to the chip, and, after further $5\,\mathrm{ms}$, we turn on the inhomogeneous magnetic field for the Stern-Gerlach deflection for a total time of $10\,\mathrm{ms}$, after that we record the five clouds profiles with the absorption imaging sequence, obtaining the relative populations $p_{m_F}(\mathrm{T})$ in each m_F sub-level. As already done for the theoretical preparation, we can define an *experimental state preparation error* $\mathcal{J}_E$, substituting $p_{m_F}(\mathrm{T})$ to $\rho(\mathrm{T})_{nn}$ in Eq. 3.4. For every state we repeat ten times the preparation procedure under the same experimental condition, and the $\mathcal{J}_E$ and population distributions reported in Tab. 3.1 are the corresponding mean values and standard deviations of the results. Note the excellent agreement between experimental data and theoretical predictions.

3.4.2 Coherence preparation

To show that we are also able to produce the coherence terms between the m_F sub-states, and not only defined population distributions, we prepared the higher and lower energies eigenstates of the Hamiltonian $\widetilde{H}$ which results from

applying to the atoms a resonant radio-frequency driving under the same constraints for the magnetic field and Rabi frequency used in the preparation phase, i.e. $\mathrm{B} = 6.1794\,\mathrm{Gauss}$, $\Omega = 2\pi\,60\,\mathrm{kHz}$, and $\omega_{RF} = 2\pi\,4.323\,\mathrm{MHz}$. We recall that, as shown in section 1.4.3, in presence of such driving the atoms coherently oscillates between all the sub-levels, unless the initial state from were the oscillations would start is an eigenstate of $\widetilde{H}$. Unlike previously done, for this preparations we used a manipulation time $\mathrm{T} = 20\,\mu\mathrm{s}$. The cost function to use in this case has to take account of the coherences, so we used the infidelity function given by

$$\mathcal{J} = 1 - F(\rho(T), \rho_{trg}), \tag{3.6}$$

and, using as additional constraint in the optimization algorithm, we forced the final value of the optimal pulse radio-frequency to be $\omega_{RF}(T) = 2\pi\,4.323\,\mathrm{MHz}$.

Also in this case we followed the same experimental sequence outlined above, and, to check if the preparation was successfully, we observed the absence of any oscillations by driving the atoms with the resonant radio-frequency field immediately after the optimal pulse manipulation. In Fig. 3.1 we show the five relative population behaviour during the preparation, and during the subsequent presence of the resonant driving.

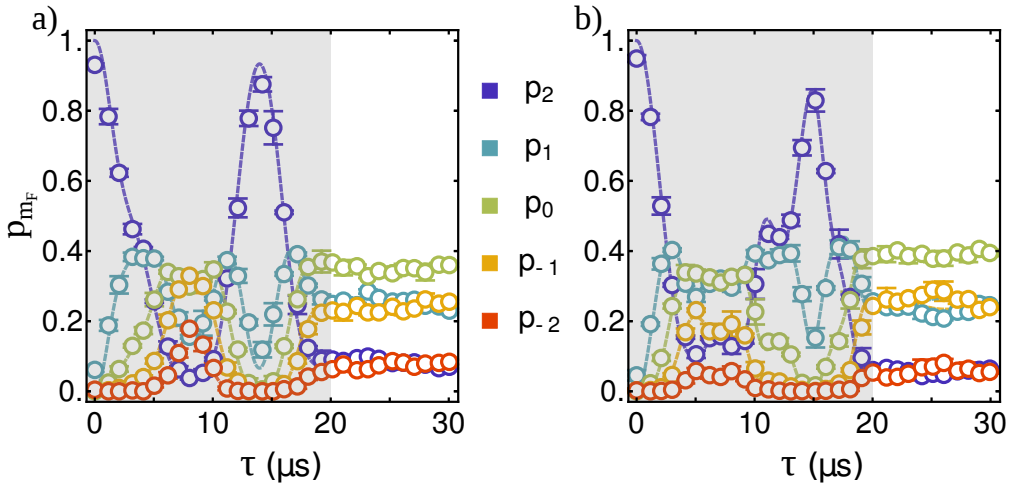

FIGURE 3.1: Preparation of the lower (right side) and higher (right side) eigenstates of the Hamiltonian $\widetilde{H}$ describing a resonant radio-frequency coupling at $\Omega = 2\pi\,60\,\mathrm{kHz}$, and $\omega_{RF} = 2\pi\,4.323\,\mathrm{MHz}$ ($B = 6.1794\,\mathrm{Gauss}$). The grey area shows the population behaviour of the five sub-levels during the preparation phase, which follows (white area) the radio-frequency driving corresponding to $\widetilde{H}$. We report both theory (lines) and experimental measurements (dots). Each set of five measured populations represents the mean values and standard deviation calculated from the outcome of seven different realizations under the same experimental conditions.

Of course the absence of evolution can happen only if the relative phases of

all sub-levels are correctly realized, proving the full capability of our optimal preparation scheme.

3.4.3 State tomography

We shown above the results about the preparation of states having a defined population distribution among the m_F sub-levels, and those about the preparation of two eigenstate of the Hamiltonian related to a resonant constant radio-frequency driving. In the first case, we used the simple cost function form given in Eq. 3.4. Note that the coherence terms are not involved in this equation, so they can assume any allowed value at the end of an optimized preparation. Nonetheless their correct evolution respect to the theoretical prediction is crucial to obtain the expected results. For this reason, given the satisfactory match between measured and expected population distribution, we can be confident that also the final coherences are close to what the theory provides. However, we can quantitatively assess their preparation by using the state reconstruction scheme described in chapter 2.

We focus on the state labelled as A in Tab. 3.1, having a 50% population distribution between the $m_F = \pm 2$ sub-levels.

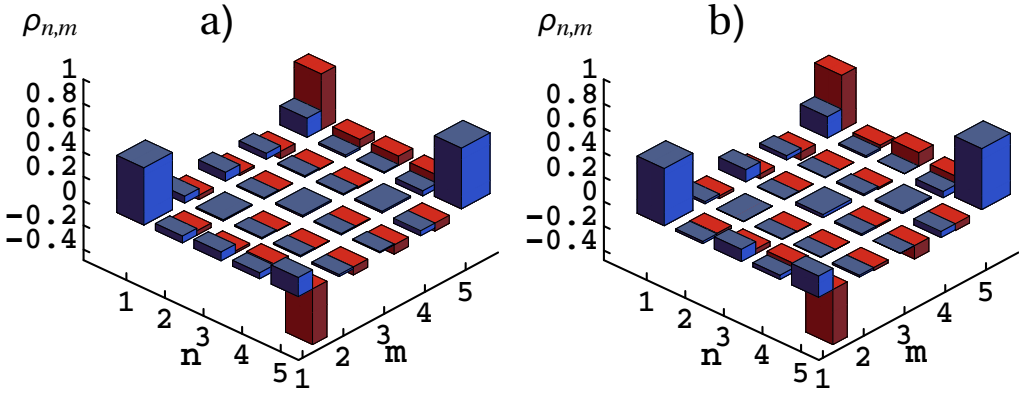

FIGURE 3.2: Representation of the reconstructed density matrix ρ_{exp} (a) and theoretically expected one $\rho(T)$ (b), related to the state A. We show in blue (red) the real (imaginary) components. The Uhlmann fidelity between $\rho(T)$ and ρ_{exp} in is $\mathcal{F} = 0.93$.

For the reconstruction we used a tomography pulse having the same amplitude of the preparation pulse ($\Omega = 2\pi\, 60\,\mathrm{kHz}$), resonant with the sub-levels splitting ($\omega_{RF} = 2\pi\, 4.323\,\mathrm{MHz}$), and directly following the preparation phase, without any intermediate delay. By measuring the population evolution in a time window $10.4\,\mu\mathrm{s}$ long, each $\tau = 10\pi\,/\omega_{RF} \simeq 1.15\,\mu\mathrm{s}$, we obtain an estimate of the experimental density matrix ρ_{exp}, shown in the left side of Fig. 3.2. We

evaluate the overlap between ρ_{exp} and $\rho(\mathrm{T})$ (right side of Fig. 3.2) calculating the Uhlmann fidelity, which turn out to be a satisfactory $F = 0.93$.

In figure 3.3 we also show the theoretical (lines) and experimental (dots) dynamical evolution of the atomic populations in the two sub–levels $m_F = \pm 2$ together with the calculated values of $\mathcal{J}$ during the application of the $100\,\mu$s long preparation pulse. Also in this case, the almost perfect correspondence between theory and experiment shows that the relative phases of the sub–levels are well under control at any time during the evolution.

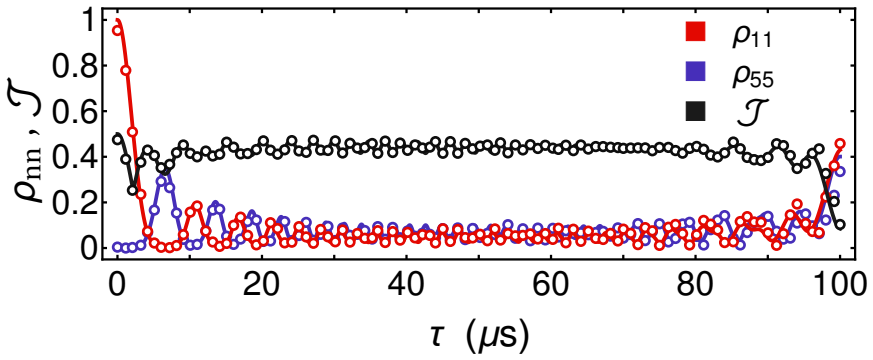

FIGURE 3.3: Theoretical (lines) and experimental (dots) dynamical evolution of the population of the sub–levels $m_F = +2$ (red) and $m_F = -2$ (blue), and of the calculated cost function $\mathcal{J}$ (black) during the application of the $100\ \mu$s long optimal pulse which produces the state A. To better reproduce the experimental points, the theoretical evolution includes a dephasing rate of 200 Hz and a magnetic field mismatch with respect to the theoretical value $6.1794\,\mathrm{Gauss}$, caused by long term drifts. In the data reported in Table 3.1 the output of the preparation pulse is recorded right after the magnetic field calibration, making those results less affected by such fluctuations.

Finally, we note that the Hamiltonian $\widetilde{H}$ of which we produced the eigenstates is identified by the same experimental parameter describing the tomography manipulation, so the data recorded in the time window $10\,\mu$s long after the states production (see Fig. 3.1) can be used to reconstruct the output density matrices. The estimated and expect results are shown in Fig. 3.4, and in both the cases we satisfactorily obtained fidelities $F > 0.99$.

3.4.4 Speed limit

We faithfully achieved the population distribution A,. . ., I using optimal pulses of duration $\mathrm{T} = 100\,\mu$s. Then a natural question arise: how much we can shorten T maintaining low errors in the state preparation? As explained above, the answer depend both on the finite amount of the resources used to drive the system, which imply a limit in the reaction time (the Quantum Speed Limit),

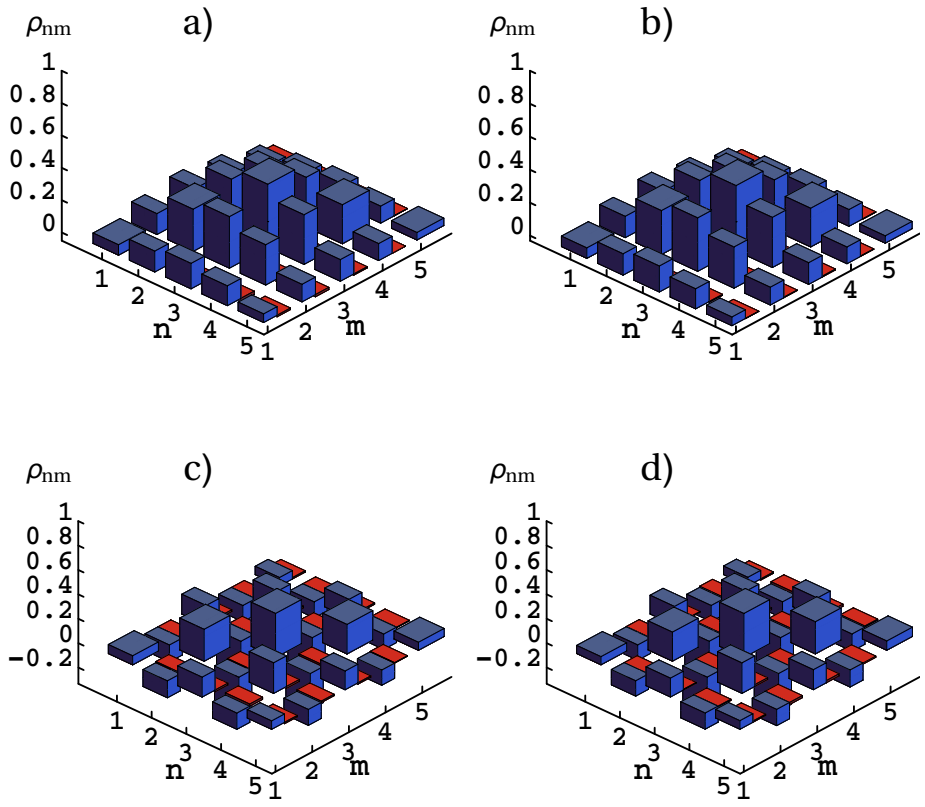

FIGURE 3.4: Pictorial representation of the reconstructed density matrix ρ_{exp} (left side) and theoretical expected one $\rho(T)$ (right side), associated to the lower (a,b) and higher (c,d) energy eigenstate of the constant frequency radio-frequency driven Hamiltonian $\widetilde{H}$. The real (imaginary) part of the matrices is represented in blue (red). The Uhlmann fidelity is $\mathcal{F} = 0.99$ for both the reconstructions.

and on the allowed paths in the Hilbert space, which depend on the specific Hamiltonian form. Especially this last factor makes difficult to derive a general theoretical bound, so it is necessary a direct analysis of the behaviour of the experimental and theoretical preparation errors as a function of T.

We again concentrate on the state A, fixing different pulse lengths and minimizing the cost function under the same constraint of constant magnetic field and Rabi frequency mentioned above. In Fig. 3.5 we show the results of the optimization. It can be noted that the theoretical noiseless errors $\mathcal{J}_{Th}$ saturate to a minimum when $\mathrm{T} \gtrsim 80\,\mu\mathrm{s}$, while for shorter time it can be observed a linear trend of increasing errors with decreasing pulse length. The experimental results $\mathcal{J}_E$ are perfectly matched to the noiseless expected values at short pulse times while deviate for longer pulses, mainly because of the increasing

effect of the dephasing rate γ on the evolution, and because of the uncertainties in the experimental parameters. For example the same γ is not constant from an experimental cycle to the next. It originates from the collisions with the background-gas atoms, and from a residual density dependent energy shift in the BEC. Since our BEC has atom-number fluctuations of the order of 15%, then γ carries in the effects of this fluctuations, leading to an unstable result of the pulse output. Another source of output instability are the low frequency fluctuations of the magnetic field, which do not average out in the time scale of tenth of μs of our pulses, so they do not simply contribute to increase the dephasing rate. We estimates that in our set-up the shot to shot fluctuation on a 1-hour time-scale are of the order of $\Delta B = 5\,\mathrm{mGauss}$. If we include in the simulation all this effects to correct the noiseless theoretical predictions, we obtain an area of uncertainty (shown as a shaded region in Fig. 3.5) which include all the experimental observation.

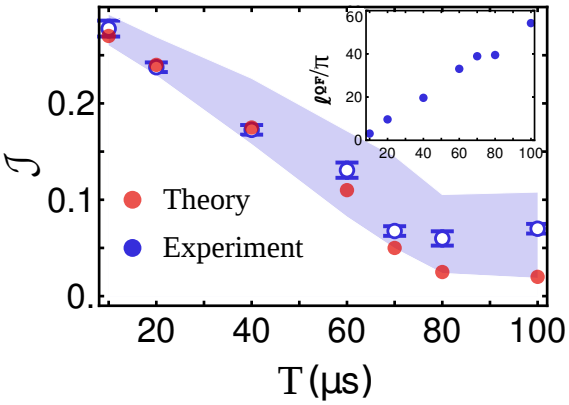

FIGURE 3.5: Error $\mathcal{J}$ in the preparation of state A as a function of pulse length T, obtained theoretically (red dots), in the absence of dephasing noise, and experimentally (blue dots). The effect of dephasing noise in the range $2\pi\,[0, 200]$ Hz, and of long term magnetic field fluctuations in the range of $\Delta B = 5\,\mathrm{mGauss}$, is also considered (blue shaded region). Inset: Bures length l^{QF} calculated for every optimal pulse as a function of T.

In terms of Bures angle (see Eq. 3.5) the geodesic arch between the initial state of the BEC ($|m_F = +2\rangle$) and the state A is $\mathcal{L}^{QF} = \pi/4$. This is the arch that the system would follow in the case of a direct resonant coupling between the sub-levels $|m_F = +2\rangle$ and $|m_F = -2\rangle$, a coupling that of course does not exist. The lack of couplings between all the sub-levels imply the underestimation of the Quantum Speed Limit bound, which imposes that $\mathcal{L}^{QF}(\rho_o, \rho_{trg}) \leq \ell^{QF}(\rho_0, \rho_T)$, where ℓ^{QF} is the length of the path covered during the optimal evolution, and it can be calculated using the formula

$$\ell^{QF}(\rho_0, \rho_T) = \frac{1}{\hbar}\int_0^T dt\sqrt{\langle H(t)^2\rangle - \langle H(t)\rangle^2}. \tag{3.7}$$

In the inset of Fig. 3.5 we show for each pulse the calculated values of ℓ^{QF}. They range from $\ell^{QF} = 49\,\pi$ in the case of pulse length $\mathrm{T} = 100\,\mu\mathrm{s}$, to $\ell^{QF} = 2.48\,\pi$ when $\mathrm{T} = 10\,\mu\mathrm{s}$, well above the QSL limit bound for the reason given above.

3.5 Conclusions and outlook

In conclusion, in this experiment we have applied an optimal control tool to prepare a family of different internal states super-positions of a Rubidium Bose-Einstein condensate produced in an atom chip-based micro-trap. We theoretically and experimentally find that these states can be prepared with a very small error in the final population distribution with respect to the desired states, and we show, by a tomographic reconstruction, that the whole density matrices are obtained according to the theoretical prediction with fidelities above $F \geq 0.9$. We have observed the behaviour of the state preparation error $\mathcal{J}$ by varying the (control) pulses length, showing the limit of a fast manipulation of the atomic state. In this respect a deeper analysis of the results may put in a different light the meaning of the quantum speed limit for this complex dynamics.

All these results might pave the way for new schemes towards, among others, better control of quantum dynamics, preparation of squeezed states, time-inversion of the system dynamics, realization of quantum gates, and more powerful quantum information protocols.

Chapter 4

Quantum Zeno dynamics

In the previous chapters we always considered internal states superpositions involving the full hyperfine manifold $F = 2$, demonstrating how it is possible to fully characterize them, and how to achieve an arbitrary manipulation. However, for some particular applications, it is often necessary to confine the dynamics in a determined number of sub-levels. In quantum information processing, for example, couples of quantum states are used to represent qubits. By properly engineered interactions it is possible to connect only the selected states, isolating the dynamics between them, but to tasks of increasing complexity correspond equally complicated setups, which place limits to the actual feasibility of some manipulations.

Thus, in order to be able to perform complex quantum logical operations, the ability to dynamically tailor the sub-spaces interested by the coherent evolution is of fundamental importance. It turns out that this task is actually possible, by exploiting the back action of quantum measurements and strong perturbations to disconnect different groups of sub-states, binding the evolution in smaller portions of the full space. This phenomenon is known as "quantum Zeno dynamics".

In this chapter I report on the first experimental realization of Zeno dynamics inside a two-level subregion of the hyperfine level $F = 2$, showing in particular, how different perturbations of the system lead to the same confining effect. The first section is devoted to a theoretical introduction which starts from the first formulation of a quantum Zeno "paradox", to arrive at the nowadays accepted quantum Zeno dynamics. Then I will discuss how it is possible to experimentally implement the necessary manipulations tools in our apparatus, and finally I will present and analyse the experimental results.

The content of this chapter is an extended version of ref. [71].

4.1 From quantum Zeno effect to quantum Zeno dynamics

"A flying arrow never reaches the target" is one of the controversial arguments against plurality and motion devised by the Greek philosopher Zeno of Elea[1]. Regardless of the reasons for which it has been formulated, this paradox has inspired for over two millennia philosophers until it has been solved by mathematicians with modern calculus. Quantum physicists reinvented it, not as a logical paradox, but as a real physical effect, the quantum Zeno effect (QZE).

In its original formulation, the QZE was based on the less intuitive and most debated postulate of the quantum mechanics, i.e. the von Neumann projection postulate [72]. It states, in contrast to classical mechanics, that any physical measurement will perturb a quantum state leaving it in an eigenstate of the hermitian operator representing the quantity to be measured, or, as usually expressed, it is impossible to probe a quantum system without disturbing it. Von Neumann already noted that a given quantum state can be guided into any other state by tailoring a specific sequence of measurements. Conversely, in the case of frequently enough identical observation, the back action of the measurement process leads to freezing out the dynamics: a prominent example of measurement-induced disturbance that later gave the name to the QZE [73].

The QZE was first qualitatively proven in a system of trapped $^{9}Be^{+}$ ions [74], in which Rabi-driven oscillations between two hyperfine levels were significantly slowed down by pulsed optical pumping to a third level. A quantitative assessment of the phenomenon by means of a similar scheme, but using a ^{87}Rb BEC, was given in ref. [75]. In open systems, the Zeno effect as well as an acceleration due to an anti-Zeno effect [76, 77] were first demonstrated in ref. [78], were cold neutral sodium atoms were trapped in an accelerated optical lattice. For a large acceleration the atoms can tunnel in unbound states but by repeatedly measuring the surviving population the depletion rate of the trap can be considerably enhanced or slowed down, depending by the observation frequency. Both the Zeno and anti-Zeno effects can also influence thermalization [79].

A general approach for the control of quantum behaviour by coupling to the continuum was presented in ref. [77]. Beside the evidence of the QZE in more and more physical systems, today this is a well-established effect used as a practical tool, for example in quantum information processing [80, 81], or, in connection to other research fields, for fundamental physics investigation, like the theory of large deviations [82], or of disordered systems [83].

However, QZE is only a particular case of a much more complex phenomenology, which does not necessarily imply the slowdown of the dynamics, and for

[1] https://en.wikipedia.org/wiki/Zeno's_paradoxes

which projective measurements are not mandatory ingredients. Indeed, the current point of view, widely accepted, identify in the dephasing between different regions of the Hilbert space of a principal quantum system, induced by strong interactions with a secondary one, the origin of a new coherent dynamics which can eventually develop independently in these regions. This resulting phenomenon, known as quantum Zeno dynamics (QZD), has been clearly highlighted in ref. [84].

In the next sections I will briefly introduce the working principle of the QZD starting from its first manifestation, i.e. the QZE. Then I will show how the QZD arises from three different perturbations of a quantum system. The main argumentation will follow the description given in ref. [85].

4.1.1 Quantum Zeno effect

The QZE consists in the suppression of the decay probability of an unstable quantum system when frequently observed. However, most of the experimental realizations have focused on the inhibition of the transition rate in externally driven two level systems.

By applying to an ensemble of N atoms for a time τ a driving field almost resonant with the levels $|0\rangle$ and $|1\rangle$, and neglecting any dephasing or depletion of the atomic population, we observe coherent Rabi oscillations described by

$$\begin{aligned} N_0(t) &= N\left(\frac{\Omega_R}{\Omega}\right)^2 \cos^2\left(\Omega\, t/2\right)\,, \\ N_1(t) &= N - N_0(t)\,, \end{aligned} \tag{4.1}$$

where $N_i(\tau)$ is the population of the $|i\rangle$ level, and $\Omega = \sqrt{\Omega_R^2 + \delta^2}$ the generalized Rabi frequency. An example of such system, represented in Fig. 4.1, consists in a ^{87}Rb BEC subjected to a two photon driving which couples the hyperfine levels $|1,0\rangle \leftrightarrow |2,0\rangle$. In right side of Fig. 4.1 we show an example of Rabi oscillations starting from $N_0(t=0) = N$.

We recall from section 1.4.2, that the relative populations $n_i(\tau) \equiv N_i(\tau)/N$ closely approximate the probabilities $p_i(\tau)$ to detect a single atom in the i-level after an evolution time τ. In particular $p_0(t)$ is defined as *survival*, or *nondecay* probability. In the resonant case ($\delta = 0$), after half oscillation period $\tau_\pi = \pi/\Omega_R$, the whole population is transferred in the state $|1\rangle$, and the survival probability is 0.

Suppose that we are able, during the resonant oscillations, to perfectly and instantaneously measure the number of atoms $N_0(\delta\tau)$. The related observable can be represented by the projector operator $P = |0\rangle\langle 0|$, which will project the state of the atoms on the level $|0\rangle$. As a consequence of the projective measurement the atomic population on level $|1\rangle$ will be lost, and the remaining

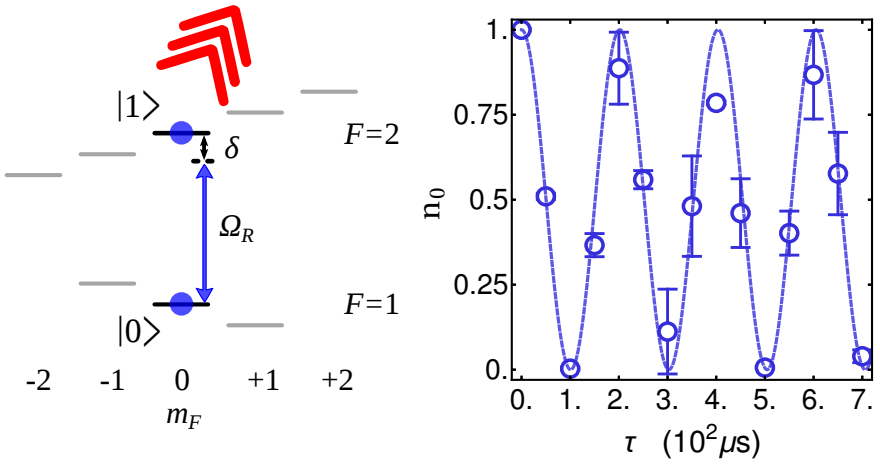

FIGURE 4.1: Left side: Pictorial scheme representing the experimental realization of the quantum Zeno effect. A laser induced Raman transition, δ detuned from the resonance, couples the sub-levels $|0\rangle \equiv |1,0\rangle$ and $|1\rangle \equiv |2,0\rangle$, while a laser resonant with the transition $|F=2\rangle \rightarrow |F'=3\rangle$ (red arrows in the picture) deplete the population of the former, and, if strong enough, results equivalent to a projective measurement. Right side: typical Rabi oscillations of the population n_0 on the level $|0\rangle$, as a function of the Raman pulse length. The dashed line represent a fit of the data with the model equations 4.1, which yields $\Omega \simeq 2\pi\, 5\,\mathrm{kHz}$, and $\delta \simeq 0$.

population, i.e.

$$N_0(\delta\tau) = N\cos\left(\Omega_R\delta\tau/2\right)\,, \tag{4.2}$$

will start afresh to oscillates as it would have been $t = 0$. If we repeat the measurement process of the N_0 population m times during the normal Rabi oscillation, at constant times $\delta\tau$, at the time $T = m\,\delta\tau$ the surviving population in $|0\rangle$ will be given by

$$\begin{aligned} N_0(m\,\delta\tau) &= N\underbrace{\cos\left(\Omega_R\delta\tau/2\right)\cdot\ldots\cdot\cos\left(\Omega_R\delta\tau/2\right)}_{m\text{ times}} \\ &= N\left(\cos\left(\Omega_R\delta\tau/2\right)\right)^m\,. \end{aligned} \tag{4.3}$$

When the evolution time $\delta\tau$ between the measurements is such that $\delta\tau\,\Omega_R \ll 1$, the cosine in Eq. 4.3 can be approximated by $\cos\left(\Omega_R\delta\tau/2\right) \approx (1-(\Omega_R\delta\tau/2)^2)$. Substituting $\delta\tau = T/m$, and assuming the equivalence between the survival probability $p_0^{(m)}(T)$ and the surviving relative population $n_0^{(m)}(T) = N_0(T)/N$, we obtain

$$p_0^{(m)}(T) \approx \left(1-(\Omega_R T/2\,m)^2\right)^m \overset{m\,\text{large}}{\sim} e^{-\Omega_R^2T^2/2m}\,. \tag{4.4}$$

We, therefore, define the "Zeno time" $\tau_z^2 \equiv 2/\Omega_R^2$, which set the natural time scale of the system evolution.

From the last similarity in the above equation it is clear that whenever the condition $T^2/m\tau_z^2 \ll 1$ is satisfied, then the survival probability is maximized, $p_0^{(m)}(T) \to 1$, i.e. the oscillations *freeze* and the atoms never leave the level $|0\rangle$. The condition $T^2/m\tau_z^2 \ll 1$ can hold in different cases, for example when T is constant and the number of measurement m increases, or when m is constant but T decreases (both the situations imply a decreasing $\delta\tau$). As an example, in Fig. 4.2 we show the surviving relative population in the $|1,0\rangle$ sub-level, after $m = 100$ measurements performed during Rabi oscillations between this level and the $|2,0\rangle$, as a function of the evolution time $\delta\tau$.

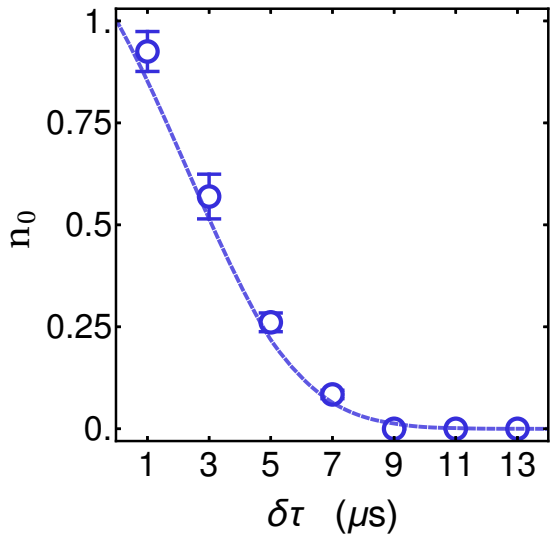

FIGURE 4.2: Typical exponential decay of the survival probability of the atoms on the $|0\rangle$ sub-level as a function of the time interval $\delta\tau$ between the resonant light pulses. In particular, while the Raman coupling is on ($\Omega \simeq 2\pi\,5\,\mathrm{kHz}$, $\delta \simeq 0$), we pulse 100 times the resonant light, and then we measure the population surviving on $|0\rangle$ level. The dashed line represent the theoretical behaviour of the survival probability, as modelled in Ref. [83].

For each $\delta\tau$ the system is driven at a Rabi frequency of $\Omega_R \simeq 2\pi\,5\,\mathrm{kHz}$, and the measurements on the atoms in $|1,0\rangle$ are achieved indirectly, by means of $1\,\mu\mathrm{s}$ long pulses of resonant light with the transition $|F=2\rangle \to |F'=3\rangle$. These pulses scatters out from the condensate the atoms on the level $|2,0\rangle$, accomplishing their effective measurement. The unscattered atoms undergo a negative-measurement process, given that their wave function is still projected on the unperturbed sub-state $|1,0\rangle$, even if we did not extracted any physical quantity from them.

Other experimental realizations demonstrated also the continuous QZE, i.e. a suppression of the dynamics in presence of a continuous strong coupling, mimicking the limit of infinite number of measurement, $m \to \infty$ [75].

The measurements considered here, probing the atoms on one level, are represented by 1-dimensional projections. In this case any evolution could only result in blocking the dynamics, but let us now linger on this point. What would happen if the levels involved in the dynamics are more than two? And what if the measurements affect more than one sub-level simultaneously? Moreover, the projective measurements correspond to ideal, instantaneous observations of the system state, and we can use them only as convenient, and rough, approximation of a more complex process which often involves more elementary steps, which can still be described in terms of (usually dissipative) dynamical evolutions. This facts could raise doubts about the real link between the QZE and the "measurement process" in a wide sense, as we will see in the next section.

4.1.2 Quantum Zeno dynamics

It turns out that the QZE is only the 1-dimensional manifestation of a richer phenomenon, the dynamical quantum Zeno effect, which hinges on measurements not able to distinguish between states belonging to a wider space, giving the same results when performed on them. Rather than slowed down, the dynamics results confined by this "incomplete" measurements in the multi-dimensional subspace of indistinguishability, leading to the QZD. Moreover, as mentioned above, the QZD does not necessarily require the use of projections to be established, but rather of strong perturbative couplings which can be part of a measurement process.

We will consider in the following three different coupling protocols leading, in some limit, to the QZD. The first protocol consists in the extension of the projective measurements to the multi-dimensional case. Then we will treat the cases of frequently enough unitary kicks, and of a continuous strong coupling.

QZD induced by projective measurements

An ideal, instantaneous (thus non-physical), measurement which gives the same results for different quantum states may be represented by a projection on a multi-dimensional Hilbert space.

Consider a system described by the Hamiltonian H, which support is the d dimensional Hilbert space $\mathcal{H}$. We adopt the density matrix formalism, thus the unitary evolution, starting from ρ_0, is given by

$$\rho(t) = U(t)\rho_0 U^\dagger(t)\,, \tag{4.5}$$

where $U(t) = \exp\{-iHt\}$ (hereafter we use the convention $\hbar = 1$). Suppose we are able to measure the presence of the system in a subspace $\mathcal{H}_P \subseteq \mathcal{H}$ through

the projection operator P ($\mathcal{H}_{\mathcal{P}} = P\mathcal{H}$). This means that for each density matrix ρ representing a state in $\mathcal{H}_P$, the measurement of P gives the same positive result, i.e. $P\rho P = \rho$, or $\mathrm{Tr}[P\rho] = 1$. Let also choose the initial state represented by ρ_0 belonging to $\mathcal{H}_P$.

We want to study the effect of repeated measurement of P during the dynamical evolution of $\rho(t)$ in $\mathcal{H}$. Following the same discussion of previous section, after letting evolve the system for a time $\delta\tau$, we perform the measurement of P. The state at the time of the measurement is represented by

$$\rho(\delta\tau) = P\,\Big(U(\delta\tau)\rho_0 U^\dagger(\delta\tau)\Big)\,P\,, \tag{4.6}$$

and the probability to remain in $\mathcal{H}_P$ is given by

$$p(\delta\tau) = \mathrm{Tr}\left[P\,U(\delta\tau)\rho_0 U^\dagger(\delta\tau)\right]\,. \tag{4.7}$$

The projected state in Eq. 4.6 continues to evolve for $\delta\tau$ and then we measure it again, and the same procedure is identically repeated on the resulting state, obtaining, after m repetitions, the final result

$$\rho(m\,\delta\tau) = \underbrace{PU(\delta\tau)\cdot\ldots PU(\delta\tau)}_{m\text{ times}}\,\rho_0\,\underbrace{U^\dagger(\delta\tau)P\cdot\ldots U^\dagger(\delta\tau)P}_{m\text{ times}}\,. \tag{4.8}$$

We can recast Eq. 4.8 by making use of the projection property $P^2 = P$ (and thus $PU\,PUP = PUP\,PUP$), and of the fact that ρ_0 belong to $\mathcal{H}_P$ ($P\rho_0 P = \rho_0$). Then, introducing $T = m\,\delta\tau$, we obtain

$$\rho(T) = \mathcal{V}_m(T)\rho_0\mathcal{V}_m^\dagger(T)\,, \tag{4.9}$$

where we have defined the operator

$$\mathcal{V}_m(T) \equiv [PU(T/m)P]^m\,, \tag{4.10}$$

which accounts all the m evolutions and measurements. The probability to found the system in $\mathcal{H}_P$ is finally given by

$$p(T) = \mathrm{Tr}\left[\mathcal{V}_m(T)\rho_0\mathcal{V}_m^\dagger(T)\right]\,. \tag{4.11}$$

Also in this case the limit of large m set the quantum Zeno regime, but this time one must pay a particular attention in draw conclusions. In Ref. [73] the authors proven that, under very general conditions, the limit $\mathcal{V}_m(T) \xrightarrow{m\to\infty} \mathcal{V}(T)$ exists for all T, and $\mathcal{V}(T)\mathcal{V}^\dagger(T) = P$. We refer to their work for a formal and complete demonstration, while here we follow Ref. [85] in performing a naive expansion

of the evolution operator for small time,

$$U(T/m) \approx (1 - iHT/m) \ , \tag{4.12}$$

which inserted in $\mathcal{V}_m(T)$ yields

$$\begin{aligned} \mathcal{V}_m(T) &\approx [P(1 - iH\,T/m)P]^m \\ &= P\,[(1 - iPHP\,T/m)]^m \\ &\xrightarrow{m\to\infty} Pe^{-iPHPt} \ , \end{aligned} \tag{4.13}$$

The limit dynamics is then described by the unitary evolution

$$U_Z(t)\rho_0 U_Z^\dagger(t) \equiv Pe^{-iPHPt}\,\rho_0\,e^{iPHPt}P \, , \tag{4.14}$$

where $U_Z(t)$ satisfies the relation $U_Z(t)U_Z^\dagger(t) = P$. This imply that the system never abandon the projected space $\mathcal{H}_P$. Indeed, the probability for the system to be measured in this space at the time T, after an infinite number of projective measurement on $\mathcal{H}_P$, is

$$p(T) = \mathrm{Tr}\left[U_Z(T)\rho_0 U_Z^\dagger(T)\right] = \mathrm{Tr}\left[P\rho_0\right] = 1 \, , \tag{4.15}$$

and we can safely refer to $\mathcal{H}_P$ as the "Zeno sub-space", and to $H_Z \equiv PHP$ as the "Zeno Hamiltonian".

We now proceed further beyond, picturing a situation in which we are able to ascertain the presence of the system in more than one sub-space, for example by means of a family of independent projections $\{P_n\}$ that eventually resolve the entire space, i.e.

$$P_n\mathcal{H} = \mathcal{H}_n, \quad P_nP_m = \delta_{n,m}, \quad \sum_n P_n = \mathbb{1} \, . \tag{4.16}$$

The above discussion can be straightforwardly generalized to this case. It is sufficient that, performing the measurements, at each step we project the evolved density matrix simultaneously on each $\mathcal{H}_n$, i.e. $\rho \to \sum_n P_n\rho P_n \equiv \widehat{P}[\rho]$.

We stress that, while this projections keeps unaltered the system description in each sub-space, they instantaneously destroy the coherences between different sub-spaces.

Replacing $PUP \to \widehat{P}[U]$ in Eq. 4.10, and reiterating the approximations which led us to the final result, we recover a Zeno-like evolution described by the super-operator

$$\widehat{U}_Z(t)\rho_0 = \sum_n P_n\, e^{-iH_Zt}\,\rho_0\, e^{iH_Zt}\,P_n \equiv \sum_n U_Z^{(n)}(t)\rho_0 U_Z^{(n)\dagger}(t) \, , \tag{4.17}$$

where the Zeno Hamiltonian is now given by

$$H_Z = \widehat{P}[H] = \sum_n P_n H P_n \,. \tag{4.18}$$

The operators $U_Z^{(n)}(t)$ defined above are unitary and drive a dynamics which take place independently in each subspace, i.e. $U_Z^{(n)}(t)U_Z^{(m)\dagger}(t) = \delta_{nm}P_n$. As a consequence, the initial probability $p_n(0) \equiv \mathrm{Tr}\,[\rho_0 P_n]$ to observe the system in the $n-\mathrm{th}$ sub-space at $t = 0$, is conserved along the evolution described by Eq. 4.17. Indeed, at the time t, we have

$$\begin{aligned} p_n(t) = \mathrm{Tr}[\rho(t)P_n] &= \mathrm{Tr}\left[U_Z^{(n)}(t)\rho_0 U_Z^{(n)\dagger}(t)\right] \\ &= \mathrm{Tr}\,[\rho_0 P_n] = p_n(0)\,. \end{aligned} \tag{4.19}$$

In the light of this result, we are now able to grasp the real nature of the QZD. Beside the fact that in a small evolution time the system is unable to abandon a sub-space, a key point is that each measurement destroys the coherences building up between different regions, which guide the common dynamics in the whole Hilbert space. Therefore, when the measurements are frequent enough, the internal dynamics is preserved, while the common one never happen. In the limit of infinite measurements, practically the internal population of each sub-space remains confined in it, and evolves locally, while nothing happen between the sub-spaces. The conclusion is that the QZD is not a mere consequence of a projection, but rather of the loss of the coherences between different sub-spaces. Whenever we are able to reproduce such situation, we will observe a Zeno behaviour.

QZD induced by unitary kicks

A "unitary kick" is an instantaneous unitary transformation U_{kick}, which effect is to abruptly add different global phases to different portion of the Hilbert space. The result of such repeated kicks is an overall dephasing between the sub-spaces created, which lead to a Zeno dynamics. Here we give only the final results, while a complete analysis can be found in ref. [86].

Given its unitary nature, a kick can be spectrally decomposed in a series of projections P_n , i.e.

$$U_{kick} = \sum_n e^{-i\lambda_n} P_n \,, \tag{4.20}$$

where the coefficients λ_n are the eigenvalues of each $\mathcal{H}_n = P_n\mathcal{H}$ ($\lambda_n \neq \lambda_m$ for $n \neq m$), and correspond to global phases added to each sub-space as a consequence of a kick. The action of repeated kicks performed at time intervals T/m during the evolution driven by U, is described by the product

$$U_m(T) = [U_{kick} U(T/m)]^m \ , \tag{4.21}$$

which is analogous to the operator in Eq. 4.10.

The limiting dynamics for large m is dominated by the large contribution of the U_{kiks} , and is given by

$$U_m(T) \sim \exp\left(-i \sum_n (m\lambda_n P_n + P_n H P_n t) \right) \ , \tag{4.22}$$

which has all the features of a Zeno dynamics, taking place in the subspaces identified by the spectral decomposition of the kicks. Indeed, as in the previous case of projective measurements (see Eq. 4.18), the Hamiltonian describing the evolution is projected on a series of sub-spaces, which this time are the eigenspaces of the unitary kick, i.e. the spaces containing those states such that $U_{kick} |\psi\rangle \propto |\psi\rangle$.

QZD induced by strong continuous coupling

Given that the Zeno dynamics is set by the independent, rapid control of the global phase between sub-spaces of the principal one, where the unperturbed dynamics take place, we may adopt, instead of pulsed perturbation, a continuous coupling that allows to achieve the same result when it dominates on the unperturbed Hamiltonian, i.e. a strong continuous coupling.

Let thus consider an additional coupling term H_c. The total Hamiltonian and the unitary evolution read

$$H_K = H + K H_c \, , \quad U_K(t) = e^{-i H_K T} \tag{4.23}$$

where K is a coupling constant. Of course H_c has to admit a spectral decomposition. Let P_n be the eigenspace related to the eigenvalue η_n, we can then write

$$H_c = \sum_n \eta_n P_n \, . \tag{4.24}$$

As in the limit of infinite number of projections, or kicks, here in the limit of infinite strong coupling the dynamics is dominated by H_c, and it can be demonstrated that the limiting evolution operator is

$$U_K(t) \sim \exp\left(-i \sum_n K t \eta_n P_n + P_n H P_n t \right) \ . \tag{4.25}$$

We are now familiar enough with the above structure, given that we already seen it in Eq.4.14, 4.17, and 4.22. Indeed, also here we recognize the block

Hamiltonian $\sum_n P_n H P_n$, describing the Zeno dynamics in the eigenspaces of H_c.

4.2 Experimental realization of QZD

In the light of the theoretical results discussed above, we have realized QZD in the $F = 2$ manifold of ^{87}Rb atoms by means of combinations of pulsed measurements and strong continuous couplings. In particular, we dynamically disconnected two different regions of the Hilbert space, inhibiting the transfer of a physical state between them. One of this two regions is the sub-space spanned by the levels having positive magnetic projections $m_F = +1, +2$, the other by the levels with negative projections $m_F = -1, -2$, see Fig. 4.3. The $m_F = 0$ level is "cancelled", or made unavailable for the dynamical evolution, by means of a Strong Raman coupling with the sub-level $|1, 0\rangle$, used only as auxiliary level. The atoms coherently transferred in this state by the Raman coupling can undergo a strongly decoherent process of excitation and spontaneous emission produced by a short pulse of repumping light (Dissipative light), which is resonant with the D_2 transition $F = 1 \to F' = 2$.

The unperturbed dynamics we break consists in the radio-frequency induced evolution described in section 1.4.1. We recall that, in presence of a resonant radio-frequency signal, the atomic population oscillates between the magnetic sub-levels, and the time scale of this oscillation is set by the Rabi frequency Ω in the Hamiltonian 1.14. The time scale imposed by Ω set a limit which we have to overcome to establish the QZD, as we will see in the following section.

4.2.1 Raman coupling and repumper

We coherently couple the levels $|2, 0\rangle \equiv |1\rangle$ and $|1, 0\rangle \equiv |0\rangle$ through a two photon Raman transition, as shown in Fig. 4.4.

The pump and Stokes beams are obtained from the same laser light, a Toptica DLX, approximately red-detuned $\Delta/2\pi \sim 20\,\mathrm{GHz}$ from the D_2 line. The Stokes beam is directly obtained from the DLX.To obtain the probe beam we extract part of the DLX light, and we modulate it at $\nu_{\mathrm{hfs}} \sim 6.834\,\mathrm{GHZ}$ with an EOM. This beam is then passed through an optical cavity to select the higher side-band. The power of both beams are controlled by two AOMs before they inject two fibers. The fiber outputs are combined to have mutual orthogonal polarizations, perpendicular to the external magnetic field in correspondence of the atomic sample, in order to drive σ^+, σ^- transitions. In resonance condition ($\hbar\,\nu_{\mathrm{hfs}} = E_{F=2,m_F=0} - E_{F=1,m_F=0}$), and when $\Omega_S, \Omega_P \ll \Delta$, the two $m_F = 0$ levels can be treated as an effectively two level system with coupling described by he Hamiltonian

$$H_R = \Omega_R \left(|1\rangle \langle 0| + |0\rangle \langle 1| \right) , \tag{4.26}$$

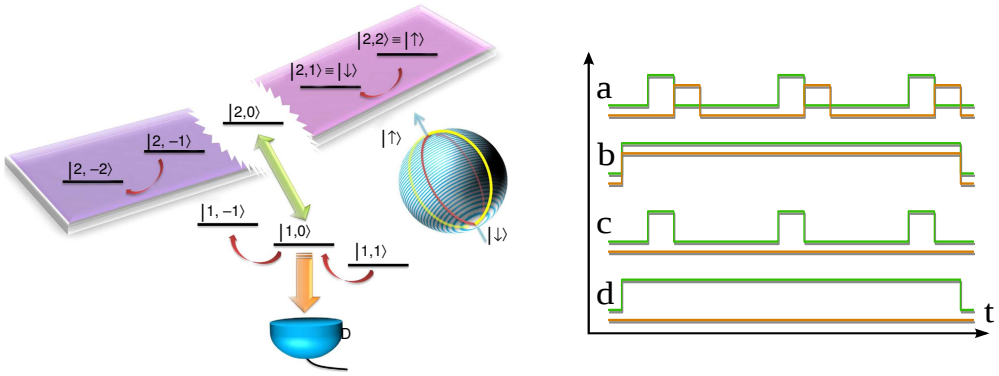

FIGURE 4.3: Left side: Representation of the effect of strong perturbation on the $|2,0\rangle$ sub-level. The $F = 2$ manifold is projected on two decoupled regions: the positive magnetic component wing, and the negative one. In particular we will study the dynamics in the protected two-level subspace $\{|2,+1\rangle\,,\,|2,+2\rangle\} \equiv \{|\downarrow\rangle\,,\,|\uparrow\rangle\}$. An applied radio-frequency field at $2.171\,\mathrm{MHz}$ couples neighbouring m_F states (thin, red arrows), a laser-induced Raman transition couples the $|2,0\rangle$ and $|1,0\rangle$ states (thick, green arrow). An additional Dissipative light (repumping light) connects the $F = 1$ states to an external level (thick, orange arrow) and induces spontaneous decay. Right side: Time sequences of the four experimental protocols achieved by combining the Raman coupling and the Dissipative light: (a) projective measurements, (b) continuous projective measurements, (c) unitary kicks and (d) continuous strong coupling.

where the effective Rabi frequency Ω_R is given by

$$\Omega_R = \frac{\Omega_P \Omega_S}{2\Delta}\,. \tag{4.27}$$

Controlling the beam powers we are able to tune the resulting Rabi frequency up to several hundreds of kHz (we performed experiments at a maximum frequency of $\Omega_R = 2\pi\,400\mathrm{kHz}$). At these frequencies the differential AC Stark shift induced between the levels of the $F = 2$ manifold is of the order of $\sim 10\,\mathrm{kHz}$, which is comparable or below the bandwidth of our manipulation pulses. We then neglect any effect arising from the light shift.

The beams are focused on the atomic sample with a waist in the focus of $D \sim 70\,\mu\mathrm{m}$, and are directed parallel to the axial radii of the BEC, to ensure an homogeneous distribution of power across the cloud (we recall that the radial dimension of the expanded BEC is $d \sim 7\,\mu\mathrm{m}$ at the moment of the manipulation). The drawback of this arrangement is the enhancement of the superradiance effect, which produces the partial break-up of the condensate into clouds of different momentum. For our investigation we managed to keep track of its effect and considering only that part of the condensate cloud that remained at rest, and the dynamics produced by the superradiance. In Fig. 4.5 we show an

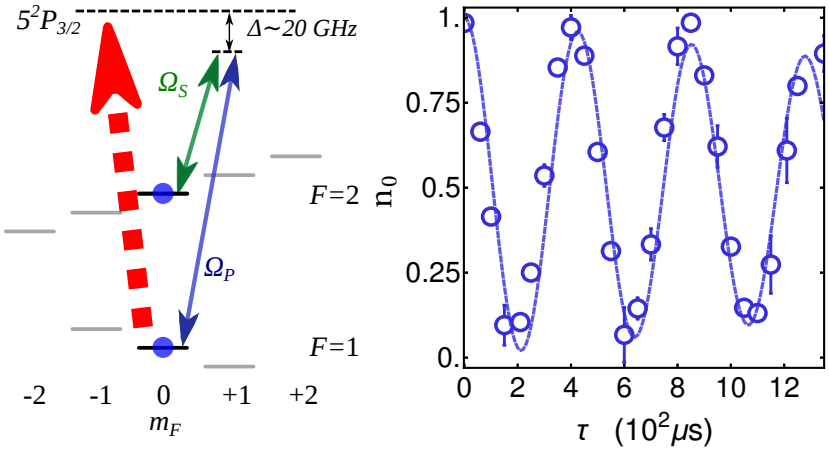

FIGURE 4.4: Detailed representation of the Raman and Dissipative Laser setup. The Stokes and pump beam are $\Delta = 20\,\mathrm{GHz}$ red detuned from the excited level $5^2\mathrm{P}_{3/2}$, and have mutual linear polarization, orthogonal to the bias magnetic field on the BEC. This polarizations configuration lead to couple the $m_F = 0$ levels by σ^+ and σ^- transitions. On the right side we is shown an example of Rabi oscillations between these levels. Each data point represents the average and standard deviation of three different realizations. With dashed line is represented a fit of a damped theoretical models on the data ($n_0 \sim \cos(\Omega_R t)\exp(-\gamma t)$), yields a Rabi frequency $\Omega_R = 2\pi\,234\,\mathrm{kHz}$ and a dephasing rate $\gamma = 20\,\mathrm{kHz}$. The Dissipative (repumping) light resonantly couples the hyperfine level $F = 1$, with the $F' = 2$ in the $5^2\mathrm{P}_{3/2}$, depleting the former in a minimum time of $0.6\,\mu\mathrm{s}$.

example of the typical superradiance induced loss of population of a condensate in the pure state $m_F = 2$ as function of the Raman beams pulse length, at beams power of $1\,\mathrm{mW}$.

The measurement system we employ for this experiment consists in a short pulse of repumping light (see section 1.2.2). By illuminating the BEC with this light the atoms in the $F = 1$ hyperfine level will be excited to the $F' = 2$, and spontaneously decaying they will emit one photon each. This is already enough to accomplish a measurement process, even if we do not effectively count the emitted photons by using a macroscopic detector.

At the maximum power available in our system ($P_D = 7\,\mathrm{mW}$) the Dissipative beam takes about $0.6\,\mu\mathrm{s}$ to completely excite all the atoms, which at this point have acquired enough recoil to be ejected from the BEC. In left side of Fig. 4.6 we show the population loss in the case of $P_D = 2\,\mathrm{mW}$, when the dissipative loss rate is $2\pi\,450\mathrm{kHz}$.

Ideally, the repumping light should not notably disturb the $F = 2$ atoms, as they are out of resonance by about $7\,\mathrm{GHz}$. However, in the experiment we observed notable losses, as shown in right side of Fig. 4.6. These are explained

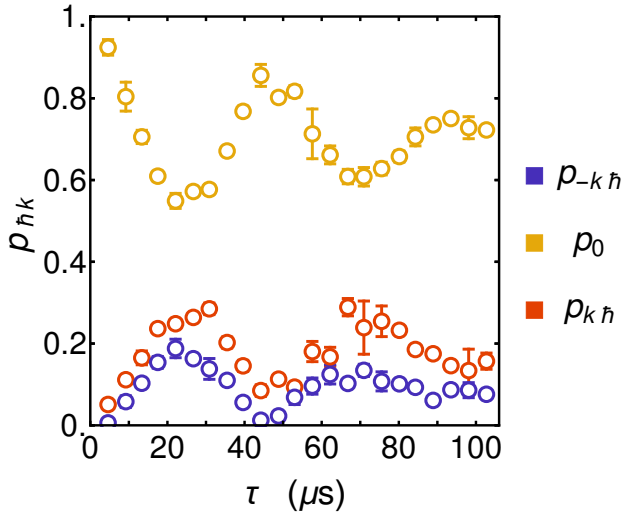

FIGURE 4.5: Effect of the collective "superradiant" scattering produced by the Raman light on the atomic cloud. With increasing Raman pulse length τ, two side clouds, having momentum $p = \pm\hbar k$ parallel to the beams direction, starts to appear. Coherent oscillations between these populations is also evident. In the experiment we usually isolate the unscattered atoms for our analysis, and by performing control measurements we separate the superradiant effect from the depletion of the Zeno protected sub-space due to a non perfect confinement.

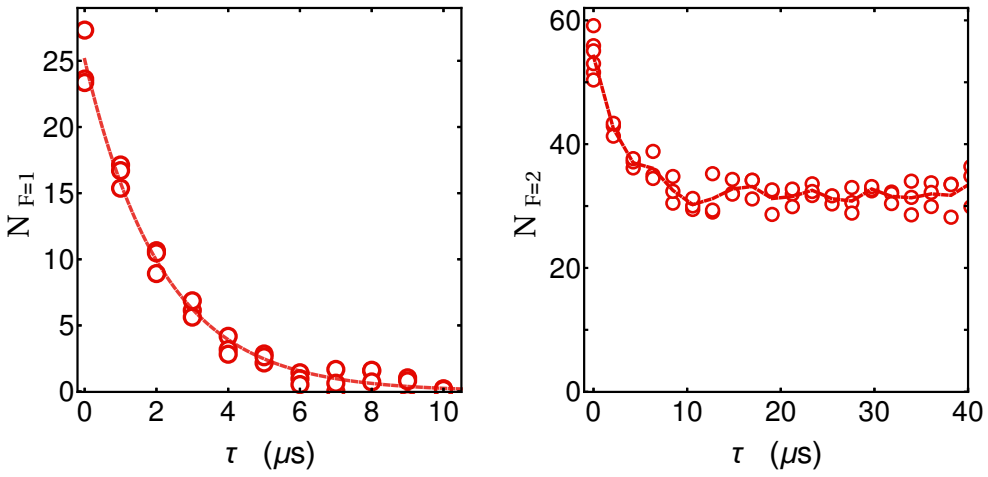

FIGURE 4.6: Left side: Decay of the $F = 1$ population produced by $2\,\mathrm{mW}$ of Dissipative light as a function of the irradiation time τ. An exponential fit (dashed smooth line) yields a loss rate of $\gamma = 2\pi\,450\,\mathrm{kHz}$. Right side: total number of atoms in the $F = 2$ manifold as a function of the irradiation time τ with the Dissipative light. The dashed line connect the mean values of the collected data. Note that the decay stops in correspondence of the complete population loss of the $F = 1$ level.

as follows: The $F = 1$ atoms absorb photons and experience heating. Via collisions this energy is transferred to the $F = 2$ atoms. Accordingly, we observe an initial decay of $F = 2$ atoms until all the $F = 1$ atoms have left the trapping region. In our analysis we have corrected the data taken for this loss of atoms, that is not related to QZD but rather due to a limitation of our experimental setup.

4.2.2 Measurement protocols

We combine the Rabi coupling and the Dissipative light in order to implement the perturbations leading to the QZD. In particular we realized four different protocols (see Fig. 4.3).

Projective measurements

In the first protocol we perform a series of discrete state-selective measurements by periodic application of the Raman and Dissipative lights.

As we mentioned above, a projection operator acting on a quantum state is an ideal description of an instantaneous measurement process, but it has no direct physical meaning. A real measurement, which can be only approximated by a projection, is more described by a sequence of steps, which finally lead the quantum system to entangle with an external apparatus, or field, characterized by some set of states having an appropriate distribution. The quantum system-apparatus interaction induces changes in this distribution, which can be classically read. At the same time, tracing out the apparatus states we are left with an incoherent superposition representing the state of the system after the measurement. A similar description is well represented, for example, by atoms undergoing an absorption process: an atomic cloud absorbs photons from a light field then spontaneously reemitting them.

In our case we perform a state selective measurement in two steps: we coherently transfer the atoms from the level $|2,0\rangle$ to the $|1,0\rangle$ by means of a Raman π-pulse $0.8\,\mu$s long, and this is immediately followed by a pulse of Dissipative light $0.6\,\mu$s long, absorbed by the atoms in the $F = 1$ level. The final result is thus a good approximation of a projective (destructive) measurements on the single level $|2,0\rangle$, and an incomplete (non-destructive) projection on the remaining space, which is left unperturbed by the sequence. In other words, a state $|\psi\rangle$ undergoing this measurement process is left in the state

$$|\psi\rangle \to P^{\perp}_{|2,0\rangle}\,|\psi\rangle\ , \tag{4.28}$$

where $P^{\perp}_{|2,0\rangle}$ is the projection on the space orthogonal to $|2,0\rangle$, represented, on the $F=2$ manifold, by the matrix

$$P^{\perp}_{|2,0\rangle} = \begin{pmatrix} 1 & 0 & 0 & 0 & 0 \\ 0 & 1 & 0 & 0 & 0 \\ 0 & 0 & 0 & 0 & 0 \\ 0 & 0 & 0 & 1 & 0 \\ 0 & 0 & 0 & 0 & 1 \end{pmatrix}. \tag{4.29}$$

The Hamiltonian guiding the unperturbed dynamics of our atoms is given by Eq. 1.14, thus the Zeno Hamiltonian $H_Z = P^{\perp}_{|2,0\rangle} H_{F=2} P^{\perp}_{|2,0\rangle}$ reads

$$H_Z = \hbar \begin{pmatrix} \delta_{2,+2}(\mathrm{B},\omega_{RF}) & \Omega & 0 & 0 & 0 \\ \Omega & \delta_{2,+1}(\mathrm{B},\omega_{RF}) & 0 & 0 & 0 \\ 0 & 0 & 0 & 0 & 0 \\ 0 & 0 & 0 & \delta_{2,-1}(\mathrm{B},\omega_{RF}) & \Omega \\ 0 & 0 & 0 & \Omega & \delta_{2,-2}(\mathrm{B},\omega_{RF}) \end{pmatrix}. \tag{4.30}$$

We finally spend some words on the limit of infinitely frequent measurements. For our scheme we used a repetition rate of $\delta\tau = 2.2\,\mu$s, while the Rabi frequency was set to $\Omega = 2\pi\,15\,$kHz. We are thus in the (finite) limit $\delta\tau \ll 2\pi/\Omega$. As we will show in the results section, indeed the Zeno dynamics is visible. However the evolution described by Eq. 4.14 is unitary only when $m \to \infty$, otherwise the projections introduce an irreversibility in the dynamics. We thus expect to observe a decay in the Zeno dynamics which scales as $\gamma \sim \delta\tau\Omega$.

Continuous projective measurements

The second protocol implemented consists in a continuous, projective measurement, achieved by applying both the Raman beams and the Dissipative Light continuously. The intensities are chosen such as to obtain a Raman-induced coupling of $\Omega_R = 2\pi\,250\,$kHz and a dissipative loss rate of $2\pi\,450\,$kHz, i.e. slightly above the Raman coupling rate. This was done to avoid blocking the Raman transition by a Dissipative Light-induced QZE, while still implementing an effective measurement scheme. Likewise the sequential projections scheme, also in this case the dynamics is described by the projected Hamiltonian in Eq. 4.30.

The continuous coupling should represent the closer approximation to the limit $m \to \infty$, however we still have to consider the time-scale coming from the Raman coupling.

Unitary kicks

In the third experiment we apply a sequence of unitary kicks. A unitary kick consists in a Raman π-pulses having a duration of $0.7\,\mu$s, and coupling, as

usual, the sub-states $|2,0\rangle$ and $|1,0\rangle$. The dynamical evolution, guided at $\Omega = 2\pi\,15\,\mathrm{kHz}$, is perturbed by a kick every $2.2\,\mu\mathrm{s}$.

As shown in section 4.1.2, the Zeno dynamics take place in the sub-spaces $\mathcal{H}_n = P_n\mathcal{H}$ which spectrally decompose the kicks, and arises from the large oscillating phases between them, resulting in an effective decoherence. In our case these eigenspaces are 1-dimensional, and correspond to the two superpositions $\mathcal{H}_\pm = |2,0\rangle \pm |1,0\rangle$ (note that both share the state $|2,0\rangle$). Given that the relative phases of this two superposition changes so abruptly as to decouple them, the same happens respect to the phase of the unperturbed orthogonal space $\mathcal{H}_\pm^\perp$, identified by the projection $P_{|2,0\rangle}^\perp$ defined above. Consequently, the evolution in $\mathcal{H}_\pm^\perp$ is independent by these in the two $\mathcal{H}_\pm$, and the Zeno Hamiltonian describing the internal dynamics is again given by Eq. 4.30.

Strong continuous coupling

In the fourth protocol, we kept the Raman beams on continuously, achieving the strong continuous coupling regime. The Raman beams are tuned to a coupling strength of $\Omega_R = 2\pi\,136\,\mathrm{kHz}$, to be compared with the radio-frequency Rabi coupling $\Omega = 2\pi\,15\,\mathrm{kHz}$. Also in this case we cannot fulfil the theoretical limit $\Omega_R \to \infty$, even if the finite limit $\Omega_R \gg \Omega$ allows to observe the QZD.

As in the case of unitary kicks, the continuous coupling causes the large oscillation of the phases of the 1-dimensional subspaces $\mathcal{H}_\pm = |2,0\rangle \pm |1,0\rangle$ respect to the remaining Hilbert space. Therefore the same conclusions holds, i.e. we will observe a decoupled dynamics in space $\mathcal{H}_\pm^\perp$, described by the usual Hamiltonian in Eq. 4.30.

4.3 Results

We tested our four protocols during the BEC dynamical evolution observing in each case the QZD.

The tests was performed as follows. We start, after the evaporation of the atomic cloud in the chip magnetic trap, with a BEC containing $\sim 90\times10^3$ atoms in the pure state $|2,+2\rangle$. We switch off all the trapping fields letting the BEC fall free, and, simultaneously, a homogeneous magnetic field of $3.1\,\mathrm{Gauss}$, corresponding to an energy splitting of the Zeeman states of about $2.2\,\mathrm{MHz}$, is set along the y direction. We perform the experiments after $0.7\,\mathrm{ms}$ of free expansion, when the cloud is dilute enough to observe a single particle dynamics, and the bias fields are stable to the predetermined values. Each experiment consists in applying to the chip antenna, for a time τ, a radio-frequency signal driving resonant oscillations at the Rabi frequency $\Omega = 15\,\mathrm{kHz}$, and, simultaneously, in performing the sequence of light pulses corresponding to one of our protocols. After the manipulation we record the number of atoms in each of the m_F states

of both the hyperfine levels, by means of the Stern–Gerlach method and absorption imaging sequence (see section 1.4.2). For each τ we perform 3 experimental cycles under the same parameters condition, extracting mean values and standard deviations of the relative populations.

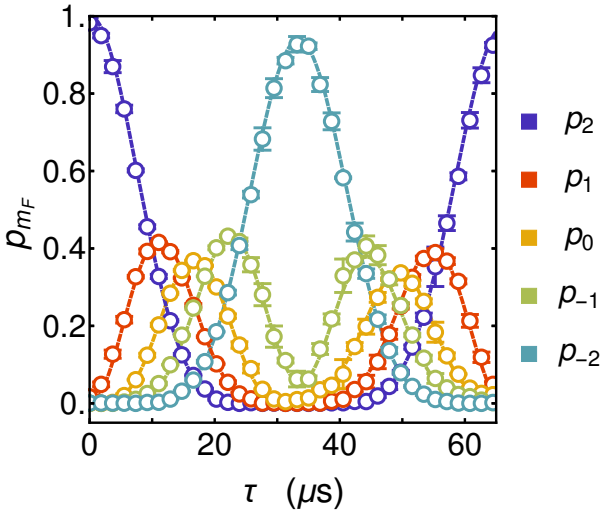

FIGURE 4.7: Resonant Rabi oscillations in the $F = 2$ manifold, induced by a radio-frequency signal, as a function of signal length τ. The mean values and standard deviations of the experimentally measured populations are shown as dots and error bars, while the dashed line represent a theoretical evolution at a Rabi frequency of $\Omega = 2\pi\, 15\,\mathrm{kHz}$. Note that each level is populated during the evolution.

By alternating measurement of the populations evolution undergoing the Zeno dynamics, with control measurements in which the radio-frequency driving is switched off, we are able to distinguish the fraction of atoms lost from the protected two-level sub-space as a consequence of imperfections of the Zeno confinement, from the loss caused by residual scattering of the Raman and Dissipative Light beams, and by the superradiant scattering, as well. Analysing the collected data we can then correct them to take into account these additional losses.

Finally, a comparison of the results obtained with the four different protocols is given in the panels of Fig. 4.8. As expected, given that we start with the total population in the $|2,+2\rangle$ state, the evolution is almost perfectly confined between this level and the $|2,+1\rangle$. This confirms that the dynamics is guided by a projected Zeno Hamiltonian describing an effective two-level system (see. Eq. 4.30). Therefore, hereafter we will refer to these two protected states as $|2,+2\rangle \equiv |\uparrow\rangle$, and $|2,+1\rangle \equiv |\downarrow\rangle$.

For the chosen parameters, we observe a similar population dynamics for each of the four protocols. This is in close agreement with the prediction that

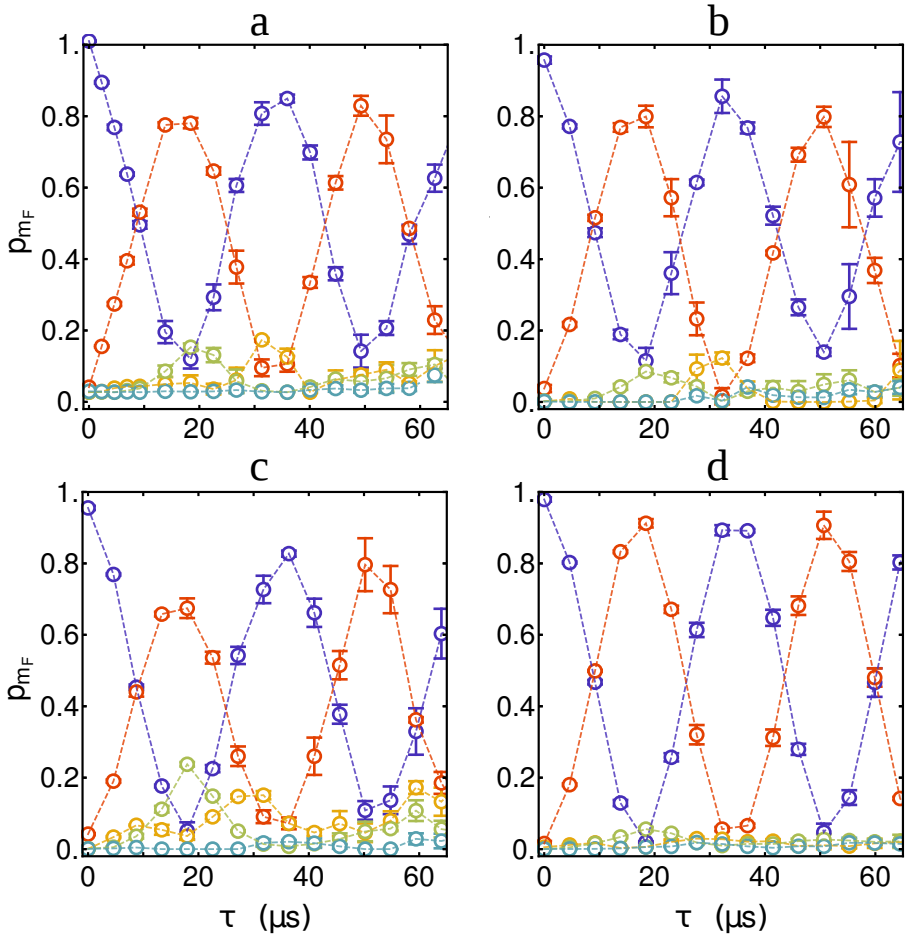

FIGURE 4.8: Population evolution in presence of the constant radio-frequency driving pulse plus the perturbations produced by our four measurement protocols, as a function of the driving pulse length τ. The colour scheme is the same as in Fig. 4.7. The labels stand for: a) Pulsed projective measurements. b) Continuous projective measurements. c) Unitary kicks. d) Continuous strong coupling. Note how the populations oscillate between the $|\downarrow\rangle$ (red) and $|\uparrow\rangle$ (blue) states.

frequent projective measurements, strong continuous coupling or fast unitary kicks should all asymptotically lead to the same projected Hamiltonian. Note that even with the finite measurement rates and coupling strengths used here the degree of confinement can be strong, leading to only a small fraction leaking in the neighbour projected sub-space via the forbidden $m_F = 0$ level.

The equivalence of the protocols is even more evident by superimposing the results on each other, as done in Fig. 4.8. No substantial difference between the populations behaviour can be appreciated, within the noise coming from the experimental parameter fluctuations.

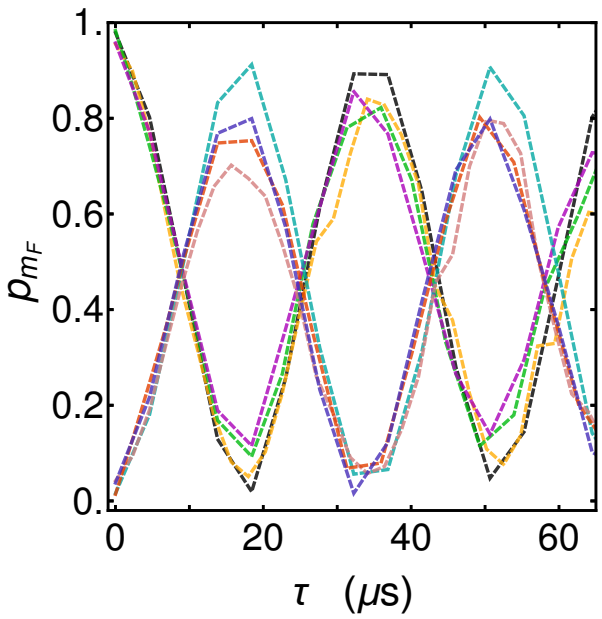

FIGURE 4.9: Superposition of the average data of the only $|\downarrow\rangle$ and $|\uparrow\rangle$ levels, reported in the previous figure. Each colour correspond to a different protocol. Note the substantially equivalent behaviour.

4.3.1 Subspace protection

We now turn to quantify the coherence in the dynamically created two-dimensional space, and strength of the Zeno confinement, by adopting an effective two-state model to describe the measured oscillations obtained with our four protocols.

We describe the dynamics in terms of the density matrix ρ, by the equations

$$\begin{aligned}
\dot{\rho}_{\alpha\alpha} &= i\Omega(\rho_{\alpha\beta} - \rho^*_{\alpha\beta}) \\
\dot{\rho}_{\beta\beta} &= -i\Omega(\rho_{\alpha\beta} - \rho^*_{\alpha\beta}) - 2\,\Gamma_{\text{loss}}\,\rho_{\beta\beta} \\
\dot{\rho}_{\alpha\beta} &= i\Omega(\rho_{\alpha\alpha} - \rho^*_{\beta\beta}) - (\Gamma_{\text{loss}} + 2\,\gamma_{\text{deph}})\rho_{\alpha\beta}\,,
\end{aligned} \tag{4.31}$$

in which, besides the coupling Ω, we introduce the phenomenological loss rate Γ_{loss} to account for losses from the state $|\downarrow\rangle$ through the Zeno barrier, and the dephasing rate γ_{deph} describing a decoherence process between $|\uparrow\rangle$ and $|\downarrow\rangle$. These two terms have different physical origin. The rate Γ_{loss} arises from the imperfect protection of the Zeno subspace due to our finite coupling strength and measurements rate. The dephasing rate γ_{deph} is originated by the residual density dependent energy shifts, by off-resonant scattering of photons from the Raman beams, and, to a lesser extent, by collisions with background gas.

This model is valid only for short evolution times. Indeed, as the population can escape from $|\downarrow\rangle$ through the Zeno barrier, it can come back as well in

the protected space. This process is unavoidable, given the finite size of our Hilbert space and the limited coupling strength. However, we should observe the revival of population into the Zeno (partially) protected subspace for longer times, above $200\,\mu$s. Therefore, we apply our two-level model only for times up to $100\,\mu$s, where the population revival is still not affecting the observed dynamics.

Given that we demonstrated the equivalence between the four protocols, we focus now to the analysis of only the strong continuous coupling confinement. In particular we measure the population evolution in correspondence of Raman couplings Ω_R chosen in the range from $100\,\mathrm{kHz}$ to $225\,\mathrm{kHz}$, then, by leaving Γ_{loss} and γ_{deph} as free parameter, we fit the theoretical dynamics given by Eq. 4.31, to the experimental data. The results of the fit are shown in Fig. 4.10.

The dephasing rate γ_{deph} reported in the upper panel does not shown any particular trend. On the contrary, the lower panel shows how in the range of power spanned, the lifetime $2\pi\,\Gamma_{\mathrm{loss}}^{-1}$ increases 100-fold with Ω_R, at an exponential rate of about $0.05\,\mathrm{kHz}^{-1}$. We stress that a complete suppression of a leakage of atoms out of the two-level subspace is only expected at infinite Ω_R, where the projected Hamiltonian of Eq. 4.30 would be exactly realized.

4.3.2 Coherence check

To extract further information about the evolution of the coherences during the Zeno dynamics, we perform Ramsey interferometry within the two-level subspace $\{|\uparrow\rangle, |\downarrow\rangle\}$, confined by the constant strong coupling. The splitting and recombining radio-frequency pulses have a $\pi/2$ area, i.e., in the case of perfect Zeno confinement, starting from the state $|\uparrow\rangle$ the first pulse would produces the state superposition $|\psi\rangle = (|\uparrow\rangle - i\,|\downarrow\rangle)/\sqrt{2}$. The interferometric fringes are measured by varying the delay T_B between the two pulses, and in Fig. 4.11 we report the population distribution achieved after the second as a function of τ.

The clear oscillations are unambiguous indicators of the evolution of a coherence in the projected sub-space. Rather than being damped by dephasing, the long term evolution of the fringes appears relatively unstable, mostly because of the experimental parameters fluctuation from one realization to the next. Nonetheless, it is possible to observe fringe contrast close to unity even for long delays.

We finally compare the experimental data describing the fringes with the theoretical evolution obtained by simulating the Ramsey schemes with Eq. 4.31, in which the set the parameters Γ_{loss} and γ_{deph} to the values extracted by the fit shown in Fig. 4.10 in correspondence of the Ω_R used, i.e. $\Omega = 2\pi\,140\,\mathrm{kHz}$. In particular, we used $\Gamma_{\mathrm{loss}} \in 2\pi\,\{0.03, 0.33\}\,\mathrm{kHz}$, and $\gamma_{\mathrm{deph}} \in 2\pi\,\{0.09, 0.69\}\,\mathrm{kHz}$. As it can be noted the agreement is highly satisfactory, and supports even more our simple two level description.

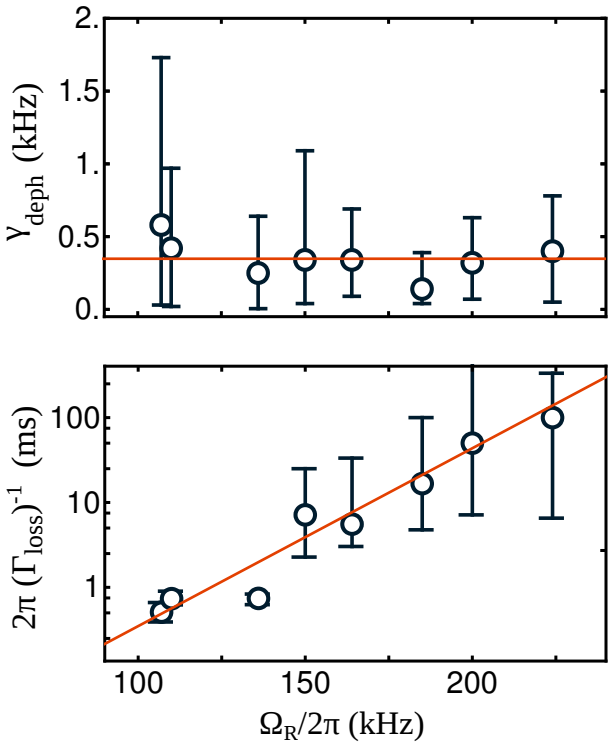

FIGURE 4.10: Dephasing rates (upper panel) and lifetimes (lower panel) of the atomic population in the subspace $\{|\downarrow\rangle, |\uparrow\rangle\}$, decoupled by the continuous strong coupling protocol, as a function of the Raman frequency Ω_R. The radio-frequency Rabi coupling is constant at $\Omega = 2\pi\,15\,\mathrm{kHz}$. The data (points) are well fitted (red lines) by a constant dephasing rate and by an exponentially increasing lifetime, respectively. The error bars indicate the uncertainty in the parameter estimation, and are determined by correcting the fraction of atoms survived in the protected subspace with the maximum and minimum estimation of the unwanted depletion due to the superradiant scattering, and to the non resonant Dissipative light effect (see section 4.2.1). The dephasing rates display only a weak dependence on the Raman coupling strength. The lifetimes are observed to increase hundredfold.

4.4 Conclusions and outlook

We have experimentally demonstrated the equivalence of different perturbation protocols in creating a coherent Zeno dynamics in disjoint Hilbert sub-spaces. In particular we have shown how to tailor a two-level region, and in which limit of the resources employed the dynamics is localized, and the leaking of probability to neighbouring Hilbert subspaces is suppressed.

Finally, the schemes implemented realizes a dynamical superselection rule, which imposes that if two initial states are separated in different regions of the Hilbert space, the separation will persist at all times.

The reader familiar with the basics principle of quantum processing, will

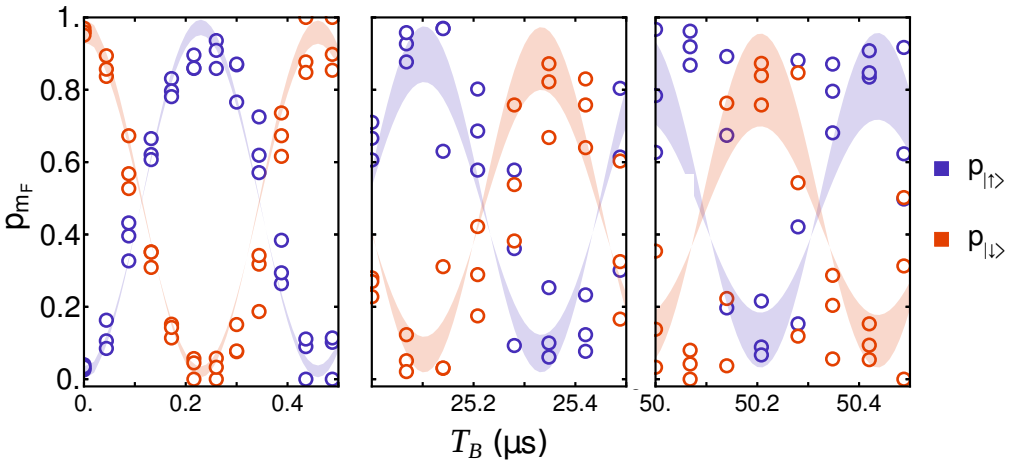

FIGURE 4.11: Ramsey fringes measured between the $|\downarrow\rangle$ and $|\uparrow\rangle$ populations as a function of the free evolution time between the splitting and recombining pulse T_B (see section 1.4.3 for detail about Ramsey scheme). The data cover three time windows $0.5\,\mu$s long. Together with the experimental data we also show the two-level model prediction (shaded areas), described by the equations 4.31, using the parameter deduced from the fit shown in Fig. 4.10. The Raman beams induces a coupling strength of $\Omega = 2\pi\,140\,\mathrm{kHz}$. The long term fluctuations of the experimental parameter such as magnetic field and Raman coupling strength, produces large populations fluctuation at longer evolution time, but full fringe contrast is still observed.

recognize in our protocols a possible tool to dynamically store the information encoded in a qubit in a controllable "register". Indeed QZD can be dynamically exploited to preserve quantum coherence against any leakage to the environment.

Conclusions and outlook

In this thesis I show how it is possible to coherently manipulate a ^{87}Rb BEC realizing two tasks which usually require many resources, i.e. the reconstruction of an unknown internal state and the preparation of an arbitrary superposition for further manipulations. These tasks, beyond their wide applicability in several quantum technology applications, are necessary ingredients for any quantum information processing algorithm.

I also report the results of the first experimental realization of Quantum Zeno Dynamics (QZD), which opens the way to a number of possible applications in the context of quantum information. Indeed QZD provides both the possibility to tailor the Hilbert space of interest in region storing some quantum information, and a possible noise-protection scheme which can be used to preserve quantum coherence against any leakage to the environment. A possible improvement of the reported results would be the implementation of all fields necessary to establishment of QZD in a single integrated device, allowing more compact applications.

In the future, all these results may be used in combination, to provide a quantum information unit which can be easily written and read out. In particular, QZD and optimal control could offer the possibility to realize a controllable quantum gate, where the qubits live in the Zeno sub-spaces created by the strong coupling between the $m_F = 0$ states, and a suitably engineered optimal pulse achieves the gate operation [87]. Thanks both to the possibility to design manipulation pulses robust against fluctuations and inhomogeneous dephasing, and to the strength of QZD, even with finite resources, it should be possible to achieve fault-tolerant quantum computation.

Finally, analysing the interplay between different control protocols and back-action of measurements could lead to major achievements in the understanding of quantum control and its limitations, providing new solutions for quantum technologies.

Appendix A

RWA Hamiltonian

In this appendix I will recover the Hamiltonians in Eq. 1.15 and 1.14, which describes the ground hyperfine levels of ^{87}Rb in presence of a uniform magnetic bias field and a radio-frequency coupling having a time modulated frequency, and the resulting dynamical equation, Eq. 1.16.

The Hamiltonian in Eq. 1.11 includes the hyperfine interaction and the coupling between an external magnetic field $\boldsymbol{B_0}$ and a time varying field $\boldsymbol{B}(t) = B(t)\widehat{\boldsymbol{\xi}}$ with the total magnetic momentum of the Rb atoms $\boldsymbol{\mu} = \boldsymbol{\mu_S} + \boldsymbol{\mu_I} = \mu_B(g_S\mathbf{S} + g_I\mathbf{I})$, where $\mathbf{S}$ is the electronic spin, and $\mathbf{I}$ the nuclear spin (the angular magnetic moment is $\mathbf{L} = 0$ in the ground state). We assume a monochromatic, frequency modulated, field $B(t) = B_{RF}\cos(\omega_{RF}(t)\,t)$. For weak fields, the Hamiltonian represented on the basis of the F^2 and F_z eigenstates $|F, m_F\rangle$ (see section 1.1.1), reads

$$\begin{aligned} H = &\sum_{F,m_F} E_{F,m_F}(B_0)\,|F,m_F\rangle\,\langle F,m_F| + \\ &\frac{\hbar}{2}\sum_{F,m_F,m_{F'}} \Omega_{F,m_F,m_{F'}}\,|F,m_F\rangle\,\langle F,m_{F'}|\cos(\omega_{\mathrm{RF}}(\mathrm{t})\,\mathrm{t})\,, \end{aligned} \tag{A.1}$$

where the couplings $\Omega_{F,m_F,m_{F'}}$ are given by Eq. 1.13. When $\widehat{\boldsymbol{\xi}}$ is linearly polarized and orthogonal to $\mathbf{B_0}$, the dot product $\widehat{\boldsymbol{\xi}}\cdot\mathbf{S}$ can be expressed in terms of raising and lowering spin operators S^+ and S^-. In this case the non vanishing $\Omega_{F,m_F,m_{F'}}$ are those such that $m_F = m_{F'} \pm 1$, and can be expressed as $c_{F,m_F,m'_F}\,\Omega$, where Ω is the Rabi frequency of the driving. The coefficients c_{F,m_F,m'_F} are easily calculated by expanding the $|F, m_F\rangle$ states in the basis of electron and nuclear magnetic spin $|S, S_z, I, I_z\rangle$.

When the energy splitting $\Delta E \sim \mu_B g_F B_0$ between the m_F sub-levels is such that $|\Delta E - \omega_{RF}(t)| \ll \omega_{RF}(t)$, we neglect the out of resonance components of the $\cos(\omega_{RF}(t)\,t)$ in Eq. A.1. The second term in the LHS of this equation is then

given by

$$H_{RF} \equiv \frac{\hbar\Omega}{2} \sum_{m_F, m_{F'} > m_F} c_{2,m_F,m_{F'}} \left(|2, m_F\rangle \langle 2, m_{F'}| \, e^{-i\,\omega_{RF} t} + \text{h.c.} \right) + \frac{\hbar\Omega}{2} \sum_{m_F, m_{F'} > m_F} c_{1,m_F,m_{F'}} \left(|1, m_F\rangle \langle 1, m_{F'}| \, e^{i\,\omega_{RF} t} + \text{h.c.} \right) . \tag{A.2}$$

The sign difference in the exponential above is due to the different slope of the energy level dependence by the magnetic field in the two hyperfine manifolds.

The time dependence in Eq. A.2 is removed by means of a unitary transformation in the reference frame rotating with the laser radiation, defined by

$$U(t) = \sum_{m_F} e^{i\,m_F\,\omega_{RF}(t)\,t} \, |2, m_F\rangle \langle 2, m_F| + \sum_{m_F} e^{-i\,m_F\,\omega_{RF}(t)\,t} \, |1, m_F\rangle \langle 1, m_F| \ , \tag{A.3}$$

which, substituted in the Liouville's equation, yields to

$$U^\dagger(t) H_{RF} U(t) = \frac{\hbar\Omega}{2} \sum_{\substack{F, m_F \\ m_{F'} > m_F}} c_{F,m_F,m_{F'}} \left(|F, m_F\rangle \langle F, m_{F'}| + \text{h.c.} \right) , \tag{A.4}$$

and to the additional diagonal terms

$$\partial_t \left(U^\dagger(t) \right) U(t) = i\,\partial_t \left(\omega_{RF}(t) t \right) \left(\sum_{m_F} m_F \ |2, m_F\rangle \langle 2, m_F| - \sum_{m_F} m_F \ |1, m_F\rangle \langle 1, m_F| \right) . \tag{A.5}$$

Thus, the usual diagonal elements $\delta_{F,m_F}(B, \omega_{RF})/\hbar E_{F,m_F}(B) - E_{F,0}(B) - \hbar\, m_F\, \omega_{RF}$ introduced in section 1.4.1, in the case of a frequency modulated field has to be modified by the substitution

$$\omega_{RF} \to \partial_t (\omega_{RF}(t)\, t) \, . \tag{A.6}$$

Appendix B

^{87}Rb relevant numbers

Fundamental Physical Constants

Planck's constant	$\hbar$	$6.58211899(16) \times 10^{-16}\mathrm{eV\,s}$
Bohr magneton	μ_B	$\hbar\, 1.399624604(35)\mathrm{MHz/G}$

^{87}Rb data

Mass	m	$1.443160648(72) \times 10^{-25}\mathrm{kg}$
Nuclear spin	I	$3/2$

^{87}Rb D_2 line data

Wavelength (vacuum)	λ	$780.241209686(13)\mathrm{nm}$
Frequency	ω_0	$2\pi\, 3842304844685(62)\mathrm{THz}$
Natural line width	Γ	$2\pi\, 6.0666(18)\mathrm{MHz}$
Lifetime	τ	$26.2348(77)\mathrm{ns}$
Recoil Velocity	v_r	$5.8845\,\mathrm{mm/s}$
Saturation Intensity $\lvert F=2,\pm2\rangle \rightarrow \lvert F'=3,\pm3\rangle$	I_{sat}	$1.669(2)\mathrm{mW/cm^2}$
Hyperfine structure constant	A_{hfs}	$\hbar\, 3.417341305452145(45)\mathrm{GHz}$
Electron spin g-factor	g_s	$2.0023193043622(15)$
Nuclear spin g-factor	g_I	$?0.0009951414(10)$

Bibliography

[1] C. Brif, R. Chakrabarti, and H. Rabitz, "Control of quantum phenomena: Past, present and future", *New Journal of Physics*, vol. **12**, no. 7, p. 075 008, 2010.

[2] R. E. Bailey, A. M. Smith, and S. Nie, "Quantum dots in biology and medicine", *Physica E: Low-dimensional Systems and Nanostructures*, vol. **25**, no. 1, pp. 1–12, 2004.

[3] H. Kawano, Y. Nabekawa, A. Suda, Y. Oishi, H. Mizuno, A. Miyawaki, and K. Midorikawa, "Attenuation of photobleaching in two-photon excitation fluorescence from green fluorescent protein with shaped excitation pulses", *Biochemical and Biophysical Research Communications*, vol. **311**, no. 3, pp. 592–596, 2003.

[4] H. Lee, Y.-C. Cheng, and G. R. Fleming, "Coherence dynamics in photosynthesis: Protein protection of excitonic coherence", *Science*, vol. **316**, no. 5830, pp. 1462–1465, 2007.

[5] I. Buluta and F. Nori, "Quantum simulators", *Science*, vol. **326**, no. 5949, pp. 108–111, 2009.

[6] R. P. Feynman, "Simulating physics with computers", *International Journal of Theoretical Physics*, vol. **21**, no. 6, pp. 467–488, 1982.

[7] D. P. DiVincenzo *et al.*, "The physical implementation of quantum computation", *ArXiv preprint quant-ph/0002077*, 2000.

[8] J. Reichel and V. Vuletic, *Atom chips*. John Wiley & Sons, 2011.

[9] S. Jose, P. Surendran, Y. Wang, I. Herrera, L. Krzemien, S. Whitlock, R. McLean, A. Sidorov, and P. Hannaford, "Periodic array of bose-einstein condensates in a magnetic lattice", *Phys. Rev. A*, vol. **89**, no. 5, p. 051 602, 2014.

[10] M. Trupke, F. Ramirez-Martinez, E. A. Curtis, J. P. Ashmore, S. Eriksson, E. A. Hinds, Z. Moktadir, C. Gollasch, M. Kraft, G. V. Prakash, *et al.*, "Pyramidal micromirrors for microsystems and atom chips", *Applied Physics Letters*, vol. **88**, no. 7, p. 071 116, 2006.

[11] D. A. Allwood, T. Schrefl, G. Hrkac, I. G. Hughes, and C. S. Adams, "Mobile atom traps using magnetic nanowires", *Applied Physics Letters*, vol. **89**, no. 1, p. 014 102, 2006.

[12] P. Bohi, M. F. Riedel, J. Hoffrogge, J. Reichel, T. W. Hansch, and P. Treutlein, "Coherent manipulation of bose-einstein condensates with state-dependent microwave potentials on an atom chip", *Nat. Phys.*, vol. **5**, no. 8, pp. 592–597, 2009.

[13] A. S. Sørensen, C. H. van der Wal, L. I. Childress, and M. D. Lukin, "Capacitive coupling of atomic systems to mesoscopic conductors", *Phys. Rev. Lett.*, vol. **92**, no. 6, p. 063 601, 2004.

[14] M. Gierling, P. Schneeweiss, G. Visanescu, P. Federsel, M. Häffner, D. P. Kern, T. E. Judd, A. Günther, and J. Fortágh, "Cold-atom scanning probe microscopy", *Nat. Nano.*, vol. **6**, no. 7, pp. 446–451, 2011.

[15] G. Kurizki, P. Bertet, Y. Kubo, K. Mølmer, D. Petrosyan, P. Rabl, and J. Schmiedmayer, "Quantum technologies with hybrid systems", *Proceedings of the National Academy of Sciences*, vol. **112**, no. 13, pp. 3866–3873, 2015.

[16] P. Treutlein, T. W. Hänsch, J. Reichel, A. Negretti, M. A. Cirone, and T. Calarco, "Microwave potentials and optimal control for robust quantum gates on an atom chip", *Phys. Rev. A*, vol. **74**, no. 2, p. 022 312, 2006.

[17] Y. Colombe, T. Steinmetz, G. Dubois, F. Linke, D. Hunger, and J. Reichel, "Strong atom–field coupling for bose–einstein condensates in an optical cavity on a chip", *Nature*, vol. **450**, no. 7167, pp. 272–276, 2007.

[18] M. F. Riedel, P. Böhi, Y. Li, T. W. Hänsch, A. Sinatra, and P. Treutlein, "Atom-chip-based generation of entanglement for quantum metrology", *Nature*, vol. **464**, no. 7292, pp. 1170–1173, 2010.

[19] C. Cohen-Tannoudji and D. Guéry-Odelin, "Advances in atomic physics", *World Scientific, Singapore*, vol. **32**, p. 36, 2011.

[20] I. Herrera, "Degenerate quantum gases production and coherent manipulation on atom chips", PhD thesis, Ph. D. thesis, Departamento de Física de Materiales, Universidad Autónoma de Madrid, 2012.

[21] D. A. Steck, "Rubidium 87 D line data", version 2.1.5, 2015. [Online]. Available: `http://steck.us/alkalidata/`.

[22] E. Majorana, "Atomi orientati in campo magnetico variabile", *Il Nuovo Cimento (1924-1942)*, vol. **9**, no. 2, pp. 43–50, 1932.

[23] D. E. Pritchard, "Cooling neutral atoms in a magnetic trap for precision spectroscopy", *Phys. Rev. Lett.*, vol. **51**, pp. 1336–1339, 15 1983.

[24] M. O. Mewes, M. R. Andrews, N. J. van Druten, D. M. Kurn, D. S. Durfee, and W. Ketterle, "Bose-einstein condensation in a tightly confining dc magnetic trap", *Phys. Rev. Lett.*, vol. **77**, pp. 416–419, 3 1996.

[25] J. Söding, D. Guéry-Odelin, P. Desbiolles, G. Ferrari, and J. Dalibard, "Giant spin relaxation of an ultracold cesium gas", *Phys. Rev. Lett.*, vol. **80**, pp. 1869–1872, 9 1998.

[26] T. Esslinger, I. Bloch, and T. W. Hänsch, "Bose-einstein condensation in a quadrupole-ioffe-configuration trap", *Phys. Rev. A*, vol. **58**, R2664–R2667, 4 1998.

[27] J. Petrovic, I. Herrera, P. Lombardi, F. Schäfer, and F. S. Cataliotti, "A multi-state interferometer on an atom chip", *New Journal of Physics*, vol. **15**, no. 4, p. 043 002, 2013.

[28] C. Lovecchio, S. Cherukattil, B. Cilenti, I. Herrera, F. S. Cataliotti, S. Montangero, T. Calarco, and F. Caruso, "Quantum state reconstruction on atom-chips", *New Journal of Physics*, vol. **17**, no. 9, p. 093 024, 2015.

[29] M. A. Nielsen and I. L. Chuang, *Quantum computation and quantum information*. Cambridge university press, 2010.

[30] A. I. Lvovsky and M. G. Raymer, "Continuous-variable optical quantum-state tomography", *Rev. Mod. Phys.*, vol. **81**, pp. 299–332, 1 2009.

[31] C. Gross, H. Strobel, E. Nicklas, T. Zibold, N. Bar-Gill, G. Kurizki, and M. Oberthaler, "Atomic homodyne detection of continuous-variable entangled twin-atom states", *Nature*, vol. **480**, no. 7376, pp. 219–223, 2011.

[32] G. M. D'Ariano, L. Maccone, and M. Paini, "Spin tomography", *Journal of Optics B: Quantum and Semiclassical Optics*, vol. **5**, no. 1, p. 77, 2003.

[33] Z. Hradil, "Quantum-state estimation", *Phys. Rev. A*, vol. **55**, no. 3, R1561, 1997.

[34] M. Steffen, M. Ansmann, R. C. Bialczak, N. Katz, E. Lucero, R. McDermott, M. Neeley, E. M. Weig, A. N. Cleland, and J. M. Martinis, "Measurement of the entanglement of two superconducting qubits via state tomography", *Science*, vol. **313**, no. 5792, pp. 1423–1425, 2006.

[35] A. Silberfarb, P. S. Jessen, and I. H. Deutsch, "Quantum state reconstruction via continuous measurement", *Phys. Rev. Lett.*, vol. **95**, p. 030 402, 3 2005.

[36] U. Fano, "Description of states in quantum mechanics by density matrix and operator techniques", *Rev. Mod. Phys.*, vol. **29**, pp. 74–93, 1 1957.

[37] G. Klose, G. Smith, and P. S. Jessen, "Measuring the quantum state of a large angular momentum", *Phys. Rev. Lett.*, vol. **86**, pp. 4721–4724, 21 2001.

[38] A. Smith, C. Riofrío, B. Anderson, H. Sosa-Martinez, I. Deutsch, and P. S. Jessen, "Quantum state tomography by continuous measurement and compressed sensing", *Phys. Rev. A*, vol. **87**, no. 3, p. 030 102, 2013.

[39] C. M. Caves, C. A. Fuchs, and R. Schack, "Quantum probabilities as bayesian probabilities", *Phys. Rev. A*, vol. **65**, no. 2, p. 022 305, 2002.

[40] F. Huszár and N. M. T. Houlsby, "Adaptive bayesian quantum tomography", *Phys. Rev. A*, vol. **85**, no. 5, p. 052 120, 2012.

[41] G. M. D'Ariano, M. F. Sacchi, and J. Kahn, "Minimax quantum-state discrimination", *Phys. Rev. A*, vol. **72**, no. 3, p. 032 310, 2005.

[42] G. M. d'Ariano, P. Perinotti, and M. Sacchi, "Informationally complete measurements and group representation", *Journal of Optics B: Quantum and Semiclassical Optics*, vol. **6**, no. 6, S487, 2004.

[43] F. Caruso, V. Giovannetti, C. Lupo, and S. Mancini, "Quantum channels and memory effects", *Rev. Mod. Phys.*, vol. **86**, pp. 1203–1259, 4 2014.

[44] T. Rowan, "The subplex method for unconstrained optimization", PhD thesis, Ph. D. thesis, Department of Computer Sciences, Univ. of Texas, 1990.

[45] A. Uhlmann, "The metric of bures and the geometric phase", in *Groups and related Topics*, Springer, 1992, pp. 267–274.

[46] J. Petrovic, I. Herrera, P. Lombardi, F. Schaefer, and F. S. Cataliotti, "A multi-state interferometer on an atom chip", *New Journal of Physics*, vol. **15**, no. 4, p. 043 002, 2013.

[47] C. Lovecchio, F. Schäfer, S. Cherukattil, M. Alì Khan, I. Herrera, F. S. Cataliotti, T. Calarco, S. Montangero, and F. Caruso, "Optimal preparation of quantum states on an atom-chip device", *Phys. Rev. A*, vol. **93**, p. 010 304, 1 2016.

[48] H. Müntinga, H. Ahlers, M. Krutzik, *et al.*, "Interferometry with bose-einstein condensates in microgravity", *Phys. Rev. Lett.*, vol. **110**, p. 093 602, 9 2013.

[49] S. Kuhr, W. Alt, D. Schrader, I. Dotsenko, Y. Miroshnychenko, A. Rauschenbeutel, and D. Meschede, "Analysis of dephasing mechanisms in a standing-wave dipole trap", *Phys. Rev. A*, vol. **72**, p. 023 406, 2 2005.

[50] L. Viola and S. Lloyd, "Dynamical suppression of decoherence in two-state quantum systems", *Phys. Rev. A*, vol. **58**, pp. 2733–2744, 4 1998.

[51] B. Yan, S. A. Moses, B. Gadway, J. P. Covey, K. R. A. Hazzard, A. M. Rey, D. S. Jin, and J. Ye, "Observation of dipolar spin-exchange interactions with lattice-confined polar molecules", *Nature*, vol. **501**, pp. 521–525, 7468 2013.

[52] A. Widera, S. Trotzky, P. Cheinet, S. Fölling, F. Gerbier, I. Bloch, V. Gritsev, M. D. Lukin, and E. Demler, "Quantum spin dynamics of mode-squeezed luttinger liquids in two-component atomic gases", *Phys. Rev. Lett.*, vol. **100**, p. 140 401, 14 2008.

[53] M. H. Schleier-Smith, I. D. Leroux, and V. Vuleti ć, "States of an ensemble of two-level atoms with reduced quantum uncertainty", *Phys. Rev. Lett.*, vol. **104**, p. 073 604, 7 2010.

[54] I. Walmsley and H. Rabitz, "Quantum physics under control", *Physics Today*, vol. **56**, no. 8, pp. 43–49, 2003.

[55] H. Mabuchi and N. Khaneja, "Principles and applications of control in quantum systems", *International Journal of Robust and Nonlinear Control*, vol. **15**, no. 15, pp. 647–667, 2005, ISSN: 1099-1239.

[56] H. Rabitz, "Focus on quantum control", *New Journal of Physics*, vol. **11**, no. 10, p. 105 030, 2009.

[57] I. Bloch, J. Dalibard, and W. Zwerger, "Many-body physics with ultracold gases", *Rev. Mod. Phys.*, vol. **80**, pp. 885–964, 3 2008.

[58] T. Caneva, M. Murphy, T. Calarco, R. Fazio, S. Montangero, V. Giovannetti, and G. E. Santoro, "Optimal control at the quantum speed limit", *Phys. Rev. Lett.*, vol. **103**, p. 240 501, 24 2009.

[59] T. Caneva, T. Calarco, R. Fazio, G. E. Santoro, and S. Montangero, "Speeding up critical system dynamics through optimized evolution", *Phys. Rev. A*, vol. **84**, p. 012 312, 1 2011.

[60] V. Giovannetti, S. Lloyd, and L. Maccone, "Quantum limits to dynamical evolution", *Phys. Rev. A*, vol. **67**, p. 052 109, 5 2003.

[61] M. G. Bason, M. Viteau, N. Malossi, P. Huillery, E. Arimondo, D. Ciampini, R. Fazio, V. Giovannetti, R. Mannella, and O. Morsch, "High-fidelity quantum driving", *Nat. Phys.*, vol. **8**, no. 2, pp. 147–152, 2012.

[62] S. Chu, "Cold atoms and quantum control", *Nature*, vol. **416**, pp. 206–210, 6877 2002.

[63] M. Shapiro and P. Brumer, "Coherent control of molecular dynamics", *Reports on Progress in Physics*, vol. **66**, no. 6, p. 859, 2003.

[64] T. Caneva, T. Calarco, and S. Montangero, "Chopped random-basis quantum optimization", *Phys. Rev. A*, vol. **84**, p. 022 326, 2 2011.

[65] P. Doria, T. Calarco, and S. Montangero, "Optimal control technique for many-body quantum dynamics", *Phys. Rev. Lett.*, vol. **106**, p. 190 501, 19 2011.

[66] S. Rosi, A. Bernard, N. Fabbri, L. Fallani, C. Fort, M. Inguscio, T. Calarco, and S. Montangero, "Fast closed-loop optimal control of ultracold atoms in an optical lattice", *Phys. Rev. A*, vol. **88**, p. 021 601, 2 2013.

[67] J. Scheuer, X. Kong, R. S. Said, *et al.*, "Precise qubit control beyond the rotating wave approximation", *New Journal of Physics*, vol. **16**, no. 9, p. 093 022, 2014.

[68] F. Caruso, S. Montangero, T. Calarco, S. F. Huelga, and M. B. Plenio, "Coherent optimal control of photosynthetic molecules", *Phys. Rev. A*, vol. **85**, p. 042 331, 4 2012.

[69] S. Hoyer, F. Caruso, S. Montangero, M. Sarovar, T. Calarco, M. B. Plenio, and K. B. Whaley, "Realistic and verifiable coherent control of excitonic states in a light-harvesting complex", *New Journal of Physics*, vol. **16**, no. 4, p. 045 007, 2014.

[70] M. Shapiro and P. Brumer, *Principles of the quantum control of molecular processes*. 2003, p. 250.

[71] F. Schäfer, I. Herrera, S. Cherukattil, C. Lovecchio, F. S. Cataliotti, F. Caruso, and A. Smerzi, "Experimental realization of quantum zeno dynamics", *Nat. Comm.*, vol. **5**, 2014.

[72] J. V. Neumann, *Mathematical foundations of quantum mechanics*, 2. Princeton university press, 1955.

[73] B. Misra and E. C. G. Sudarshan, "The zeno's paradox in quantum theory", *Journal of Mathematical Physics*, vol. **18**, no. 4, 1977.

[74] W. M. Itano, D. J. Heinzen, J. J. Bollinger, and D. J. Wineland, "Quantum zeno effect", *Phys. Rev. A*, vol. **41**, pp. 2295–2300, 5 1990.

[75] E. W. Streed, J. Mun, M. Boyd, G. K. Campbell, P. Medley, W. Ketterle, and D. E. Pritchard, "Continuous and pulsed quantum zeno effect", *Phys. Rev. Lett.*, vol. **97**, no. 26, p. 260 402, 2006.

[76] A. G. Kofman and G Kurizki, "Acceleration of quantum decay processes by frequent observations", *Nature*, vol. **405**, no. 6786, pp. 546–550, 2000.

[77] A. G. Kofman and G. Kurizki, "Universal dynamical control of quantum mechanical decay: Modulation of the coupling to the continuum", *Phys. Rev. Lett.*, vol. **87**, p. 270 405, 27 2001.

[78] M. Fischer, B Gutiérrez-Medina, and M. Raizen, "Observation of the quantum zeno and anti-zeno effects in an unstable system", *Phys. Rev. Lett.*, vol. **87**, no. 4, p. 040 402, 2001.

[79] N. Erez, G. Gordon, M. Nest, and G. Kurizki, "Thermodynamic control by frequent quantum measurements", *Nature*, vol. **452**, no. 7188, pp. 724–727, 2008.

[80] G. A. Paz-Silva, A. Rezakhani, J. M. Dominy, and D. Lidar, "Zeno effect for quantum computation and control", *Phys. Rev. Lett.*, vol. **108**, no. 8, p. 080 501, 2012.

[81] S. Maniscalco, F. Francica, R. L. Zaffino, N. L. Gullo, and F. Plastina, "Protecting entanglement via the quantum zeno effect", *Phys. Rev. Lett.*, vol. **100**, no. 9, p. 090 503, 2008.

[82] S. Gherardini, S. Gupta, F. S. Cataliotti, A. Smerzi, F. Caruso, and S. Ruffo, "Stochastic quantum zeno by large deviation theory", *New Journal of Physics*, vol. **18**, no. 1, p. 013 048, 2016.

[83] S. Gherardini, C. Lovecchio, M. M. Müller, P. Lombardi, F. Caruso, and F. S. Cataliotti, "Ergodicity in randomly perturbed quantum systems", *ArXiv preprint arXiv:1604.08518*, 2016.

[84] P Facchi and S Pascazio, "Quantum zeno subspaces", *Phys. Rev. Lett.*, vol. **89**, no. 8, p. 080 401, 2002.

[85] P. Facchi and S. Pascazio, "Quantum zeno dynamics: Mathematical and physical aspects", *Journal of Physics A: Mathematical and Theoretical*, vol. **41**, no. 49, p. 493 001, 2008.

[86] P. Facchi, D. A. Lidar, and S. Pascazio, "Unification of dynamical decoupling and the quantum zeno effect", *Phys. Rev. A*, vol. **69**, p. 032 314, 3 2004.

[87] M. Müller, D. Reich, M Murphy, H Yuan, J Vala, K. Whaley, T Calarco, and C. Koch, "Optimizing entangling quantum gates for physical systems", *Phys. Rev. A*, vol. **84**, no. 4, p. 042 315, 2011.